Aeroacoustics of Perforated Drag Plates for Quiet Transport Aircraft

by

Kiril Dimitrov Sakaliyski

B.S., Aeronautical Engineering
Technical University-Sofia, 2002

Submitted to the Department of Aeronautics and Astronautics
in partial fulfillment of the requirements for the degree of

Master of Science in Aeronautics and Astronautics

at the

MASSACHUSETTS INSTITUTE OF TECHNOLOGY

September 2005

Author .....
Department of Aeronautics and Astronautics
August 19, 2005

Certified by .....
Zoltan Spakovszky
Associate Professor of Aeronautics and Astronautics
Thesis Supervisor

Accepted by .....
Jaime Peraire
Professor of Aeronautics and Astronautics
Chairman, Department Committee on Graduate Students

Aeroacoustics of Perforated Drag Plates for Quiet Transport Aircraft

by

Kiril Dimitrov Sakaliyski

Submitted to the Department of Aeronautics and Astronautics
on August 19, 2005, in partial fulfillment of the
requirements for the degree of
Master of Science in Aeronautics and Astronautics

Abstract

Historically aircraft noise is one of the principal environmental issues for aviation. Within this context, the Silent Aircraft Initiative was launched with the objective to achieve a step-change in noise reduction compared to current practice. One of the most critical tasks in noise reduction is to develop technologies to increase drag in quiet ways. The work presented in this thesis focuses primarily on aeroacoustic tests and analysis of perforated drag plates. The idea behind a quiet spoiler or drag rudder is to alter the noise production mechanism by perforating the drag plates. The hypothesis is that the large length scales responsible for the noise radiated by unsteady vortical structures can be changed to small length scales driving jet noise at frequencies which are perceived unannoying by the human ear.

The aeroacoustic characteristics of laboratory-scale perforated spoilers were measured in an acoustic chamber at MIT. Based on the experimental data a noise prediction model was developed for the bluff-body and turbulent mixing noise generated by a perforated drag rudder. Acoustic phased array measurements of seven perforated plates in four different installation configurations were conducted in the Markham wind tunnel at Cambridge University to further investigate the noise mechanisms. The analysis of the test results showed that there are two identifiable peak frequencies which scale with free stream velocity. Different candidate length scales were investigated with the goal to collapse the data on a Strouhal number basis. However, a universal length scale was not found. It was hypothesized that the noise is mainly due to the isotropic turbulence generated behind such perforated plate. Due to the high background noise levels in the experiments the impact of the perforations on the low frequency noise signature could not be assessed.

A perforated plate of 28.19% porosity with a hole diameter to plate length ratio d/L of 0.013 and a non-dimensional hole separation s/L of 0.0217 was identified to be the most beneficial plate in terms of noise reduction. The experiments showed that a spoiler mounted on the suction surface of the wing is the quietest configuration. In order to scale the results to full size, the observed peak magnitudes are suggested to scale with the 4^{th} power of the free stream velocity. In addition, the overall sound pressure levels were found to scale with plate size such that an increase in source area causes an equivalent increase in the acoustic power.

The developed models were used to predict the noise signature of a full sized drag rudder which enabled a 6° glide slope angle resulting in a 4 dBA reduction in cumulative sound pressure level of the candidate SAX10 Silent Aircraft design.

Thesis Supervisor: Zoltan Spakovszky
Title: Associate Professor of Aeronautics and Astronautics

Acknowledgments

The completion of this thesis is the result of assistance and advice from a number of individuals.

First and most importantly, I want to thank my advisor, Prof. Zoltan Spakovszky, for giving me the opportunity to work on this very interesting project and his support, insight and guidance over the past two years.

Second, I need to thank Dr. James Hileman for answering numerous questions concerning aeroacoustics, providing me with invariable ideas and for always taking time to review and make sense of the test results.

I also wish to thank the following individuals that have made my Gas Turbine Laboratory experience much more memorable: Juan Castiella, Adam Diedrich, Justin Jaworski, Anya Jones, Nayden Kambouchev, Vai-Man Lei, Jean-Francois Onnee, Angelique Plas, Parthiv Shah, Yuto Shinagawa, Dr. Borislav Sirakov, Ryan Tam, David Tan and Serge Tournier. Thanks to Prof. Edward Greitzer for keeping me busy during the terms I took his classes, which on the other hand gave me the depth I need to interpret computational results and hence effectively extract conclusions about key features of complex flows.

I would also like to express my thanks to my best friends Mariya Petrova and Olivier Toupet whom I had numerous memorable experiences with while studying for the Ph.D. qualifiers and goofing around on a daily basis.

Special thanks to the people from the Silent Aircraft Initiative and especially the airframe team members Christodoulos Andreou, Andrew Faszer and Ho-Chul Shin for their valuable help and ideas.

The author wishes to gratefully acknowledge the help of Victor Dubrowski, James Letendre and Richard Perdichizzi at MIT and John Clark at Cambridge University for their help with the experiments' setup and without whom this work would have not been possible. Thanks are due also to Jordan Brayanov and Atanas Pavlov for their help and valuable technical advice throughout the course of this project.

My parents and my younger brother also deserve acknowledgements as the one

who always encouraged me to pursue my dreams. I could not have gone so far, if there were not their full support.

Last, but not least important, I want to thank my true love Krassi for supporting me through those long days when we are long apart and spent so little time together.

This project was part of the Silent Aircraft Initiative and was funded by the Cambridge-MIT Institute. This support is gratefully acknowledged.

Nomenclature

Roman

d	perforation diameter
x	horizontal separation between two neighboring perforations or axis direction
y	vertical separation between two neighboring perforations or axis direction
s	separation between two neighboring perforations in a uniform perforation pattern
U	free stream velocity
a	speed of sound
F	force
j	$\sqrt{-1}$
f	frequency
f_s	vortex shedding frequency or sample rate
Δf	frequency resolution
T	length of a time signal
H	height of a plate
L	length of a plate
r	distance to an observer or radius
p	pressure
C_D	drag coefficient
C	contraction coefficient
u	mean velocity through a perforated plate
D	drag force
A	plate area

x_s	spoiler location on the wing, measured from the wing leading edge
c_{ws}	wing chord at spoiler location
St	Strouhal number
Re	Reynolds number
M	Mach number
N	number of perforations or number of sample points
I	acoustic intensity
P	acoustic power
AIF	area increase factor
n	exponential speed dependance of the plate noise levels

Greek

β	porosity, defined as the ratio of open to total plate area
ρ	air density
μ	air viscosity
θ	directivity angle in degrees
κ	plate resistance to a passage of air
ψ	deployment angle of a drag device
ρ	density
δ	boundary layer thickness
ω	angular frequency

Subscripts

PP	perforated plate or pistonphone quantity
SP	solid plate quantity
$corr$	corrected quantity
P	peak quantity
$norm$	normalized quantity
req	required quantity
$prod$	produced quantity
av	average quantity

Abbreviations

SAI	Silent Aircraft Initiative
SAX	Silent Aircraft eXperimental design
MIT	Massachusetts Institute of Technology
CU	University of Cambridge
FFT	Fast Fourier Transform
SPL	Sound Pressure Level
OASPL	Overall Sound Pressure Level
DAQ	Data Acquisition System

Contents

List of Figures

List of Tables

Chapter 1

Introduction

Historically, noise is one of the principal environmental issues for aviation. Aircraft noise is particularly annoying to people living in areas around airports despite considerable reductions in noise and a corresponding decrease in the population around airports. Air traffic keeps increasing as does pressure from the public to control the increase in aircraft noise. Moreover, concern about noise remains a constraint on efforts to expand airport capacity to meet the growing demand for air travel.

One region in which aircraft noise has been extensively studied and controlled is the United Kingdom. Estimates from the United Kingdom Department for Transportation put noise costs for London Heathrow airport in the range of £293 million (approximately $571 million) in lost property value alone [1].

One way to solve this problem is to introduce quieter aircraft. Research at MIT and Cambridge University was initiated to design a Silent Aircraft[1]. The transition to quieter aircraft is expected to benefit communities, airports, and airlines. The levels of noise affecting communities near airports are expected to decline, providing a better quality of life for those communities. That decline is, in turn, expected to reduce community opposition to airport operations and expansion and to reduce the demand for funds provided for noise abatement through federal grants and user charges. The airlines expect the transition to facilitate their long-term planning for

[1]Silent means sufficiently quiet that outside the airport perimeter aircraft noise is less than the background noise in a well populated area.

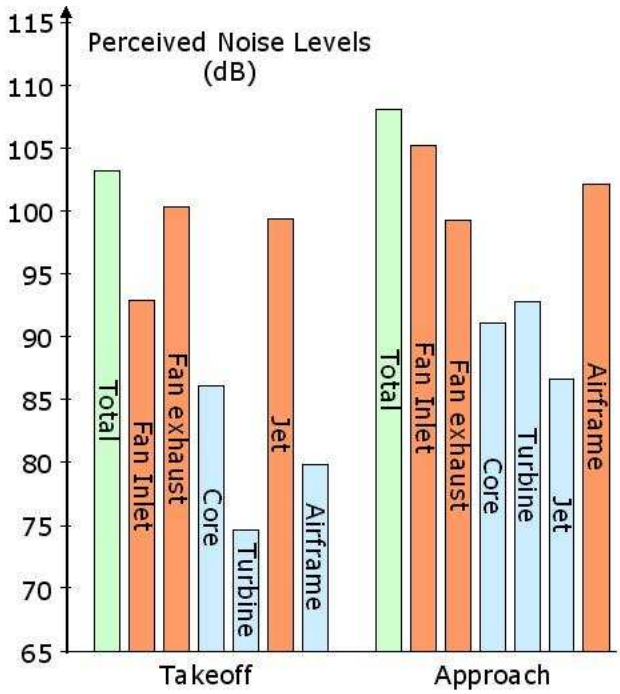

Figure 1-1: Aircraft noise sources on approach and takeoff [3].

investment and fleet operations. These expectations vary concerning the extent to which the airlines would replace rather than convert old aircraft to comply with the new noise requirements [2].

1.1 Background

1.1.1 Aircraft Noise Sources

The noise generated by a transport aircraft can be divided in two main groups: one due to airframe and other due to engine noise sources. The absolute and relative levels of each of the noise sources depend on the aircraft configuration. The various noise sources on a conventional transport aircraft are shown in Figure 1-1 for the takeoff and approach configurations.

Engine noise sources include fan and compressor noise, turbine noise, combustion (core) noise and jet noise (see Figure 1-2). In the past, turbojet engines were the dominant noise source both on approach and takeoff. Since the introduction of high-

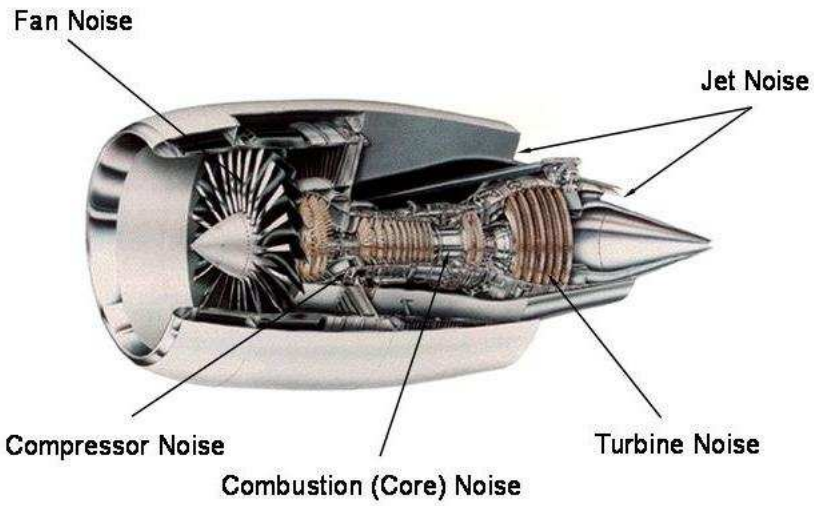

Figure 1-2: Aircraft engine noise sources

bypass turbofan engines and acoustic liners, the engine noise was significantly reduced (by of over 10 EPNdB [4]). Currently, acoustic liners are used in the inlet, fan case, aft bypass duct, and core nozzle to attenuate both fan and core engine noise. These passive liners are tuned to be most effective at frequencies in the peak annoyance range (2-4 kHz).

The airframe is an important noise source from a large aircraft in its landing configuration as the level of noise may only be a few decibels below the level of noise radiated from the engines. The airframe noise is due to unsteady flow from wing and tail trailing edges, turbulent flow through and around deflected wing trailing edge flaps and leading edge slats, flow past landing gear shafts, and other undercarriage elements, fuselage and wing turbulent boundary layers, panel vibrations, and high-speed airflow past contours and cavities such as uncovered wheel wells (see Figure 1-3).

Much research is aimed at reducing airframe noise contribution by improving the 'smoothness' of the flow over the most critical components. The longer-term solution of this problem is a Silent Aircraft that can operate within this air transportation system.

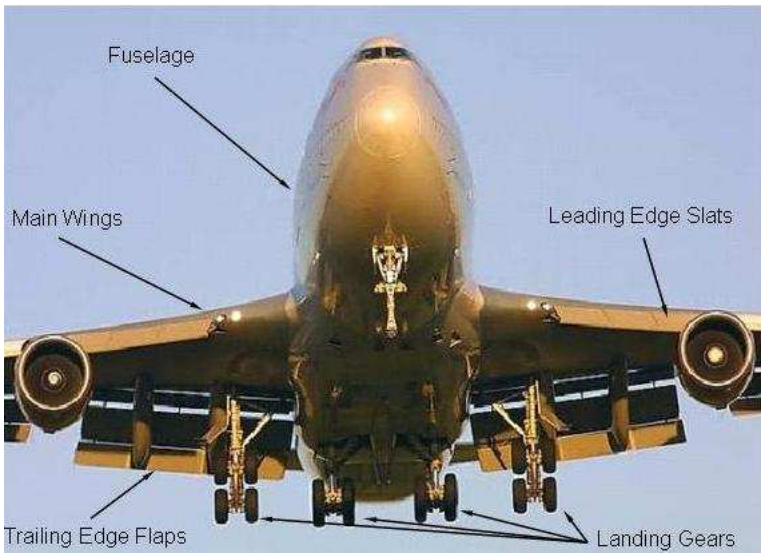

Figure 1-3: Sources of airframe noise (picture courtesy of Ben Pritchard, Airliners.net).

1.1.2 Silent Aircraft Initiative

Within this context, the Silent Aircraft Initiative (SAI) funded by the Cambridge-MIT Institute (CMI) was launched. The objective of the SAI is to achieve a step-change in noise levels compared to current practice and this will require a radically different approach to the problem. This is a multidisciplinary problem involving airframe, engine, and operation design teams. Assessment of the economic impact of a Silent Aircraft is also under investigation. The design process of such an aircraft requires close interaction between the design teams. The information flow is shown in Figure 1-4.

This information flow establishes the framework for a fully integrated and optimized for noise Silent Aircraft. The boxes represent the different research areas. In each of these areas, the aim is to use both analytical techniques and experimental measurements to assess potential solutions and to validate advanced prediction tools, which will then be used to scale the results to a full size aircraft.

In order to reduce airframe and propulsion system noise levels below the background noise in well-populated areas, noise must be a prime design variable. It is also clear that conceptually new aircraft configurations should be studied. A blended-

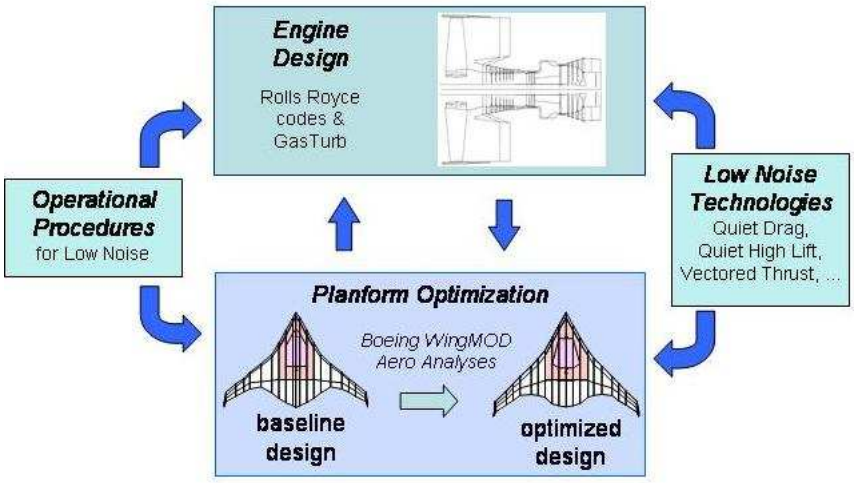

Figure 1-4: Information flow in the Silent Aircraft Initiative [5].

wing-body type aircraft configuration with aerodynamically-smooth lifting surfaces is a potential candidate to achieve the airframe noise reduction goals. The current Silent Aircraft eXperimental design, SAX10, is shown in Figure 1-5.

However, mitigating airframe noise emissions by removing the high-lift devices (leading edge slats and trailing edge flaps) invariably leads to a reduction in the drag. Also, when using a steeper approach profile, during which the noise sources are further from the ground and the noise levels are lower because of the atmospheric and geometric attenuation, a lot of drag need to be generated. Thus, one of the most critical tasks in noise reduction is to develop technologies to increase drag in quiet ways.

One way to dissipate the energy on approach is to use deployable low-noise high-drag structures. Conventional spoilers as those shown in Figure 1-6 create drag in a noisy manner. The processes that lead to drag on such bluff bodies involve unsteady wakes and inevitably generate noise.

So far, relatively little analysis has been done to investigate the possibility of generating drag quietly during approach. Noise reduction should be considered along with the performance (drag generation) penalty. Therefore, silent drag concepts should be investigated to determine how much drag could be produced with satisfactory noise

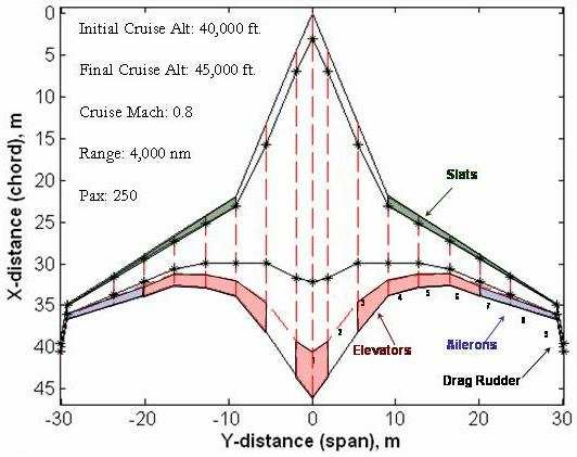

(a) Top section view [5].

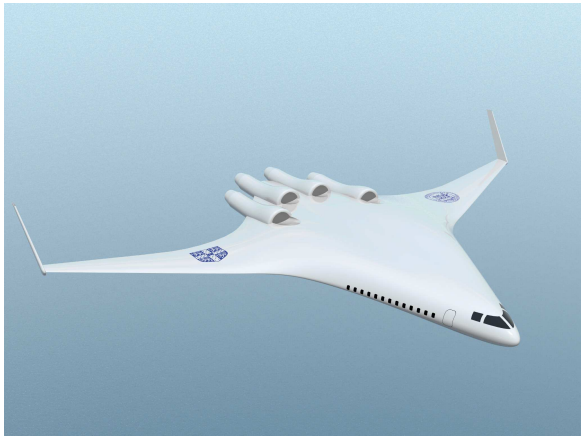

(b) Design rendering (picture courtesy of Steve Thomas).

Figure 1-5: Current Silent Aircraft eXperimental design SAX10.

Figure 1-6: Aircraft spoilers (picture courtesy of Michael Catchpole, Airliners.net).

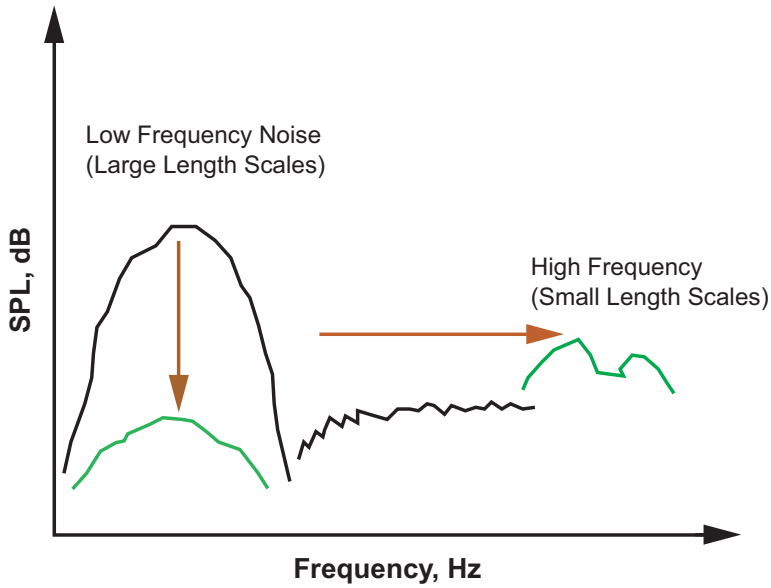

Figure 1-7: Hypothetical transformation in noise signature through perforated drag plates.

reduction.

1.2 The Idea Behind Silent Spoiler/Drag Rudder

The idea behind a silent spoiler/drag rudder is to alter the noise production mechanism by perforating the spoilers/drag rudders. It is hypothesized that, by introducing perforations the large length scales responsible for the noise radiated by unsteady vortical structures are changed to small length scales driving jet noise, which at high frequencies are attenuated more effectively and perceived less annoying to the human ear. This transformation of the noise signature is depicted in Figure 1-7.

Jet and jet noise studies [6, 7] also suggest that the peak frequency associated with mini-jets is shifted to higher frequencies and that the mini-jets interfere to produce a lower sound pressure level. Atmospheric attenuation, on the other hand, increases nearly exponentially with increasing frequency, and spectral noise components contribute less to the Effective Perceived Noise Level (EPNL)[2] noise metric

[2]This is a metric used to describe the tone-sensing characteristic of the human hearing system and also contains a "duration" correction, which recognizes the rising and falling nature of aircraft

as the frequency increases above 4 kHz. Humans have a low sensitivity to acoustic frequencies above 10 kHz and noise at frequencies higher than 10 kHz is not included in the calculation of EPNL. This idea may be applied to the noise produced by a perforated plate resembling an array of low speed mini-jets. The perforated spoilers/drag rudders could help reduce noise produced by current and future generations of aircraft.

One of the main challenges of designing quieter drag devices is that current analytical models do not accurately predict the noise that would be emitted by such designs. Also, the effect that such designs may have on the lift and drag of the wing has not been investigated. Therefore, it is necessary for an actual model to be built and tested to determine the potential noise reduction that can be achieved by using such silent drag devices.

The work presented in this thesis focuses primarily on aeroacoustic tests and analysis of perforated drag plates.

1.2.1 Research Objectives

The primary objective of these aeroacoustic experiments is to asses the acoustic benefits and impact on drag of a perforated spoiler/drag rudder. The second objective is to assess the strength and if possible, determine the directivity of the noise sources (bluff-body and turbulence mixing noise) of such perforated plates. The third objective is to assess different configurations of perforated drag devices. The fourth objective is to find scaling laws for the perforated plate noise spectra. These scaling laws are envisioned to help establish a prediction model for the acoustic signature of perforated drag devices to be used on a Silent Aircraft.

1.2.2 Research Questions

The main research question is to determine for a fixed level of drag what noise reduction potential can be achieved by perforating the drag plates.

noise, and the fact that duration varies with both the type of aircraft and the mode of operation [8].

1.2.3 Success Goals

The primary success goal is to demonstrate a net benefit in the acoustic signature of perforated drag plates compared to a solid plate on the same drag basis.

The second success goal is to show that low frequency noise is reduced and that the turbulence mixing noise generated at mid frequencies is shifted to higher frequencies.

1.2.4 Technical Approach

To meet the research objectives, first the noise mechanisms associated with perforated drag plates are identified together with the non-dimensional parameters governing these noise mechanisms. Second, a drag analysis is conducted to investigate the effect that perforations have on the drag generation of such perforated plates.

Conducting aeroacoustic tests using advanced equipment such as an acoustic phased array is expensive and requires careful planning. Thus, fast and most importantly inexpensive aeroacoustic tests are needed to get preliminary results of the noise characteristics of perforated drag plates.

A preliminary test campaign is conducted in the acoustic chamber facility at the Massachusetts Institute of Technology (MIT). First, the chamber is acoustically characterized. Then, aeroacoustic tests of perforated plates are conducted. The data is analyzed and the results are used for development of a preliminary noise prediction tool.

Based on the preliminary acoustic test campaign at MIT, the parameter space of perforated drag plates is defined and later explored in the Markham wind tunnel at Cambridge University (CU). The Markham wind tunnel is equipped with an acoustic phased array which provides a powerful measurement capability that can identify noise 15 dB below the wind tunnel background noise [9].

1.3 Thesis Outline

Chapter 2 presents the noise mechanisms and dimensional analysis of the key geometric and fluid dynamic parameters that govern the noise generation of a perforated drag plate. A drag analysis to investigate the effects of the perforations on the drag generation is then discussed.

In Chapter 3, a characterization of the acoustic chamber at MIT is presented together with the test equipment calibration procedure and data reduction technique.

Chapter 4 presents a combined experimental and analytical effort that was conducted to determine the noise signature of perforated drag plates.

In Chapter 5, the parameter space of perforated drag plates is first defined and then explored through a series of aeroacoustic tests conducted in the Markham wind tunnel at Cambridge University. The results and data analysis are discussed.

In Chapter 6, a prediction tool for a perforated drag rudder configuration is developed on the basis of the MIT acoustic chamber experimental results.

Conclusions and recommendation for future work are given in Chapter 7.

Chapter 2

Description of Noise and Drag Mechanisms of Perforated Drag Plates

This chapter presents the noise mechanisms and dimensional analysis of the important geometric and fluid dynamic parameters that govern the noise generation of a perforated drag plate. A drag analysis to investigate the effects of the perforations on the drag generation is also discussed.

2.1 Noise Mechanisms Associated with Perforated Drag Plates

The true sources of aerodynamic noise are the fluid disturbances themselves. The interaction of these disturbances with airframe structural discontinuities causes substantial sound radiation. It is believed that there are three major noise source mechanisms associated with perforated drag plates:

- **Bluff-body noise** due to the flow separation at the side edge. The unsteady motions in the shear layer are a major noise source.

- **Turbulence mixing noise** by the individual jetlets that comprise the perforated drag plate and their interaction with the bluff-body wake.

- **Panel vibration noise** due to the mechanical vibration of the plate.

The difficulty is that these noise mechanisms are interacting with one another. This makes their individual identification very complicated. On the other hand the strong coupling is the reason why a noise reduction could be achieved (see Section 1.2).

Characteristics of the individual mini-jet nozzles that comprise the perforated drag plate are jet-to-jet shielding and coalescence into a larger jet. This is a critical factor in order to realize acoustic suppression from any distribution of the perforations. Without enough separation of the mini-jets, they will coalesce into a larger jet with a noise signature more characteristic of a single larger jet rather than many small jets.

Different designs of perforations will have different effect on the perforated drag plate noise signature. Having perforations closer to the drag plate edges will relieve the pressure distribution and this affects the vortex shedding from the edge. Thus, in order to fully understand the noise generation of a perforated drag plate different perforation patterns need to be tested. The relation of the separation and the perforations' diameter that gives satisfactory acoustic suppression without considerable drag penalty is what needs to be found.

Another significant noise mechanism of the perforated drag plate is associated with panel vibration driven by turbulent pressure fluctuations. Dowell [10] has given a simple estimate of the far-field radiation from the lowest order mode of a rectangular panel under turbulent excitations. For a panel of area 3 ft^2, he found a lowest eigenfrequency of 37 Hz and a sound pressure level (SPL) of 97 dB at a range of 300 ft. This estimate is very sensitive to the modeling of the surface pressure field, which may itself be significantly changed by the vibration, especially if the dominant radiation is from a high order panel mode. The principal sites of vibration are likely to be associated with regions in which the surface pressure modeling is probably inaccurate. Thus, the theoretical work seems of little help in those circumstances [11]. Panel vi-

bration noise is also difficult to be tested as the vibrations depend not only on the perforated drag plate design but also on the way it is secured to the wing or winglet. Thus, the current study does not focus on this noise mechanism but considers it as a possible and significant noise source.

The interaction of flow with structure, or sound generated by fluid flow is in the class of wake flows, which occur in the separated flow behind the drag plate. The wakes, highly coherent or very random, produce fluctuating forces on the element "shedding" the wake in both the streamwise (drag) and normal-to-streamwise (lift) direction. These force fluctuations may be characterized as acoustic dipoles, whose far-field sound exhibits a known dependence on frequency, amplitude, and direction (which may be determined from flow speed and element geometry). The strength of the bluff-body effects depends not only on the flight conditions such as angle of attack and flight speed but also on the spoiler/drag rudder location because of the interaction with local flow. The noise signature of the bluff-body effect could be modeled by an array of independent acoustic point dipoles along the surface of the plate.

As mentioned before, the main challenge is that these noise mechanisms are interacting with one another which makes their individual identification very complicated. This complication is reduced then by a dimensional analysis identifying the important non-dimensional groups that govern these noise mechanisms.

2.2 Dimensional Analysis

The optimal perforated drag plate is one that achieves a balance of reducing the noise without sacrificing the drag generating ability of the plate. In order to find the optimal design the critical parameters that describe the noise mechanisms associated with a perforated plate need to be determined.

Dimensional analysis offers a method for reducing complex physical phenomena to a simple form prior to obtaining a qualitative answer. The premise of this type of analysis is that the form of any physically significant equation must be such that the

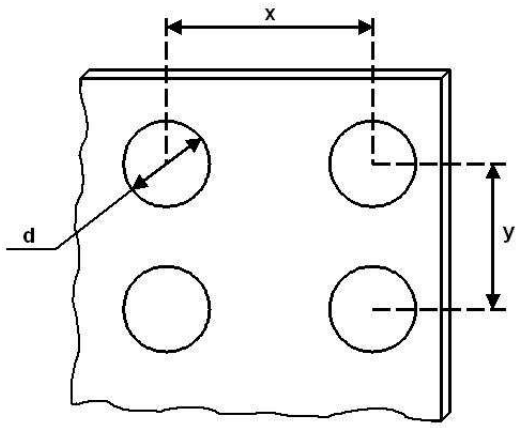

Figure 2-1: Schematic of a perforated drag plate.

relationship between the actual physical quantities remains valid independent of the magnitudes of the base units [12].

A simple non-dimensional model can provide a parametric guideline for sizing the perforated drag plates to be tested and helps predict and scale some important features of the flow and the noise generation mechanisms.

An enlarged view of a perforated drag plate is shown in Figure 2-1. In this model, the horizontal separation defined as the horizontal distance between two neighboring perforations is denoted by x. The vertical separation is denoted by y. The porosity of such a plate, defined as the ratio of the open to total area, can be calculated using the following equation

$$\beta = \frac{\pi d^2}{4xy}. \tag{2.1}$$

The parameters that are sufficient to define the flow and geometry of the perforated drag plates are: the free stream velocity U_∞ in m/s, the speed of sound a_∞ in m/s, the air density ρ_∞ in kg/m^3, the air viscosity μ in kg/ms, the diameter of the perforations d in m, the horizontal separation x in m, the vertical separation y in m, the frequency f in Hz, the deployment angle ψ in deg, the plate height H in m, the plate length L in m, the distance to an observer r in m, and directivity angle θ in deg. The deployment angle ψ is defined as the angle between the winglet axis and the drag plate axis. Figure 2-2 shows a conceptual design of perforated drag rudder used on

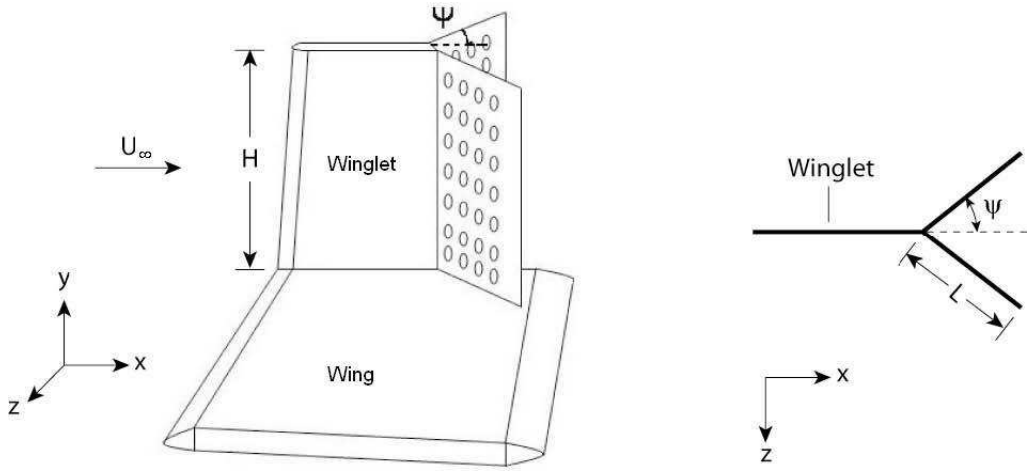

Figure 2-2: Schematic of a perforated drag rudder.

the current Silent Aircraft design.

The Buckingham π-theorem can be used to express any physical quantity of interest such as the sound pressure level, as a function of the non-dimensional quantities

$$SPL = f\left(\frac{x}{L}, \frac{y}{L}, \frac{fL}{U_\infty}, \frac{\rho_\infty L U_\infty}{\mu}, \frac{U_\infty}{a_\infty}, \frac{d}{L}, \frac{H}{L}, \psi, \theta, \frac{r}{L}\right). \tag{2.2}$$

The third argument in Equation 2.2 is the Strouhal number

$$St_L = \frac{fL}{U_\infty}, \tag{2.3}$$

while the fourth non-dimensional group is the Reynolds number based on the length L of the perforated drag plate

$$Re_L = \frac{\rho_\infty L U_\infty}{\mu}. \tag{2.4}$$

The equation for the porosity, β, expressed using the non-dimensional parameters is as follows

$$\beta = \frac{\pi}{4}\left(\frac{d}{L}\right)^2 \left(\frac{x}{L}\right)^{-1} \left(\frac{y}{L}\right)^{-1}. \tag{2.5}$$

For the simple case of a square plate with a uniform perforation pattern (see Figure

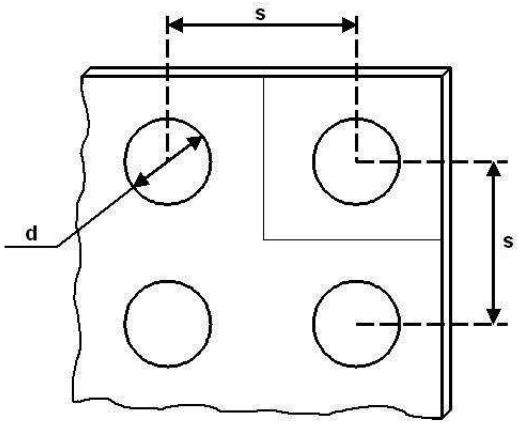

Figure 2-3: Square perforated drag plate schematic with uniform perforation pattern

2-3), Equations 2.2 and 2.5 simplify to the following

$$SPL = f\left(\frac{s}{L}, St_L, Re_L, M, \frac{d}{L}, \psi, \theta, \frac{r}{L}\right), \tag{2.6}$$

$$\beta = \frac{\pi}{4}\left(\frac{d}{L}\right)^2\left(\frac{s}{L}\right)^{-2}. \tag{2.7}$$

An $L \times L$ perforated square plate with a uniform perforation pattern consists of N small $s \times s$ squares plates (Figure 2-3). Therefore,

$$\frac{s}{L} = \sqrt{\frac{1}{N}}. \tag{2.8}$$

Thus, s/L in Equation 2.6 takes only discrete values. The exact forms of (2.2) and (2.6) can be discovered by experimentation or by solving the problem theoretically. The forms obtained so far reduce the number of variables and simplify the analysis of the situation.

2.3 Drag Analysis

It is misleading to only consider noise suppression without considering the associated performance penalty of perforated drag plates. Thus, noise assessment of potential

perforated drag devices should always be made on the same drag basis. For this purpose, a drag analysis is conducted to investigate the effect of perforations on the drag generation of such perforated plates. For the current study, it was hypothesized that the plate drag coefficient depends only on the plate porosity and an analytical expression exists that captures this variation. This hypothesis was based on the Taylor's theory [13]. Considering the perforated plate to be an assemblage of uniformly spaced centers of resistance, Taylor found that

$$C_D = \frac{\kappa}{(1 + \frac{1}{4}\kappa^2)^2}. \tag{2.9}$$

Here κ is expressed in terms of the pressure drop across the plate such that

$$p_1 - p_2 = \kappa\left(\frac{1}{2}\rho u^2\right), \tag{2.10}$$

where p_1 is the static pressure on the upstream side, p_2 that on the downstream side of the plate, u the mean air velocity through it, and κ the plate resistance to a passage of air. Since the flow through the perforated plate can take place only in the holes, the resistance κ of the plate depends on its porosity. However, Equation 2.9 for the drag coefficient suggests that C_D cannot be greater than 1.0. This is not true as the drag coefficient of a high-resistance plate must approach that of a solid plate placed perpendicular to the air flow. The drag coefficient for such a bluff body was experimentally determined by Castro [14] and found to be 1.89. Taylor [13] suggests that this discrepancy may be due to the fact that the mixing of the wake with the air which has not passed through the perforated plate can increase the negative pressure at the back of the screen, and this is not modeled in his theory.

On the other hand, Eckert and Pfluger [15] found that the resistance κ takes the form

$$\kappa = \left(\frac{1 - \beta}{\beta}\right)^2, \tag{2.11}$$

where β is the porosity of a perforated plate. Davies [16] found a similar variation of

the resistance κ with porosity

$$\kappa + 1 = \frac{1-\gamma}{\beta^2 C^2}. \tag{2.12}$$

Here C is the contraction coefficient for a fluid flowing through a perforation, while γ is the fraction of the lost pressure which is regained when the stream again becomes uniform behind the plate,

$$p_2 - p_c = \frac{1}{2}\gamma\rho\left(\frac{u}{\beta C}\right)^2, \tag{2.13}$$

where p_c is the pressure in the contraction.

Equation 2.12 is consistent with Equation 2.11 since both C and γ may depend on β. Then, substituting Equation 2.11 or 2.12 in Equation 2.9, the drag coefficient can be expressed as a function of β only.

Davies [16] carried out measurements of the air resistance of perforated plates and gauzes to test this theory and to explore the connection between the resistance κ and the porosity β. He found that the data do not collapse based on Equation 2.11 given by Eckert and Pfluger. The discrepancy suggests that the jets do not recover a constant portion of their kinetic energy as it was assumed deriving Equation 2.11. He also found that for perforated plates there is a steady and slow increase in $(\kappa+1)\beta^2$ as β decreases.

Although, the variation of the resistance κ with β cannot be exactly derived and experimental data is usually used to get this variation, Taylor's theory was proved valid for $\kappa < 4$ or plates with high porosity. This suggests that there might be two regimes for the flow behind the perforated plate, one for low porosity plates and one for high porosity plates.

It is obvious that a more thorough understanding of the flow behind a perforated plate is needed in order to find the drag coefficient variation with plate porosity.

Next the physics of flow behind a perforated plate is considered. A bluff body usually sheds two shear layers which are unstable and interact in the near wake, rolling up to form a vortex street. If the two separating shear layers are prevented from interacting in the usual way, as is the case with a splitter plate, the vortex formation may be delayed and the vortex formation point moves downstream. When

the plate is perforated extra air is injected between the two shear layers and they do not meet but sill interact.

At low values of porosity the two shear layers are not prevented from interacting and they form a vortex street that will dominate the wake. As the porosity increases, more bleed air is introduced, the vorticity in the shear layers decreases. There is also a corresponding increase of base pressure and hence a decrease in drag. Thus, the vortex street strength gradually decreases when the porosity increases. This also reduces the noise levels at low frequencies that are mainly due to the vortices shed by the plate.

As the plate porosity increases, the extra air injected increases and if enough air is injected between the two shear layers, they could be prevented from interacting at all. To conserve the mass balance across the wake there still has to be a reversed flow region, and this moves downstream with increasing porosity β.

It was hypothesized that if the porosity is high enough the flow will change its characteristics from flow dominated by the vortex street to flow dominated by the turbulence or from large length scale structures dominated to small length scale structures dominated.

This change of the flow regimes was observed by Castro [14]. He investigated the flow in the wakes behind two-dimensional perforated plates. Measurements of drag and shedding frequency were made in the Reynolds number range $2.5 \times 10^4 < Re < 9.0 \times 10^4$.

The drag coefficient was defined as

$$C_D = \frac{Drag\ Force}{\frac{1}{2}\rho U_\infty^2 A}, \tag{2.14}$$

where A is the plate area.

Figure 2-4 shows a plot of the drag coefficient, C_D, as a function of $1/\beta^2$ obtained by both wake traverses and drag balance methods at $Re = 9 \times 10^4$. The expression $1/\beta^2$ was used as the ordinate since it is a relevant parameter in Taylor's theory.

Figure 2-4 shows that at high values of β the results agree well with the theoretical

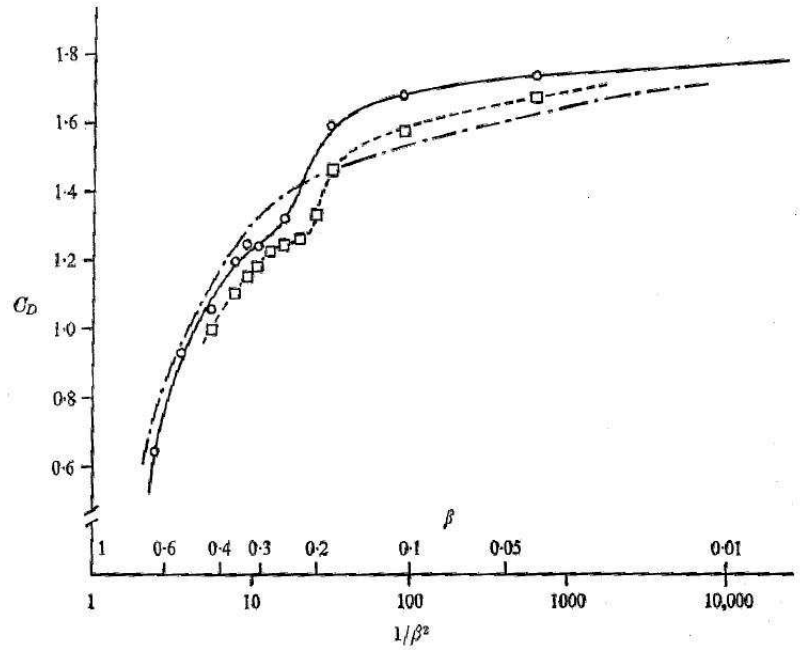

Figure 2-4: Perforated plate drag coefficient C_D variation with porosity β (Castro[14]), $-\cdot-$, Blockley[17], $-\circ-$, wake traverse method, $-\Box-$, drag balance method.

predictions by Taylor and at lower values (high $1/\beta^2$) the agreement is not so good.

By placing a hot wire outside the wake to obtain a frequency shedding signal Castro [14] also measured the vortex shedding frequency. Figure 2-5 shows the Strouhal number, defined as $St = fL/U_\infty$, where f is the shedding frequency, L the plate chord and U_∞ the free stream speed, again plotted against $1/\beta^2$. The Strouhal number was measured over a range of Reynolds number, but only the two sets of results corresponding to the two limits of the range are shown. As β increases there is a gradual increase in Strouhal number until at $\beta = 0.2$, where an abrupt reversal of slope is present. However, there is still a distinct peak in the spectrum, and only when β exceeds about 0.4 does this peak begin to spread over a range of values. At this stage it is no longer possible to pinpoint any dominant frequency [14]. Therefore, Figure 2-5 shows a band of possible values of St at these high values of porosity.

It was observed by Castro [14] that at β of about 0.2 there are quite abrupt changes in the drag coefficient and Strouhal number. Figure 2-4 shows a sudden drop in the drag coefficient. If the vortex street died gradually a smooth continuation of

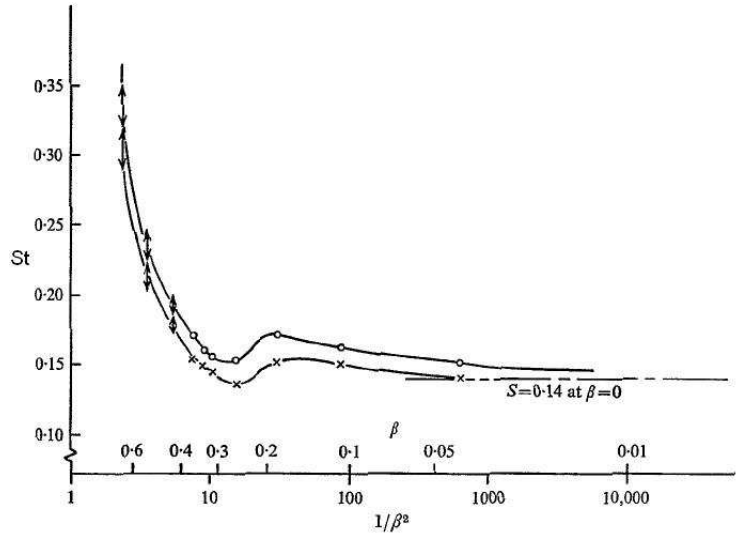

Figure 2-5: Strouhal number versus $1/\beta^2$ (Castro[14]), $-\circ-$, $Re = 2.5 \times 10^4$,$-\times-$, $Re = 9 \times 10^4$.

the drag coefficient curve at high values of β into the low β range should be present. The drag of a body shedding a vortex street is substantially higher than if the vortex street is not present, so Figure 2-4 suggests that at β of 0.2 the vortex street suddenly ceases to exist. There is a corresponding drop in the Strouhal number as Figure 2-5 suggests. Castro argues that this is a critical point, at which there is just enough bleed air to prevent the shear layer from interacting at all to form a vortex street. If this is the case, a 'shedding frequency' or 'Strouhal number' can not be defined in the same sense beyond this critical value of β, but he still found a dominant frequency probably connected with the jetlets or some sort of far wake instability.

The abrupt changes in C_D and St, observed by Castro [14], proved that there indeed exist two flow regimes behind the perforated plate, one at low porosity and the other at high porosity of the plate. The critical value of β seems to be of about 0.2. In the first flow regime, appropriate to low values of porosity, the vortex street (large length scales) dominates the wake. In the second flow regime, at high values of porosity the small length scales dominate the wake. Because a proper analytical expression for the drag coefficient was not found, data obtained by Castro [14] is used to obtain the drag coefficient for a given perforated plate in this study.

Chapter 3

MIT Acoustic Chamber Design and Instrumentation

One of the main challenges of designing quieter drag devices is that current analytical models do not accurately predict the noise that is emitted by such designs. Therefore, it is necessary to build an actual model and test it to determine any noise reduction that can be achieved by using perforated drag plates.

Conducting aeroacoustic tests in Markham wind tunnel at Cambridge University, equipped with a phased microphone array is expensive and requires careful planning. The test articles should be sized properly to yield noise spectra above that of the wind tunnel background noise and within the desired frequency range. Thus, low cost acoustic tests were first conducted at MIT to get preliminary results of the noise characteristics associated with perforated drag plates.

Aeroacoustic tests of perforated plates mounted on a horizontal plate in a spoiler configuration were conducted in the MIT acoustic chamber placed in front of the 1-by-1 Foot Low-Speed Wind Tunnel. These preliminary results were then used to derive the first scaling laws and to size the test articles for the detailed aeroacoustic tests in the Markham wind tunnel.

The main purpose of the MIT acoustic chamber is to minimize the effect of ambient noise on test article noise measurements driven the 1-by-1 Foot Low-Speed Wind Tunnel. The chamber is located inside the Gerhard Neumann Hangar and Laboratory

at MIT. This chapter introduces the design of the MIT acoustic chamber, microphone and associated support instrumentation, measurement technique and characterization of the MIT acoustic chamber.

3.1 Acoustic Facility Design

The goal in source characterization is to determine quantities that are independent of the particular acoustical environment or installation. This permits the prediction of characteristics in other environments or installations.

Reflections and reverberations from surrounding objects produce standing waves at the point of observation. Such distortions are caused by interaction between the directly incident wave and the returning reflections. In order to make measurements in a free-field, without reflecting objects, the measurements must be made outdoors at the top of a flagpole or in an anechoic chamber.

Originally, the MIT acoustic chamber was constructed for an undergraduate project [18]. The ceiling, floor and all the walls of the chamber are covered with acoustic foam forming wedges of $\sim$5 cm size such that the small reflections with the wall are directed again and again into the absorbent material until essentially all the energy is absorbed. In such an anechoic environment, sound simply travels outward and away from the source, with no return and without the presence of interfering reflections.

Figure 3-1 shows the inside of the acoustic chamber with a perforated drag plate test configuration. A more detailed drawing is presented in Figure 3-2. The duct inside the acoustic chamber attaches to the MIT 1-by-1 Foot Low-Speed Wind Tunnel. With the help of brackets and adhesive sealant between them air is prevented from bleeding. There is a rectangular opening at the wall opposite the duct through which the wind tunnel jet exhausts to the outside. Figure 3-2 also shows four thin aluminum arcs on which 12 microphones are mounted. The microphone assembly is discussed next.

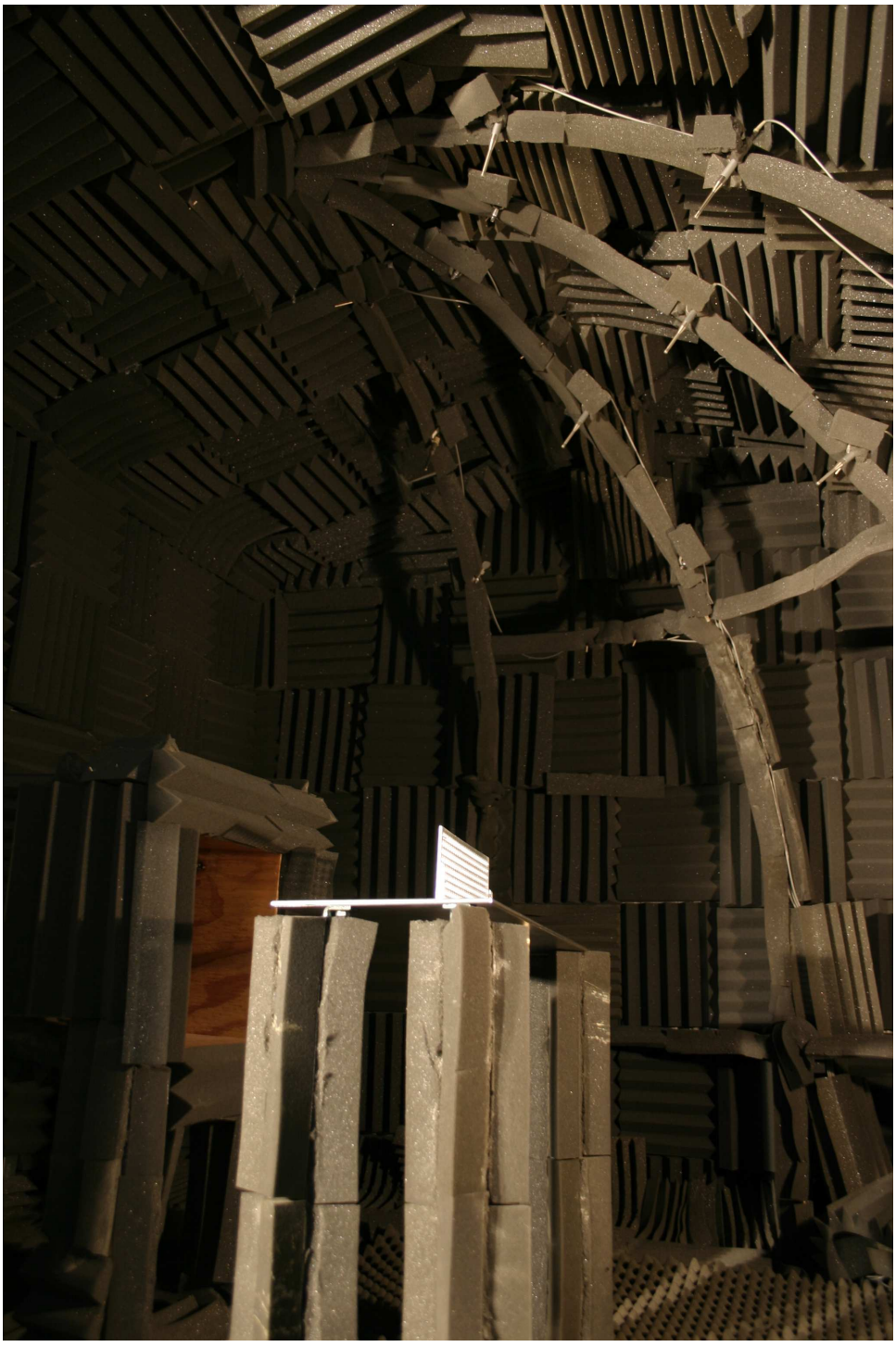

Figure 3-1: MIT acoustic chamber and perforated drag plate test configuration.

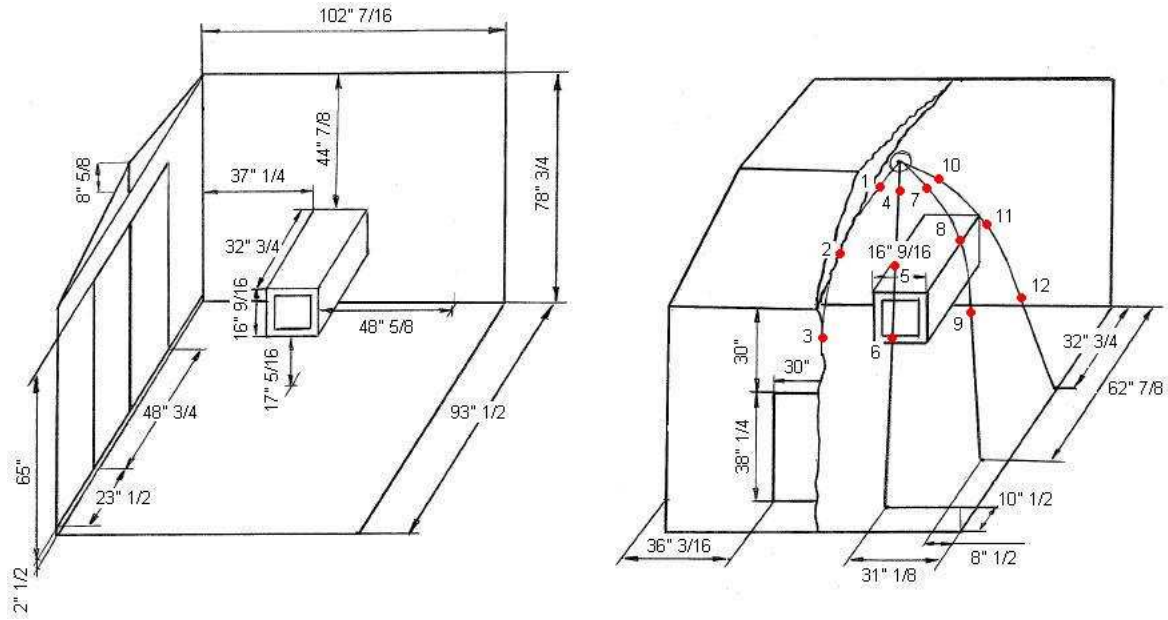

Figure 3-2: Detailed drawing of the MIT acoustic chamber. Red dots indicate microphone locations.

3.1.1 Microphone Placement

An important characteristic in aeroacoustics is source directivity because what might be perceived as a noise reduction at one location could be a shift in acoustic energy from one direction to another. Ideally, a map of the sound field on a sphere surrounding the noise source is desired. However, when there is symmetry in the noise field, as is the case for the perforated spoiler tests performed in this study, the microphones can be distributed on a one-eighth sphere.

The microphone array (see Figure 3-2) in the MIT acoustic chamber was arranged to create an eight-sphere with radius 1.5 m. The center of the sphere is the wind tunnel duct exit. The entire aluminum microphone mount was attached directly to the roof of the acoustic chamber. The twelve microphones and their azimuthal and elevation position are tabulated in Table 3.1. Throughout this thesis the microphone locations are referred to by their angle of azimuth and elevation.

Next, the acoustic instrumentation used in the preliminary aeroacoustic tests is discussed.

Table 3.1: Microphone position.

Microphone Number	Microphone Location
1	(0°, 75°)
2	(0°, 60°)
3	(0°, 45°)
4	(30°, 75°)
5	(30°, 60°)
6	(30°, 45°)
7	(60°, 75°)
8	(60°, 60°)
9	(60°, 45°)
10	(90°, 75°)
11	(90°, 60°)
12	(90°, 45°)

3.2 Acoustic Instrumentation

This section outlines the microphones used, the calibration procedures and the associated data acquisition system.

3.2.1 Microphone Instrumentation

All acoustic measurements at MIT were conducted using Brüel & Kjær (B&K) 4135, 1/4 inch free-field microphones, which are able to measure the sound pressure levels over a frequency of 4 Hz through 100,000 Hz. Table 3.2 summarizes some of the key properties for this type of microphone.

The B&K 4135 is a condenser type microphone. The small 1/4" diameter provides higher limits for the frequency and dynamic ranges, at the expense of a lower sensitivity. B&K 4135 has very high relative impedance and linearity. Some of the advantages of this type of microphone are the stability (holds calibration), low sensitivity to vibration and the wide range.

B&K 4135 microphones are sensitive to temperature and pressure variations, relatively fragile and require high polarizing voltage and impedance-coupling device near the microphone. These microphones obtain the charge for the electric field from a

Table 3.2: Summary of the key specifications for B&K 4135 microphones [19].

Microphone Property	**Description / Value**
Frequency Response Characteristic	Free-field 0° Incidence and Random Incidence
Open Circuit Frequency Response[a] (2dB)	4 Hz to 100 kHz
Open Circuit Sensitivity	4 mV/Pa
Lower Limiting Frequency (-3 dB)	0.3 Hz to 3 Hz
Cartridge Thermal Noise	29.5 dB
Resonance Frequency[b]	100 kHz
Polarization Voltage	200 V

[a]Not for random incidence.
[b]90° phase shift of pressure characteristic.

DC power supply connected to the microphone via the preamplifier [19]. This DC power is provided by the Microphone Multiplexer Type 2822. Due to the high charge resistance of the preamplifier, the charge build-up on the backplate is not instantaneous. Thus, the externally polarized B&K 4135 microphone only reaches the correct working voltage after about one minute. Before this time a microphone may not be within specification.

When using a B&K 4135 microphone, the microphone should be pointed towards the source. Figure 3-3 shows the free-field corrections for a B&K 4135 microphone with incidence angle. For the conducted experiments, the microphones were oriented at zero incidence angle to the source/test article and grid caps were left on to protect the microphone.

The microphones are connected to a 1/2 inch B&K 4135 preamplifier Type 2669 using a UA 0035 1/4 to 1/2 inch adapter. The preamplifier has a very high input impedance presenting virtually no load to the microphone [20]. The high output voltage together with a low inherent noise level gives a wide dynamic range. The frequency response of the preamplifier is ±0.5 dB between 3 Hz to 200 kHz. The preamplifiers are then connected to a 2669 B cable, which in turn connects to B&K Microphone Multiplexer 2822. A schematic of the microphone assembly and associated hardware support is shown in Figure 3-4. A BNC cable connects the Multiplexer 2822 with the data acquisition system (DAQ) used for the acoustic experiments conducted at MIT.

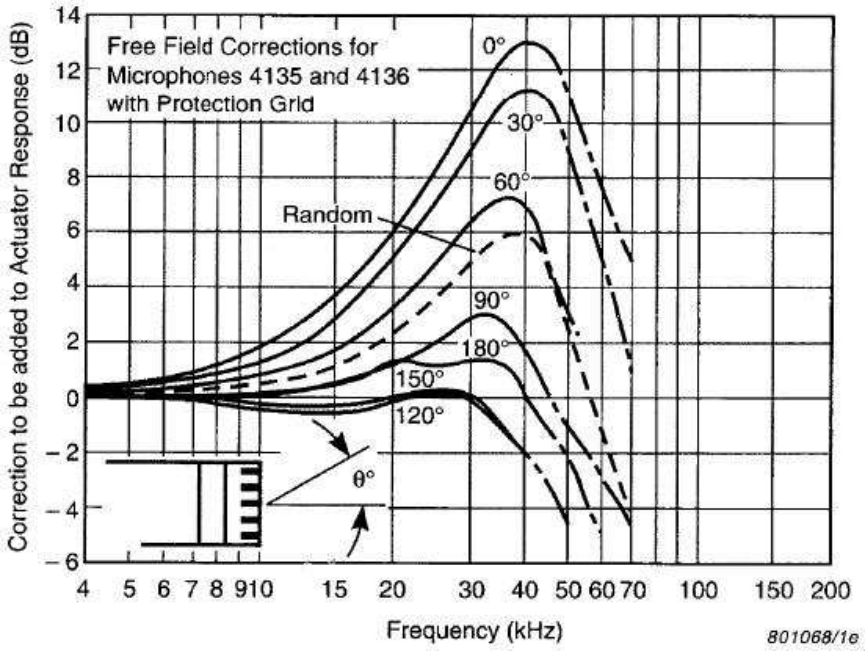

Figure 3-3: Free-field corrections for B&K 4135 microphones with protection grid [19].

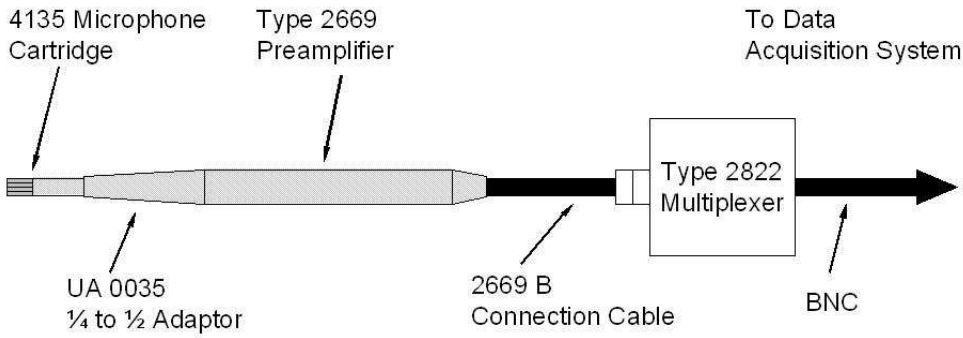

Figure 3-4: Microphone system schematic and associated hardware support.

Table 3.3: Channel, speed, and resolution specifications for a NI PCI-6143 DAQ card [21]

PCI-6143 DAQ Property	Description / Value
Bus	PCI, PXI
Analog Inputs	8
Input Resolution	16 bits
Sampling Rate	250 kS/s per channel
Input Range	±5 V
Digital I/O	8
Counter/Timers	two 24-bit
Trigger	Digital

3.2.2 Data Acquisition System

The output signal from the multiplexer through a BNC cable is fed into a National Instruments BNC-2110 shielded connector block. A SHC68-68-EP Noise-Rejecting, Shielded Cable connects the NI BNC-2110 to the NI PCI-6143 DAQ card. The NI PCI-6143 is a high-speed continuous data logging (speeds of 2 MS/s aggregate per board) card that has high dynamic accuracy and simultaneity. Table 3.3 summarizes the specification details of a NI PCI-6143 DAQ card.

Figure 3-5 shows the block diagram describing how the sound data was actually acquired. As depicted, the signal from the microphone is first transmitted through a preamplifier and a multiplexer. The multiplexer acts as an interface to the DAQ board. The DAQ board converts the signal into a digital format and feeds it into the NI LabVIEW® program run by a PC. The NI LabVIEW® program controls the DAQ card by the sampling parameters, defined by the user.

Selection of Sampling Parameters

The two sampling parameters that can be chosen are the sample rate f_s and the number of points recorded, N. The sample rate, $f_s = 1/\Delta t$, is the frequency with which samples are recorded.

The highest frequency resolved at a given sampling frequency is determined by

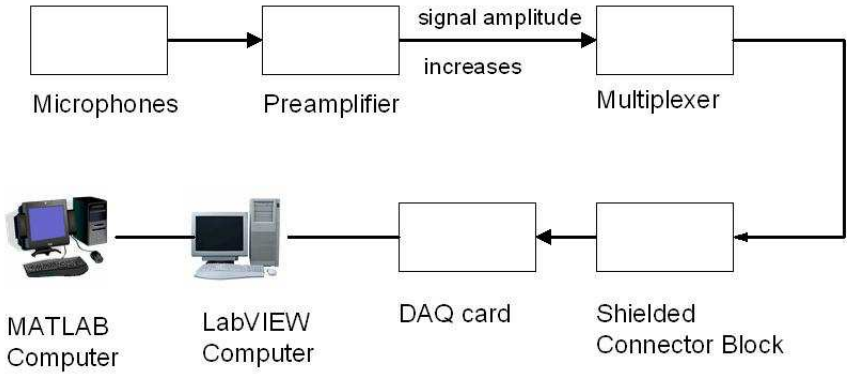

Figure 3-5: Sound data acquisition schematic.

the Nyquist frequency,

$$f_{Nyq} = \frac{f_s}{2}. \tag{3.1}$$

Signals with frequencies lower than f_{Nyq} are accurately sampled but signals with greater frequencies are not. The frequencies above f_{Nyq} incorrectly appear as lower frequencies in the discrete sample and the phase ambiguity prohibits sampling even at the Nyquist frequency itself. To prevent these problems, the sampling rate should always be chosen to be more than twice the highest frequency in the measured signal.

The sample rate of the equipment was chosen to be 50 kHz. Thus, the maximum frequency that the microphones could accurately detect is 25 kHz. This was a tradeoff between saving data acquisition time and yield a wide test frequency range.

The acquisition time is essentially determined by the speed at which the NI LabVIEW® program can write the microphone voltage data into text files. An ensemble average was used over 200 voltage spectra to remove any random noise from the spectra of the test articles, as will be discussed later. It takes approximately 20 minutes for the LabVIEW® program to write 200 text files with the voltage data of 7 microphones, at the sample rate and the choice of frequency resolution.

After the sample rate is chosen, the frequency resolution has to be determined. The frequency resolution, $\Delta f = f_{lowest}$, is both the lowest frequency in the discrete signal and the spacing of frequencies in the signal. It determines how accurately the frequency components in the signal are resolved.

When a signal is recorded by a computer, only discrete points are stored. The number of points N in the sample to yield the desired

$$\Delta f = \frac{f_s}{N} \tag{3.2}$$

at the previously determined value of the sampling frequency can be calculated. The samples will be taken at intervals of $\Delta t = 1/f_s$ covering a period of $N\Delta t$.

In order to get narrow band resolution the number of discrete points was chosen to be $N = 2^{15}$. The number of points is a power of two so that the Fast Fourier Transform (FFT) can be used and save computation time. This N then gives a resolution of $\Delta f = 1.5$ Hz.

The raw sound data obtained from the microphone setup was a voltage time signal. A LabVIEW® DAQ program that was used records the sample rate at which the measurements were taken, along with amplitude of the voltage signal sent by each microphone at each time interval. This information was then saved in a text file, as already mentioned. Then the voltage magnitudes were transformed into the corresponding sound pressure level readings using the data reduction technique discussed next.

Data Reduction Technique

The data reduction was done primarily through the use of a MATLAB® script, which performs several functions necessary to adequately reduce the data. The first step in analyzing the data was to remove the mean value from the time signal.

The emitted sound is a combination of sound waves with different amplitudes and frequencies. After measuring a complex waveform the task is to determine the frequency content. These frequencies may be described using the frequency spectrum, which shows the amplitude of each frequency component. Thus, the second step was to convert the saved voltage time signal into a frequency spectrum by using a Fast Fourier Transformation (FFT).

Before converting to a frequency spectrum, a window/filter needs to be applied.

Table 3.4: Time domain characteristics of rectangular and Hanning weighting functions [22].

Window	**Max. Amplitude**	**Min. Amplitude**	**Effective Duration**
Rectangular	1	1	1×T
Hanning	2	0	0.375× T

Table 3.5: Frequency domain characteristics of rectangular and Hanning weighting functions [22].

Window	**Noise Bandwidth**	**3 dB Bandwidth**	**Ripple**	**Highest Sidelobe**	**Sidelobe Fall-Off rate per Decade**	**60 dB Bandwidth**	**Shape Factor**
Rectangular	Δf	$0.89\Delta f$	3.92 dB	-13.3 dB	20 dB	$665\Delta f$	750
Hanning	$1.5\Delta f$	$1.44\Delta f$	1.42 dB	-31.5 dB	60 dB	$13.3\Delta f$	9.2

The weighting function/window, is applied to the data record to be analyzed, i.e. the data is multiplied by the weighting function. The data record (block) is T seconds long and the filters are separated by $\Delta f = 1/T$ Hz.

When no filter is applied then all data points are equally weighted. This weighting, also known as a rectangular weighting is defined as:

$$w(t) = \begin{cases} 1, & 0 \leq t < T \\ 0, & \text{elsewhere.} \end{cases} \tag{3.3}$$

This filter has a mainlobe, which is twice the width of the filter spacing Δf, and an infinite number of sidelobes with widths equal to the filter spacing. For the analysis of harmonic signals this is a poor filter because it has: (1) a very poor selectivity, due to the wide 60 dB bandwidth, and (2) a relatively large (3.9 dB) ripple in the passband. The rectangular window is a bad choice of window due to its poor filter characteristics. Thus, a Hanning window was applied to the microphone time signal to minimize the measurement errors. Table 3.4 lists and compares the rectangular and Hanning window functions in the time domain, while Table 3.5 lists and compares the same window functions in the frequency domain.

The relatively narrow mainlobe and low sidelobes of the Hanning window give the

lowest possible leakage that causes underestimation of the peak value [22].

The Hanning window is a smooth window function which is defined as:

$$w(t) = \begin{cases} 1 - \cos 2\pi t/T, & 0 \leq t < T \\ 0, & \text{elsewhere.} \end{cases} \tag{3.4}$$

As can be seen, the Hanning window is a sum of a rectangular window and one period of a cosine of equal amplitude (i.e. the sum of a DC and an AC component). The mainlobe is $4\Delta f$, double the width of the rectangular window. The number of filters will always be greater than or equal to three. The first sidelobe is much more attenuated, and the fall-off rate is much faster, than for rectangular weighting. This means that the 60 dB bandwidth is much narrower giving far better selectivity. The Hanning window performs better than the rectangular window with respect to selectivity, passband ripple and apparent leakage. The Hanning weighting function is also easy to implement and gives a high real-time rate.

Next, FFT was used to find the voltage spectrum from the time signal. After a magnitude window compensation was applied, 200 voltage spectra were overlapped and the average voltage spectrum was found. All random signals which might have contaminated the test article spectra during acquisition were removed by ensemble averaging of the spectral data.

The averaged voltage magnitudes were then transformed into the corresponding sound pressure level readings using the data obtained during the calibration of the microphones, discussed in the next section. The voltage output of the microphones is equal to the pressure measured by the microphones, p_{mic}, multiplied by a constant, K_{mic},

$$V_{mic} = K_{mic} \times p_{mic}. \tag{3.5}$$

Once the voltage frequency spectrum is converted to a SPL frequency spectrum, a correction filter was applied to remedy the slight drop-off in the response of the microphones at high frequencies. The correction filter is simply the negative of the microphone response chart. The roll-off correction filter was plotted at several differ-

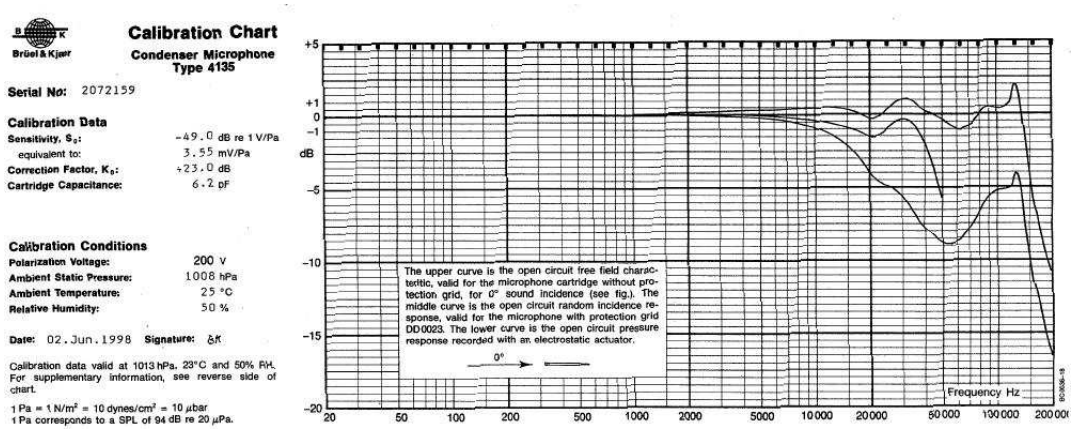

Figure 3-6: Example calibration chart delivered with the condenser microphone cartridges [19].

ent points on the frequency spectrum. A best-fit curve in the form of a sixth-degree polynomial was then found, and this filter was applied to the frequency spectrum. Free-field corrections were also added to the pressure response of the microphones in order to obtain the free-field response at a particular angle of incidence using a best-fit curve line in the form of a seventh-degree polynomial.

After all SPL spectra were found, MATLAB® was used to create plots of sound pressure spectra. These plots were then used to determine any changes in the acoustics of the tested articles.

3.3 Microphone Calibration

The microphones must be calibrated in order to provide precise and accurate measurements. A sample calibration chart for one B&K 4135 microphone is shown in Figure 3-6. The upper curve is the open circuit free-field characteristic, valid for the microphone cartridge without the protection grid, for 0° sound incidence. The middle curve is the open circuit random incidence response, valid for the microphone with protection grid DD 0023. The lower curve is the open circuit pressure response recorded with an electrostatic actuator.

As can be seen from Figure 3-6, the response of the B&K 4135 microphone rapidly

rolls-off around 100 kHz. The calibration curves shown was taken into account in the acoustic data processing, which was discussed in the previous section.

Calibration coefficients K_{mic} for each microphone were obtained by placing a portable acoustic calibrator B&K pistonphone type 4228, directly over the microphone. These calibrators, in which one or more mechanically driven pistons produce a known time-varying volume displacement in a small (relative to a wavelength of sound) cavity of known volume, provide a precisely defined sound pressure level to which the microphones can be adjusted. Practical mechanical problems have limited pistonphones to use at low frequencies, on the order of 250 Hz.

High-vacuum grease, WA 0417, was applied to the adaptor base before fitting the appropriate adaptor for the B&K 4135 microphones. The nominal frequency and sound pressure level of the B&K 4228 pistonphone are 250 Hz and 124 dB, respectively [23]. This sound pressure level, given on the calibration chart for the pistonphone, is only for the reference conditions stated there. However, ambient conditions will affect the SPL, and give rise to a number of corrections. These, should therefore, be taken into account. Ambient condition corrections for pressure and load volume were taken into account during the calibration process to comply with class 1L laboratory experiments,

$$SPL_{actual} = SPL_{stated} + \Delta L_p + \Delta L_v. \tag{3.6}$$

The most significant factor affecting the pistonphone SPL, is the ambient pressure. Generally, the pressure correction, ΔL_p, can be derived as:

$$\Delta L_p = 20 \log_{10} \left(\frac{p_a}{1013hPa} \right) dB, \tag{3.7}$$

where p_a is the actual atmospheric pressure. When the B&K pistonphone type 4228 is used as a class 1 calibrator, the correction for ambient pressure can be obtained in a faster and simpler way using Correction Barometer UZ0004. For ambient pressure within the range from 650 hPa to 1080 hPa, the correction for ΔL_p in dB can be read directly from the barometer scale.

The factory calibration is valid for an effective load volume of 1.333 cm^3 [23].

However, different microphones represent different load volumes. The microphone load volume correction is given by:

$$\Delta L_v = -20 \log_{10} \left(\frac{V_{load} + 18.400 cm^3}{19.733 cm^3} \right) dB, \tag{3.8}$$

where V_{load} is the actual effective volume (the sum of the front volume and the microphone equivalent volume). For B&K 4135 1/4 inch free-field microphones used in the acoustic chamber experiments, the correction for the load volume is 0.0.

The pistonphone produces a certain pressure level, p_{pp}, which in turn produces a sinusoidal voltage signal with magnitude V_{pp}, which is easily obtained using a *Textronix TDS* 210 oscilloscope,

$$V_{pp} = K_{mic} \times p_{pp}. \tag{3.9}$$

Using the corrected sound pressure level at the microphone, the actual pressure of the sound waves emitted by the pistonphone can be calculated according to

$$10 \log_{10} \frac{p_{pp}^2}{p_{re}^2} = SPL_{actual}, \tag{3.10}$$

and

$$p_{pp} = p_{re} \times 10^{(SPL_{actual}/20)}, \tag{3.11}$$

where p_{re} is the reference pressure equal to 2×10^{-5} Pa. Now using the value for p_{pp} and Equation B-1, the value of K_{mic} is then determined, following

$$K_{mic} = \frac{V_{pp}}{p_{pp}}, \tag{3.12}$$

and

$$K_{mic} = \frac{V_{pp}}{p_{re} \times 10^{(SPL_{actual}/20)}}. \tag{3.13}$$

A MATLAB® script was used to compute the calibration coefficient for each microphone, taking into account the correction for ambient pressure and the correction for load volume after the data has been obtained using a LabVIEW® code. The scan rate and the number of samples to read during the calibration procedure were

Table 3.6: Summary of B&K 4135 microphone calibration coefficients, both factory and measured.

Serial Number	Sensitivity	Correction Factor	Cartridge Capacitance	Factory Calibration Coefficient	Measured Calibration Coefficient
2072161	-48.5 dB	+22.5 dB	6.3 pF	3.76 mV/Pa	3.2509 mV/Pa
2072154	-48.8 dB	+22.8 dB	6.3 pF	3.63 mV/Pa	3.1282 mV/Pa
2072155	-48.0 dB	+22.0 dB	6.1 pF	3.98 mV/Pa	3.4864 mV/Pa
2072156	-48.5 dB	+22.5 dB	6.4 pF	3.76 mV/Pa	3.1251 mV/Pa
2072157	-47.9 dB	+21.9 dB	6.4 pF	4.03 mV/Pa	3.5386 mV/Pa
2072159	-49.0 dB	+23.0 dB	6.2 pF	3.55 mV/Pa	3.1215 mV/Pa
2072160	-49.4 dB	+23.4 dB	6.4 pF	3.39 mV/Pa	2.9722 mV/Pa

$f_s = 1000$ Hz and $N = 10^6$, respectively.

The factory calibration coefficients for the seven B&K 4135 microphones used in the acoustic chamber experiments within this study are summarized in Table 3.6. Also listed in the same table are the measured calibration coefficients using the techniques described in this section.

3.3.1 Measurement Errors

Errors that may result in the actual measurements must be considered in order to reduce their impact on the accuracy of the data. The fact that B&K 4135 microphones used in this study, were designed for use at 23° C, 1013 hPa and 50% RH, and that any deviation from these conditions causes systematic error in the measurements must be taken into account. The influence of humidity on the noise measurements is less than 0.1 dB in the absence of condensation. The error resulting from varying temperatures is approximately -0.01 dB/°C. The influence of static pressure is -0.007 dB/kPa.

The absolute measurements were on the order of 20 dB, so errors resulting from variation in temperature and humidity variations likely caused an error in the noise measurements of less than 0.5%.

The main goal of the aeroacoustic tests conducted at the MIT acoustic chamber is to get preliminary results of the noise characteristics associated with perforated drag plates. These preliminary results are then used to obtain the first scaling laws and to

size test articles for the detailed CU Markham aeroacoustic tests.

Before the actual acoustic tests were conducted, a characterization study of the MIT acoustic chamber was carried out using an acoustic point source. The results of this study are presented next.

3.4 Characterization of the MIT Acoustic Chamber

One of the main challenges in taking microphone measurements is to assure that the correct sound pressure level is measured. This is connected with the microphone position with respect to the test article and the characteristics of the walls of the acoustic chamber.

It is important that the microphones are far enough from the noise source in order to ensure that only far-field noise measurements are obtained. If measurements are made too close to the source, the sound pressure may vary significantly with small change in the microphone position. This will occur at a distance less than the wavelength of the lowest frequency emitted from the source, or at less than twice the greatest dimension of the source, whichever distance is the greater. This area is the near-field of the source, and 'if possible' measurements in this region should be avoided.

If the measurements are done too far from the source, closer to the walls of the acoustic chamber, reflection from the walls and other objects may be just as strong as the direct sound from the source and accurate measurement would not be possible. This region is the reverberant-field. The free-field is located between the reverberant and the near-field and is defined as the area where the decrease in intensity of a noise disturbance is inversely proportional to the square of the distance to the source. However, it is possible that the conditions are so reverberant or the room is so small that free-field conditions do not exist.

Microphone measurements require low background noise and minimal reflections

for accurate results. In most cases, proper design of wind tunnel components and test apparatus are critical to successful acoustic measurements. The sources of wind tunnel background noise are the drive fan, wall boundary layer, test dependent hardware, and microphone self noise. The later can be associated with the microphone boundary layer, screen or cavity perturbations, electronic noise, and free-stream turbulence. The background noise level in the test chamber should be as low as possible. However, when making acoustic measurements there is always a potential for data contamination from the background noise. This section presents the details for the characterization of the MIT low-speed acoustic wind tunnel facility.

3.4.1 Facility Characterization Using an Acoustic Point Source

In order to assess the acoustic performance of the acoustic chamber simple tests were conducted to check if the chamber is anechoic over the frequency range of interest. These tests were also performed to make sure that the microphones and data acquisition system are working properly.

An monopole point source was placed in the center of the chamber and B&K 4135 microphones were positioned along rays from the source in four directions. The microphones were located at distances from 2 to 50 inches away from the acoustic point source. The four directions coincided with the four microphone positions (0°, 60°), (30°, 60°), (60°, 60°) and (90°, 60°) on the microphone array placed inside the chamber.

The monopole source was initially created to perform some diagnostic tests for the MIT shock tunnel facility [24]. The point source was made out of 1/2 inch rubber with a small speaker mounted inside. A schematic of the point source is shown in Figure 3-7. The speaker was driven using a Hewlett Packard 3312OA function generator at frequencies ranging from 100 to 16,000 Hz.

To model the constant frequency disturbance by the point source, the points source is assumed to have complete spherical symmetry with regards to the excitation of sound [25]. The symmetry of the excitation and of the environment requires that the acoustic intensity I has only a radial component I_r and that its time average $I_{r,av}$

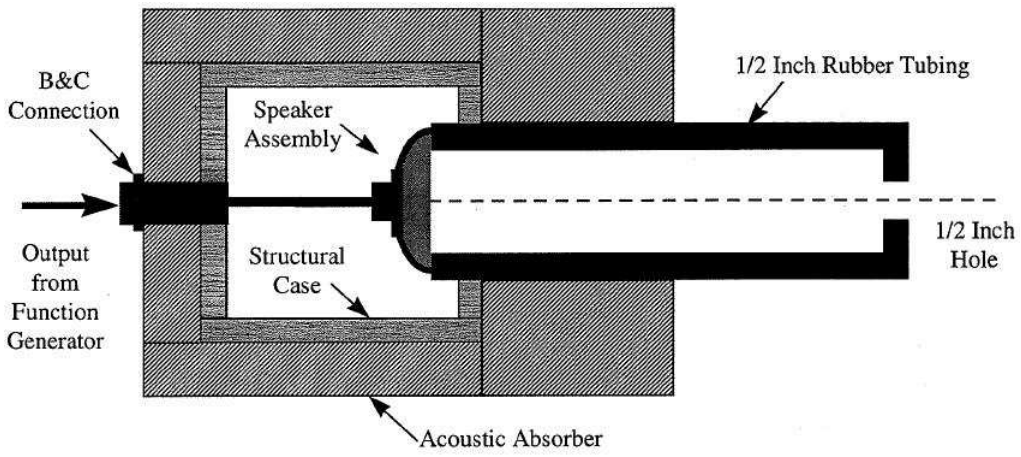

Figure 3-7: Point source schematic used in facility validation [24].

only depends on the radial distance r from the source. If P_{av} is the average power, ρ the air density, a the local speed of sound, and $p(r)^2$ the root-mean-square (rms) pressure at the same radius r, then

$$I_{r,av} = \frac{P_{av}}{4\pi r^2} = \frac{p(r)^2}{\rho a}. \tag{3.14}$$

From the conservation of acoustic energy the average power is proportional to the radial distance squared. Therefore,

$$P_{av} = \frac{4\pi r_0^2 p(r_0)^2}{\rho a} = \frac{4\pi r^2 p(r)^2}{\rho a}, \tag{3.15}$$

where r_0 is a reference radius.

On the other hand, the sound pressure level can be expressed as a function of the radial distance according to

$$SPL(r) = 10 \log_{10} \left(\frac{p^2(r)}{p_{re}^2} \right). \tag{3.16}$$

Using Equation 3.15 the sound pressure at radial distance r is obtained from the

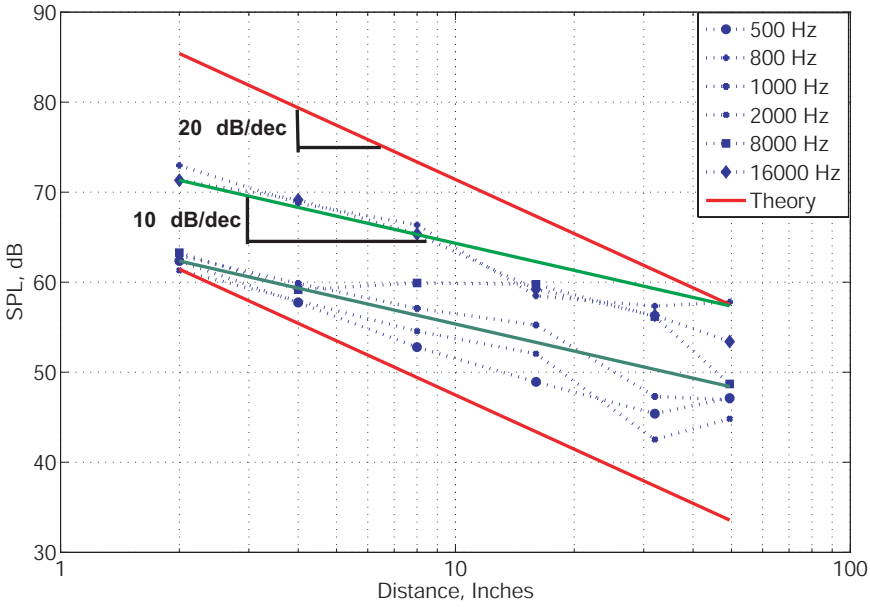

Figure 3-8: Decay of point source noise with distance for six frequencies.

sound pressure level at the reference using

$$SPL(r) = SPL(r_0) - 20\log_{10}\left(\frac{r}{r_0}\right). \tag{3.17}$$

In a free field, according to Equation 3.17, doubling the distance away from the source will drop the SPL by $20\log_{10}(2) = 6$ dB (equivalent to 20 dB/decade).

A sample of the results for microphone (30°, 60°) is shown in Figure 3-8. The acoustic data was compared to the theoretical result of Equation 3.17. The results show that the noise levels do not drop with 20 dB/dec but more on the order of 10 dB/dec which corresponds to a 3 dB drop for each doubling of the distance away from the source. A possible explanation for the deviation is that the conditions are reverberant and the chamber is too small for a free-field to exist. Other types of background noise, such as vibrations through the floor, could also affect the test data. However, the chamber was deemed good enough for the preliminary test campaign.

3.4.2 Lowest Usable Far Field Frequency

The spherical spreading rule [25] was used to determine the lowest usable far field frequency at the measurement location. If a harmonic spherical wave is considered, the impedance or the ratio of the pressure p' to velocity v_r' perturbation is

$$\left|\frac{p'}{v_r'}\right| = \frac{\bar{\rho}a}{\sqrt{1+\left(\frac{a}{\omega r}\right)^2}}. \tag{3.18}$$

Here $\bar{\rho}$ is the average density, a the speed of sound, r the radial distance and $\omega = 2\pi f$ the angular frequency. This rule states that the measurement position occurs in the far field if the spherical wave behaves like a plane wave or, equivalently, the impedance of the spherical wave approaches the impedance of a plane wave $\bar{\rho}a$. This is true for $\omega r/a \gg 1$. Then, choosing $\omega r/a = 10$ as an order of magnitude greater than 1, a basic relation can be found for f as a function of r

$$f = \frac{5a}{r\pi}. \tag{3.19}$$

Substituting $a = 340$ m/s and $r = 1$ m, the domain to obtain far-field data was determined to include all frequencies measured above 540 Hz.

3.4.3 Background Noise Considerations

The wind tunnel background noise during different hours of operation was measured and documented. A repeatability check on the background noise was performed at various times during data collection since the acoustic chamber is located in the Gerhard Neumann Hangar and Laboratory at MIT, next to other experimental facilities and the department workshop which produce varying amounts of noise depending on the time of the day.

The correction process for background noise contamination is to compare the background noise level to the noise measurement, and to subtract the background noise from the test data if the difference between the test data and background noise

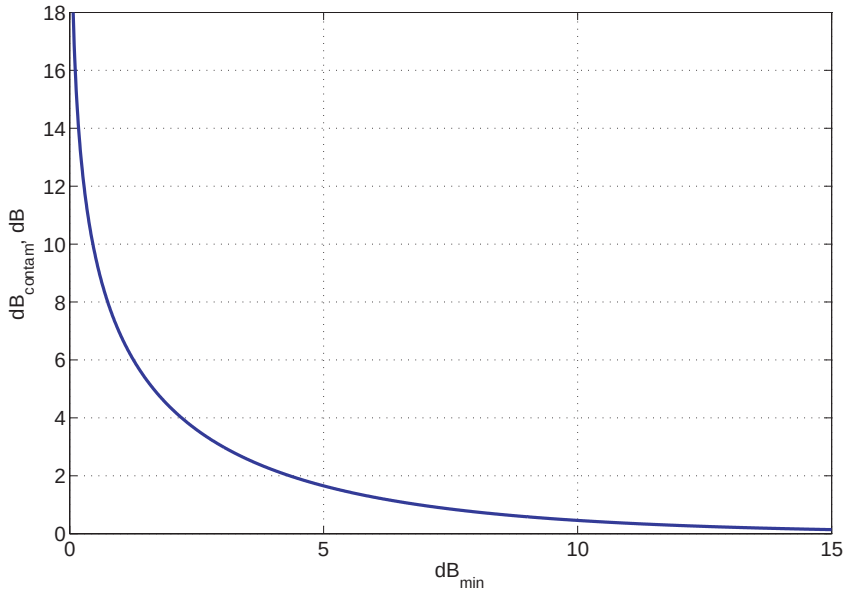

Figure 3-9: Amount of data contamination as a function of the separation between background noise and data measurement [26].

levels is larger than a certain permissible dB tolerance level, ΔdB_{min}. If the difference between the background and test data noise level is less than this permissible amount, the data should be considered contaminated. The value ΔdB_{min} is based on the repeatability of the background noise measurements. The more repeatable the background noise measurement, the smaller ΔdB_{min} can be given for a given correction accuracy [26, 24].

Once an estimate for ΔdB_{min} has been established, the amount of noise contamination ΔdB_{contam} can be determined from:

$$\Delta dB_{contam} = -10 \log_{10} \left(1 - 10^{-\frac{dB_{min}}{10}} \right). \tag{3.20}$$

Equation 3.20 can be interpreted as an estimate of the level of corruption of test data as a function of the separation between the data and the background noise (Figure 3-9).

For the MIT acoustic chamber, on average, the acoustic data was up to 10 dB above the background noise, which corresponds to at least 0.46 dB of contamination. Thus, the background noise contamination is an issue, so that it has to be subtracted

from the acoustic measurements to get the correct sound pressure level magnitude of the noise source under investigation. This is good enough for the present preliminary tests. This subtraction assumes that the source of interest and the source of background noise are not coherent and are not related to standing wave phenomena. In this case their acoustic power instead of their pressures would add together. When subtracting levels that are ΔdB_{min} apart, the higher level is always reduced by a fixed amount, independent of the absolute values (all levels are assumed positive) [26, 24].

Next the wind tunnel background noise is considered. This is important because the desired frequency test range for the MIT acoustic chamber must be identified.

3.4.4 Wind Tunnel Background Noise Measurements

Figure 3-10 shows a typical sound pressure level spectrum of the background noise. It was measured in the anechoic chamber while the wind tunnel was running at different speeds. The data is collected from microphone 6 (30°,45°) which is at 150°, measured from the wind tunnel inlet. At this location a typical peak was expected because of the waves related to large-scale turbulence structure emitted by the wind tunnel jet. Indeed, the peak frequency observed due to the 1 by 1 foot free jet does not depend on the wind tunnel velocity, and the Strouhal number, based on the speed of sound is $St_a = 0.27$. This is different from 0.19 which was found by Tam [6] for jet noise. This difference might be due to the specifics of the flow in the acoustic chamber duct. For the present purpose of doing only preliminary measurements, this was not considered an issue.

The 1-10 kHz frequency range is free of external noise such as noise due to the electronic equipment, and the background noise has a flat spectrum in this frequency range. The observed distinct peaks at 12.5 kHz are due to electronic noise and were always present in the sound pressure spectra. These peaks are outside the frequency range of interest.

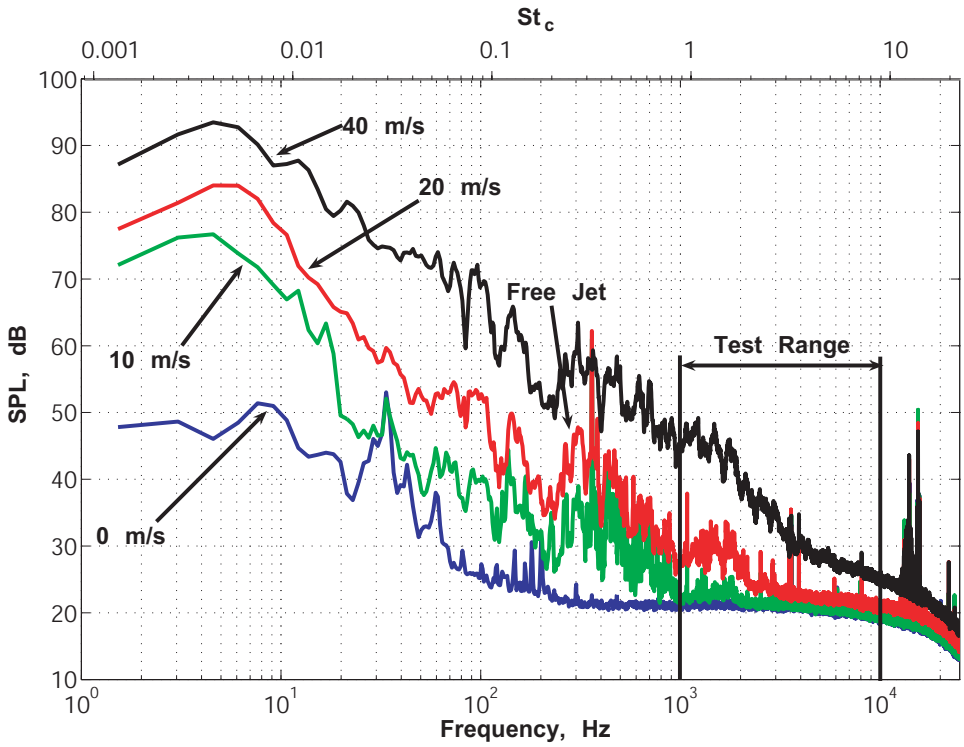

Figure 3-10: Wind tunnel background noise at 150° directivity and 1.3 m radial location.

3.5 Summary

The MIT acoustic chamber together with the microphone instrumentation and support hardware were presented and the procedure for microphone calibration along with the data reduction technique and data acquisition system were discussed.

Although the walls of the MIT acoustic chamber are covered with sound absorbing foam, the characterization of the chamber with acoustic point source shows that the microphones are not located in the free field. A possible explanation is that the chamber might be too small for free field conditions to exist and reflections from the walls interfere with the sound field. However, this was considered acceptable for the preliminary acoustic tests. Further precautions were taken to minimize the contamination of the data. For example, tests were conducted after normal working hours such that other noise from laboratory work or air conditioning would not affect the data.

Next, the domain to obtain far-field data was determined to include all frequencies measured above 540 Hz. The amount of noise contamination was established as a function of the difference between the background noise and the test article noise spectra. In the MIT acoustic chamber, on average, the acoustic data was up to 10 dB above the background noise, which corresponds to at least 0.46 dB of contamination. Thus, the background noise contamination is an issue, so that it has to be subtracted from the acoustic measurements to get the correct sound pressure level magnitude of the noise source under investigation. The subtraction should be done on an absolute basis.

It was found that the peak frequency of the noise due to the wind tunnel free jet does not change with velocity which is in agreement with observed by Tam [6]. However, when non-dimensionalized in terms of a Strouhal number, the value for the MIT 1 by 1 Low Speed Wind Tunnel facility is 0.27, which is higher compared to the data by Tam. This difference might be due to the flow in the duct not the acoustic equipment.

Finally, the desired frequency test range was identified. The 1-10 kHz frequency

range is free of external noise (such as for example noise due to the electronic equipment) and the background noise exhibits a flat spectrum. Within this frequency range the design of experiments is conducted for the preliminary experiments. The results of the preliminary experiments are discussed in the next chapter.

Chapter 4

Preliminary Experiments in the MIT Acoustic Chamber

Conducting aeroacoustic tests in CU Markham wind tunnel, equipped with a phased microphone array is expensive and requires careful planning. The perforated drag plates should be properly sized to yield noise spectra above that of the wind tunnel background noise and in the desired frequency range. Current analytical models do not accurately predict the noise that would be emitted by such perforated plates. It is necessary to build an actual model and then conduct tests to determine the noise characteristics of perforated drag plates. Thus, inexpensive aeroacoustic tests are needed to get preliminary results of the noise characteristics of perforated drag plates.

This chapter presents results obtained from the preliminary test campaign conducted in the MIT acoustic chamber. Six perforated plates and one solid plate were tested in a spoiler configuration at three different wind tunnel velocities. The results from the tests are analyzed and discussed. In addition, aeroacoustic tests to assess the interaction of the perforated plates with the shear layer of the MIT acoustic chamber open jet were also conducted and the results are also presented.

4.1 Overview of Acoustic Chamber Experiment

The idea behind a silent spoiler/drag rudder is to alter the noise production mechanism by perforating the spoilers/drag rudders. The large length scales responsible for the noise radiated by unsteady vortical structures are changed to the small length scales relevant to jet noise.

Experiment Hypothesis

The hypothesis for these preliminary experiments is that perforating the spoilers reduces low frequency noise and shifts the acoustic energy to high frequencies.

Objectives

The objectives of these experiments are to:

1. assess the acoustic benefits and impact on drag of a perforated spoiler,

2. assess the strength and if possible, determine the directivity of the noise sources (bluff-body and turbulence mixing noise) of such a perforated plate,

3. determine the scaling laws for the perforated plate noise spectra. These scaling laws will establish a prediction model for the acoustic signature of the drag devices on the current Silent Aircraft SAX10 design.

Success Goals

The main success goal is to demonstrate a net benefit in acoustic signature of perforated drag plates when compared to a solid plate generating the same amount of drag. The secondary success goal is to show that low frequency noise can be reduced and the turbulence mixing noise generated at mid frequencies is shifted to higher frequencies, where the noise is perceived less annoying by the human ear.

4.1.1 Description of the Aeroacoustic Experiments

All of the tests described in this chapter were performed in the low-speed acoustic chamber facility described in Chapter 3. Not only does the chamber reduce ambient noise, but it also reduces the variation of ambient noise, since outside noise is not heard in the chamber. The tests were performed after regular working hours in order to reduce the effect of outside noise sources to a minimum. The air conditioning system in the building was turned off and all the doors of the hangar were closed.

The aeroacoustic measurements were carried out using perforated plates mounted on a horizontal plate similar to an aircraft spoiler configuration (see Figure 4-1). The horizontal plate was mounted on four U-shaped struts, which were covered with acoustic foam to reduce the reflection of sound waves. The dimensions of the horizontal plate were 0.71 m by 0.254 m by 0.013 m. All of the horizontal plate edges were rounded to reduce sound wave scattering effects.

To assure that the correct sound pressure is measured, it is important that the microphones are far enough from the test setup so that only far-field noise measurements are obtained. Because of the small size of the MIT acoustic chamber, the horizontal plate was placed such that the microphones were at approximately 1 m from the test article. The leading edge of the horizontal plate was at 0.254 m from the wind tunnel duct exit.

The size of the low-speed wind tunnel exit limited the size of the perforated plates. For the tested plates 0.254 m by 0.125 m by 0.003 m in size the bluff-body noise, due to vortex shedding is expected to be in the 100 Hz range [14]. This is much below 540 Hz which is the lowest usable far-field frequency of the acoustic chamber. Thus, only the turbulence mixing noise mechanisms could be assessed in these aeroacoustic experiments.

In an effort to reduce the complexity of this experiment, only the porosity (the open area over the total area) of the drag plates was varied. Porosities ranging from $\beta = 0\%$ (solid drag plates) to $\beta = 60\%$ were tested. The non-dimensional characteristics of the perforated drag plates are shown in Table 4.1 together with a

Figure 4-1: Perforated plate with $\beta = 60\%$ porosity mounted in a spoiler configuration.

Table 4.1: Characteristics of the test plates.

Plate	**x/L**	**y/L**	**H/L**	**d/L**	β
Solid plate	-	-	2.0253	-	0
Perforated Plate 1	0.1680	0.2741	2.0253	0.0764	0.1085
Perforated Plate 2	0.1320	0.1645	2.0253	0.0764	0.2035
Perforated Plate 3	0.1155	0.1175	2.0253	0.0764	0.3075
Perforated Plate 4	0.0972	0.1028	2.0253	0.0764	0.4069
Perforated Plate 5	0.0880	0.0914	2.0253	0.0764	0.4974
Perforated Plate 6	0.0803	0.0822	2.0253	0.0764	0.5969

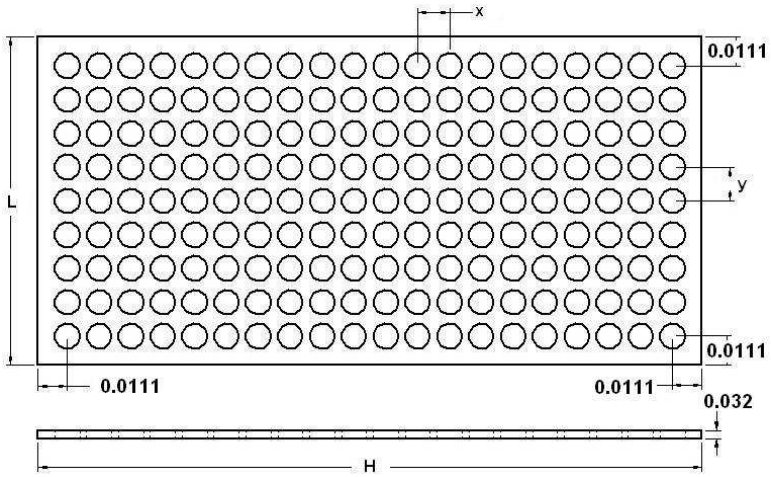

Figure 4-2: Detailed drawing of a perforated drag plate with $\beta = 40\%$ porosity (all dimensions are in meters).

detailed drawing (see Figure 4-2 of one of the plates).

The same perforation diameter $d = 0.0096$ m was chosen for all plates such that the expected peak frequency due to individual jetlets, based on $St_a = fd/a = 0.19$ [6], was within the 1-10 kHz preferred frequency test range (see Section 3.4.4). This frequency range is free of external noise as discussed earlier.

Two L-brackets were used to secure the drag plates to the horizontal plate. At the low free jet velocities of up to 30 m/s this guaranteed that the test plates were safely secured to the horizontal plate and were free of vibration. The test plan for the preliminary acoustic test campaign is presented next.

4.1.2 Preliminary Acoustic Test Campaign

Preliminary aeroacoustic tests were conducted in the MIT acoustic chamber. Six perforated plates and one solid plate were tested in a spoiler configuration at different free stream velocities. In addition, aeroacoustic tests were conducted to assess the interaction of the perforated plates with the shear layer of the open jet. These acoustic tests included noise measurements of perforated plates with some of the perforations taped in order to assess shielding effects.

During the acoustic tests the microphones not only measured the noise produced by the current test article under investigation, but also the noise reflected off the walls of the chamber and unrelated to the test article. The background noise in the acoustic chamber was always measured prior to installation of the test model (see Section 3.4.4). Acoustic measurements of the horizontal plate with and without spoilers were performed. The tests with the horizontal plate only were used as a benchmark to determine the spectra of the perforated plates in isolation by subtracting the spectra on an absolute basis.

The test matrix of the preliminary acoustic test campaign is shown in Figure 4-3. Perforated plates of seven different porosities, including the solid plate were tested. Three values of free stream velocity were examined: 15, 20 and 30 m/s. Unfortunately, the wind tunnel velocity was limited to 30 m/s, which is much lower than the current Silent Aircraft SAX10 (see Figure 1-5) approach velocity of 75 m/s. The purpose of testing at three different free stream velocities is to determine the magnitude and frequency variation of the sound spectra with airspeed in order to be able to scale them up to the approach velocity of the candidate Silent Aircraft design. Free stream velocity was used in the search for scaling laws as it is believed that this is the important velocity scale for the perforated drag plates.

The tunnel speed was determined using a pitot-static probe in the test section upstream of the acoustic chamber duct. The tunnel velocity could be held constant within $\pm 5\%$.

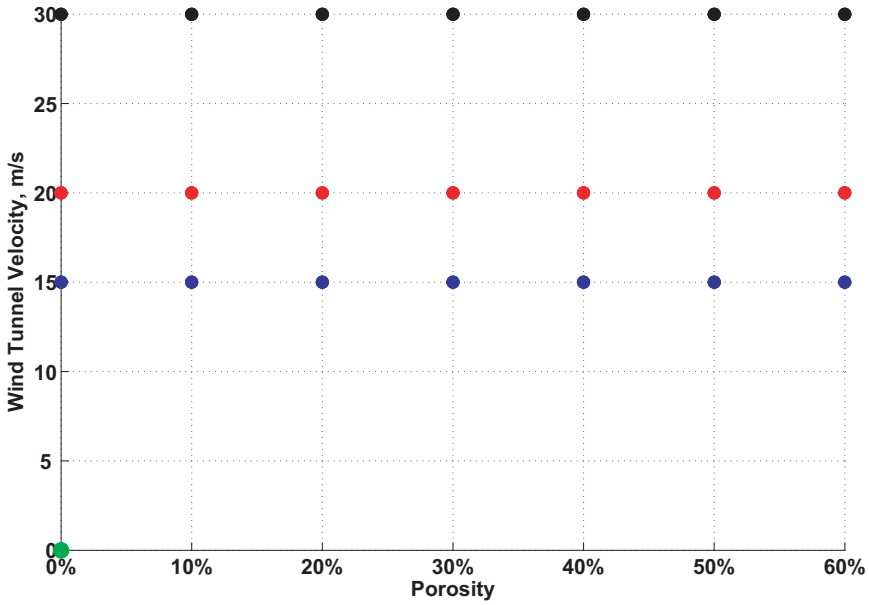

Figure 4-3: Test matrix.

4.2 Discussion of Perforated Drag Plate Spectra

This section presents the results obtained from the preliminary aeroacoustic tests of the horizontal plate with and without spoilers. The following sections are separated in terms of wind tunnel velocities tested during the preliminary acoustic test campaign.

4.2.1 Noise Spectra at 15 m/s

Figure 4-4 shows the sound spectra at a free stream velocity of 15 m/s of the horizontal plate alone and the spoilers mounted. The spectra obtained from microphone 6 (30°,45°) are plotted. This microphone was chosen to be representative since it was at 150° from the jetlets inlet axis, which is considered a location where large-scale turbulence structure/instability waves have their peak amplitude with negligible contribution of the fine-scale turbulence noise [6].

The lower set of curves corresponds to the narrowband spectra ($\Delta f = 1.5$ Hz) and the upper set of curves to the 1/3-octave-band spectra of the same measurements.

The broad peak at 300 Hz is due to the wind tunnel jet, as already discussed in Section 3.4.4. At 600 Hz there is a small peak, seen both on the narrowband and 1/3-

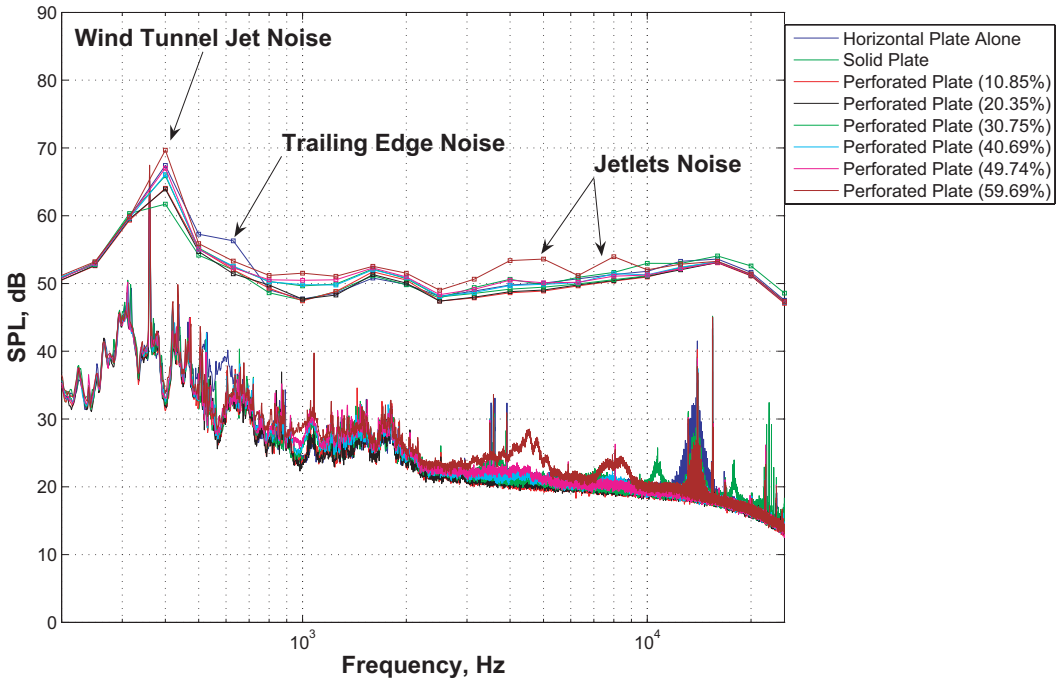

Figure 4-4: Model scale noise spectra at 15 m/s. Perforated plate porosities are shown in brackets.

octave-band spectra of the horizontal plate alone spectra. This peak was suppressed once the spoilers were mounted. Thus, it is conjectured that this peak is due to the trailing edge effects of the horizontal plate. The scaling laws for this peak were not investigated since this was not considered important in the light of the perforated plate noise characteristics.

In the mid-frequency range, 1-2.5 kHz, the noise spectra for all the spoilers and the horizontal plate have similar features and comparable noise levels. At high frequencies, above 2.5 kHz, two peaks can be seen, again clearly on both the narrowband and 1/3-octave-band spectra. The first peak is at about 4-5 kHz and the second at 8 kHz. These two peaks are seen at wind tunnel velocity of 15 m/s for the spectra of the 60% porous plate only. It is conjectured that these peaks may be due to the jetlets and their interaction with the wake behind the perforated plate. It seems that for $\beta = 60\%$ the corresponding open area is enough such that the flow injected through the plate generates noise above the wind tunnel background noise. The peak

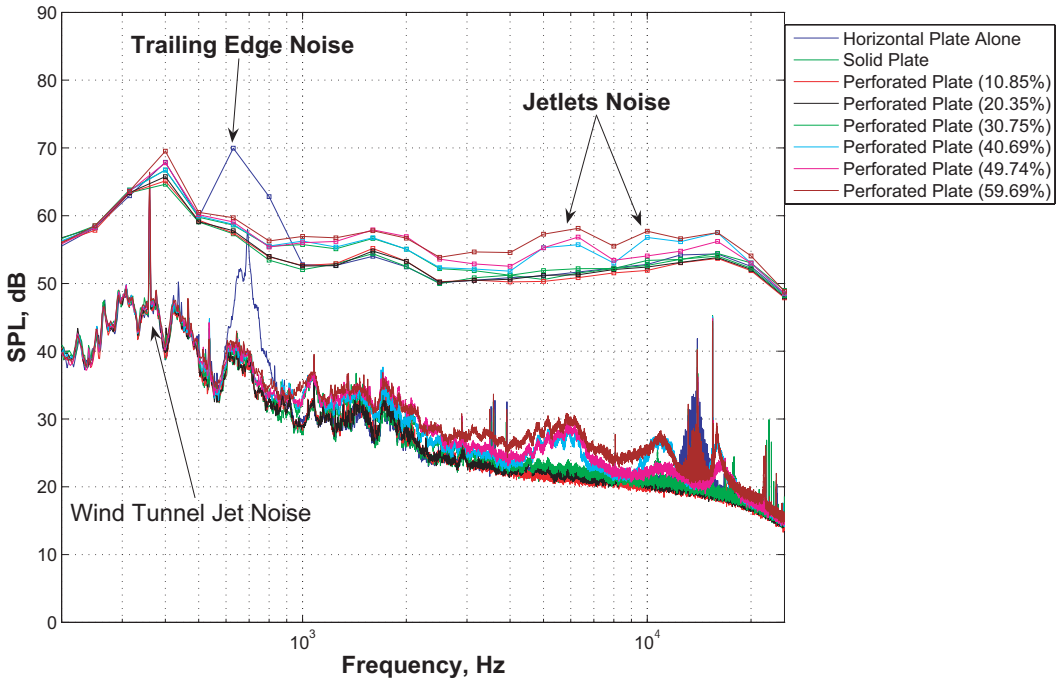

Figure 4-5: Model scale noise spectra at 20 m/s. Perforated plate porosities are shown in brackets.

at 12.5 kHz is due to electronic noise and is always present in all of the acoustic measurements.

4.2.2 Noise Spectra at 20 m/s

Distinct peaks, similar to the ones already discussed, are also present in the spectra of the test articles at 20 m/s (see Figure 4-5). The peak due to trailing edge noise of the horizontal plate is more prominent and is at 700 Hz. It can be seen that the solid and the perforated plates equally suppress the trailing edge noise of the horizontal plate.

The spectral features are similar in the mid-frequency range (with only a small difference in magnitude) and the high frequency range again exhibits two distinct set of peaks. This time the peaks occur for perforated plates with porosities of 40%, 50% and 60%. The peaks are at 5-6 kHz and 11 kHz, and there is a small increase in

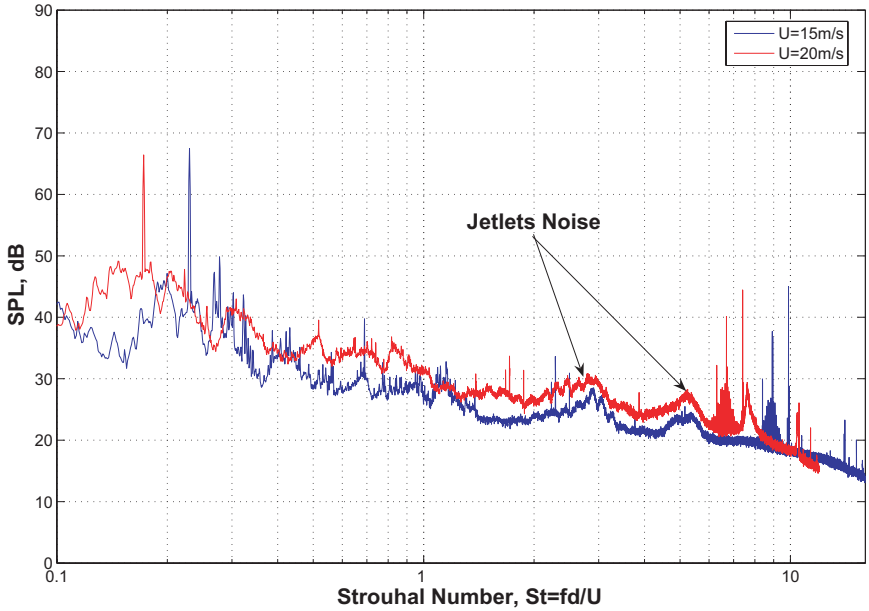

Figure 4-6: Strouhal number scaling of jetlets noise of a perforated plate with 60% porosity.

the magnitude as the porosity increases. It seems that 20 m/s is the speed at which the noise due to perforations in the 40% and 50% porous plates becomes dominant compared to the background noise of the wind tunnel.

It is also important to note that these two peak frequencies scale with velocity for a perforated plate with 60% porosity as shown in Figure 4-6. The data was scaled based on $St_d = St_L \times d/L$. This Strouhal number was used to align the high frequency features of the spectra as it is believed that the perforation diameter is the relevant length scale. It can be seen that the frequencies of these two peaks collapse on a St_d basis. The first peak Strouhal number is 2.9 whereas the second peak Strouhal number is 5.1.

4.2.3 Noise Spectra at 30 m/s

Figure 4-7 shows the sound spectra of the horizontal plate with and without spoilers at 30 m/s. The figure reveals the same spectral features (peaks), although at higher sound pressure levels and different frequencies.

In order to find the relation between the peaks observed at the three wind tunnel

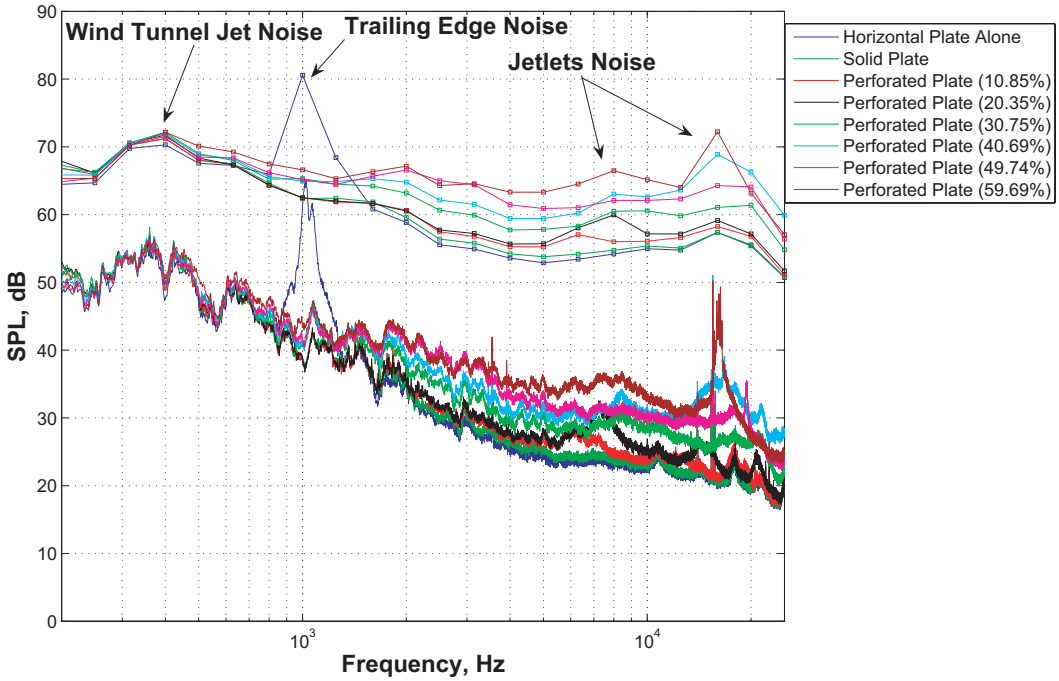

Figure 4-7: Model scale noise spectra at 30 m/s. Perforated plate porosities are shown in brackets.

velocities, the frequency scaling laws are discussed next. These are also important in the noise estimation of perforated drag plates when scaled to full size.

4.2.4 Frequency Scaling

Figure 4-8 depicts the 40% porous perforated plate spectra at different wind tunnel velocities. The data was scaled based on $St_d = St_L \times d/L$. As already mentioned, this Strouhal number was used to align the high frequency features of the spectra as it is believed that the perforation diameter is the relevant length scale. It can be seen that the frequencies of the two peaks collapse on a St_d basis. The peak Strouhal numbers are again 2.9 and 5.1 for the first and the second peak, respectively. Based on this it was hypothesized that the frequencies of the two peaks will scale as the St_d for the full scale case.

It is important to note that when scaling to full size there are two different length scales. One is the perforation diameter, d, and the other is the size of the plate, L. Thus, assuming that the full-size perforated plate has the same perforation diameter,

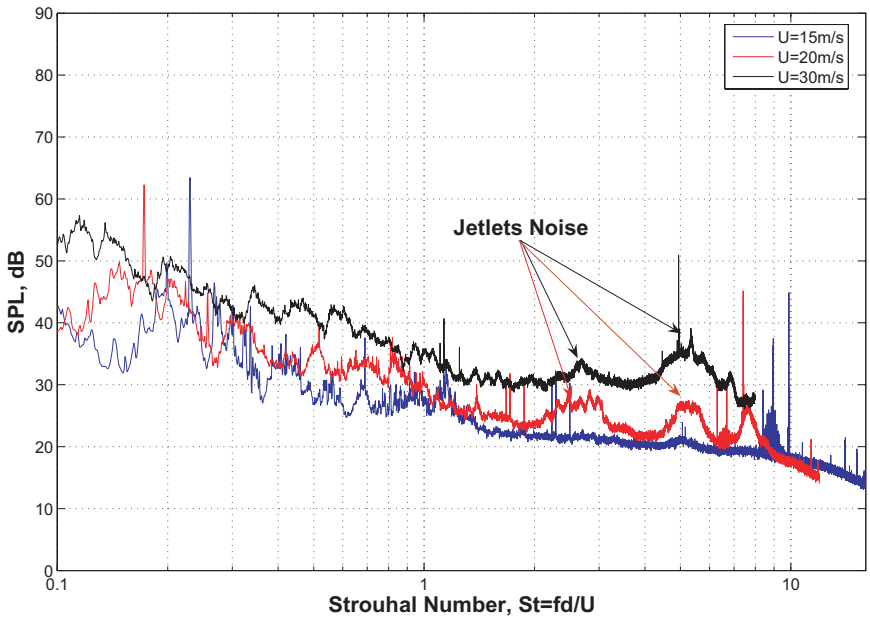

Figure 4-8: Strouhal number scaling of jetlets noise of a perforated plate with 40% porosity.

d, the SPL spectrum above 2.5 kHz scaled to full size on a St_d basis will be above 10 kHz. Thus, it can be concluded that these peaks are not contributing to the noise of the full-size perforated drag plate since 10 kHz is the highest frequency of interest for noise certification purposes.

Therefore, the mid-frequency range ($800 \leq f \leq 2500$ Hz) is the frequency range of interest and needs to be scaled to full size. It is hypothesized that this noise signature, which does not scale with St_d, must be due to the isotropic turbulence structures and hence has no directivity. A semi-empirical noise prediction tool, described in Chapter 6, was used to predict the noise signature of the full scale perforated plates at these frequencies.

In the low frequency region $0 \leq f \leq 800$ Hz the noise signature due to the wind tunnel jet noise and trailing edge noise can be seen. Unfortunately, the noise signature of the perforated drag plates are below the acoustic chamber background noise. This, combined with the fact that 540 Hz is the lowest usable far field frequency at all microphone locations, makes it impossible to determine the noise spectrum of the perforated plate in the low frequency range. In order to obtain the low frequency

content hot wire measurements were performed behind the perforated plates at distances corresponding to 1, 3 and 10 times the perforation diameter. A single hot wire was traversed vertically at each axial location behind the plate. The results were not conclusive and are not shown. In order to get the full low frequency content measurements need to be conducted further downstream, at least a couple of plate chords behind the plate. A further investigation is left for future work. In Chapter 6, an analytical noise prediction tool is discussed which was used to predict the noise signature of the perforated plates in the low frequency range.

4.3 Shear Layer Interaction and Shielding Effects

Aeroacoustic tests to assess the interaction of the perforated plates with the shear layer of the MIT acoustic chamber open jet and jet-jet shielding effects were also conducted. The results of these tests are presented here.

The shear layer originating from the wind tunnel exit develops instability waves which roll up into coherent structures. These structures merge as they are convected downstream [27]. Because of the merging the shear layer spreads.

The exit of the wind tunnel inside the MIT acoustic chamber is a 0.305 m by 0.305 m square duct. Three different values of the potential core length of the jet were assumed: 2, 3 and 4 times the equivalent diameter D_{eq}. The equivalent diameter is expressed as follows

$$D_{eq} = \sqrt{\frac{4}{\pi}H}, \tag{4.1}$$

where $H = 0.305$ m is the exit height. Figure 4-9 shows the MIT acoustic chamber wind tunnel exit, the spoiler setup and the assumed open jet potential cores.

In order to investigate the interaction of the perforated plates with the shear layer of the MIT acoustic chamber open jet, aeroacoustic measurements were conducted using the same perforated plates and test setup, described in Section 4.1.1. Only perforated plates with 40%, 50% and 60% porosities were used since only for these plates, distinct peaks above the wind tunnel background noise were observed in the

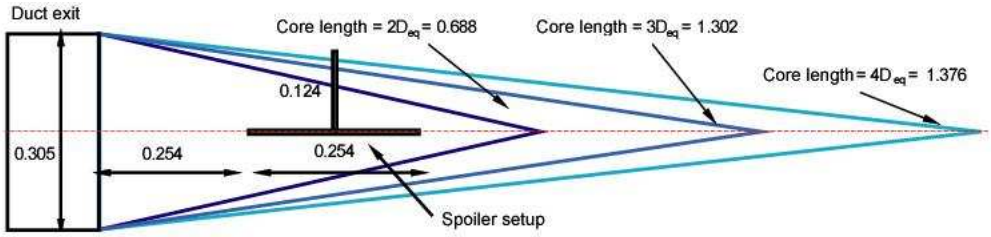

Figure 4-9: Schematic of the MIT acoustic chamber open jet. All dimensions are in meters (picture courtesy of James Hileman).

acoustic tests.

The test procedure was as follows. Initially, only the first row (see Figure 4-10) of plate perforations was taped and noise measurements were conducted. Then, the neighboring second row was taped and again noise measurements were obtained. After that, the noise spectrum of the perforated plate with the first three rows taped was obtained, and so on. The same procedure was applied by starting from the top row (9^{th} row in Figure 4-10) and taping rows downward.

The objective of these experiments is to assess the interaction of the perforated plates with the shear layer of the MIT acoustic chamber open jet and to investigate potential jet-jet shielding effect.

Here specifically, the goal was to identify how much of the perforated plate is affected by the shear layer of the MIT acoustic chamber open jet.

The results for the perforated plate with 40% porosity are only shown as the conclusions from the other plate measurements are the same. The 40% porous plate was taped first starting from the 9^{th} row (see Figure 4-11) and then starting from the 1^{st} (see Figure 4-12). Here the 9^{th} row is the spoiler row furthest from and the 1^{st} is the row closest to the horizontal plate in a spoiler configuration as shown in Figure 4-10.

Figure 4-11 suggests that by taping the top rows the noise due to the jetlets and their interaction (the two distinct peaks) increases compared to the case when all of the nine rows are open. Thus, the noise source region which is responsible for these peaks must be below the top five rows. The top rows essentially shield the noise

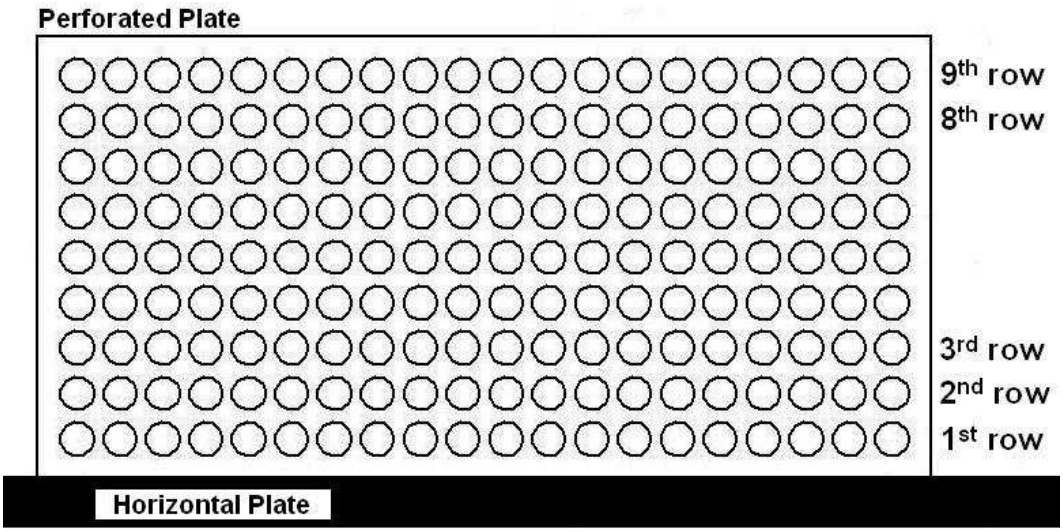

Figure 4-10: Schematic of the 40% perforated plate showing the row number in spoiler configuration.

generated within this noise source region.

Figure 4-12 further clarifies the situation. Once the 1^{st} and 2^{nd} rows are taped the distinct peaks disappear below the wind tunnel background noise. This suggests that the potential core of the open jet flows through the first couple of perforation rows. The shear layer interacts with the perforated plate through the top five rows, shielding the noise generated by the jetlets merging in the lower rows of perforations.

Using linear acoustic theory, the change in SPL that can be obtained by taping some of the rows, and leaving the other open (flowing) of a perforated drag plate can be assessed. The noise reduction relative to the case when no rows are taped, expected from k flowing rows, independent of mixing and shielding effects, is given by $10\log_{10}(9/k)$.

Table 4.2 shows the expected sound pressure level (SPL) reduction and effective porosity if a specified number of rows are taped compared to the case when no rows are taped. For example, if 4 rows are taped, then $9-4=5$ rows are flowing (open) and the noise reduction compared to the case when no rows are taped will be $10\log_{10}(9/5) = 2.55$ dB for a system of completely independent rows. The effective porosity of this plate will be 22% compared to 40% when no rows are taped.

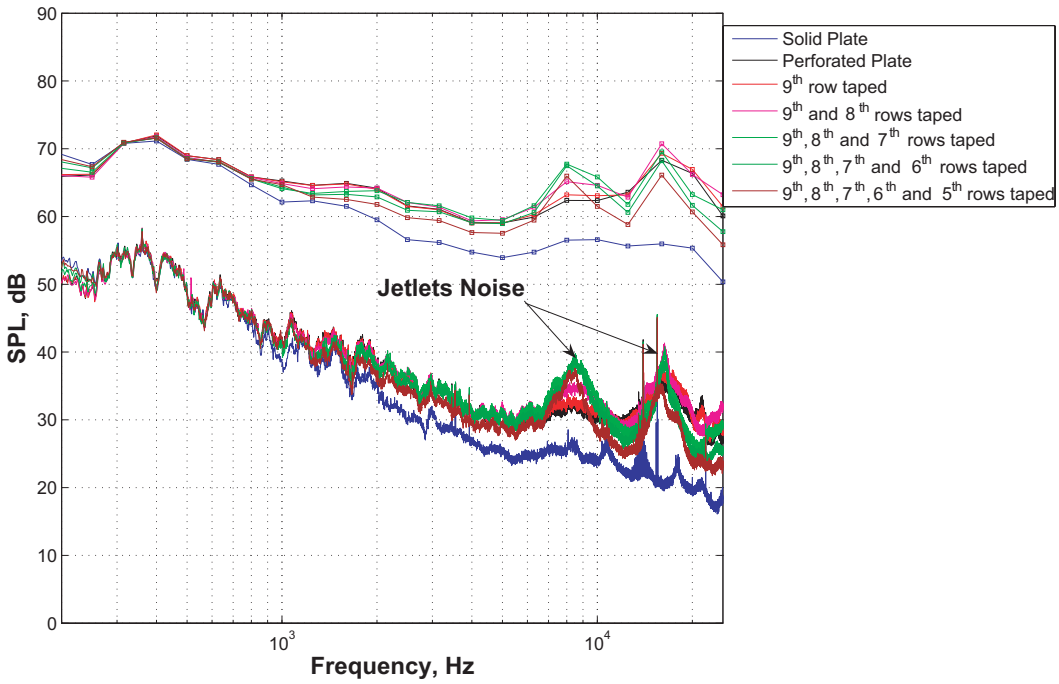

Figure 4-11: SPL spectra for a 40% perforated plate at 30 m/s, rows taped from the top.

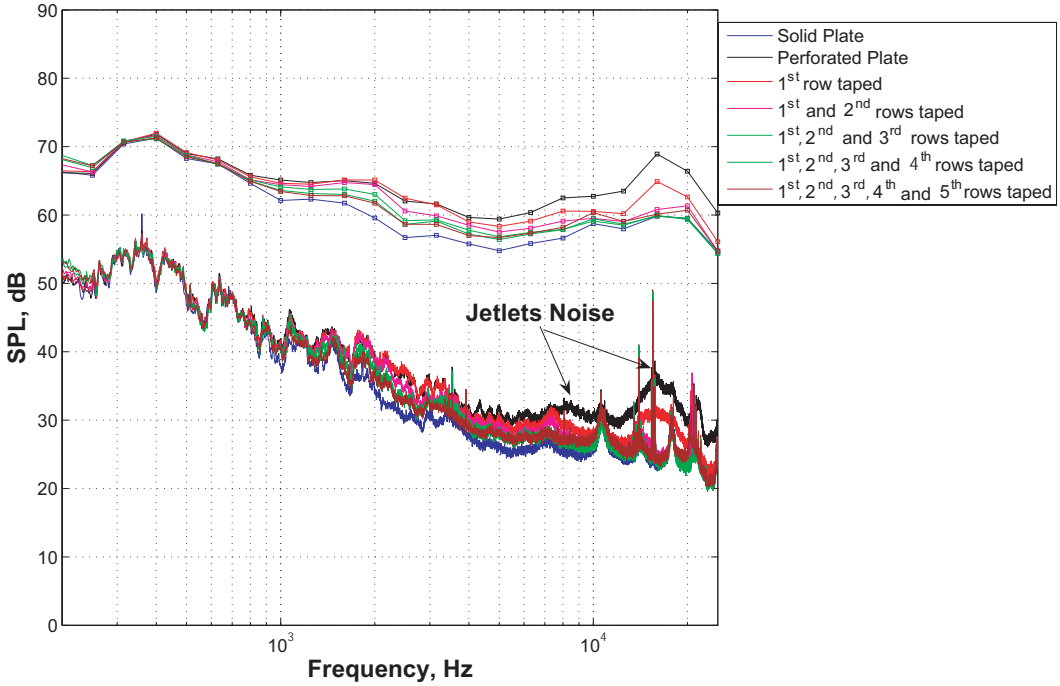

Figure 4-12: SPL spectra for a 40% perforated plate at 30 m/s, rows taped from below.

Table 4.2: Expected SPL reduction if a specified number of rows are taped compared to the case when no rows are taped for the 40% porous plate.

Number of Rows Taped	**ΔdB,** $10\log_{10}(9/k)$	**Effective Porosity**
1	0.51	36%
2	1.09	31%
3	1.76	27%
4	2.55	22%
5	3.52	18%

To more easily evaluate the effects of interaction of the open jet shear layer with the plate on the measured spectra, data for each spectrum of the 40% porous plate was normalized as follows. The appropriate value from Table 4.2 was added to each of the measured 1/3-octave-band spectrum levels, to correct the SPL levels for the number of flowing rows. Next, the spectrum levels measured for all nine rows flowing was subtracted from each of these spectra. The resulting SPL correction when k rows are flowing and $9-k$ are taped then becomes

$$SPL_{corr}(k) = SPL(k) + 10\log_{10}(9/k) - SPL(9). \tag{4.2}$$

Therefore, for a system of completely independent rows of jetlets this normalization would result in 0 dB spectra at all frequencies. For a given data point, net negative SPL spectral values represents frequencies for which merging of jetlets results in excess mixing noise. Net positive SPL values indicate frequencies for which shielding of jet noise by neighboring rows occurs. This helps to indicate plate regions where merging of jetlets results in excess mixing noise and regions where the shielding effects of the shear layer are dominant.

Figure 4-13 shows that when taping rows from the top, there is a large acoustic shielding effect for mid to high frequencies while at low frequencies, the noise signature is independent of the number of rows taped. The corrected SPL values at low to mid frequencies are the corresponding correction numbers in Table 4.2.

On the other hand, Figure 4-14 shows, that when taping rows starting from below, for mid to high frequencies jetlets interaction generates excessive noise. Here, again

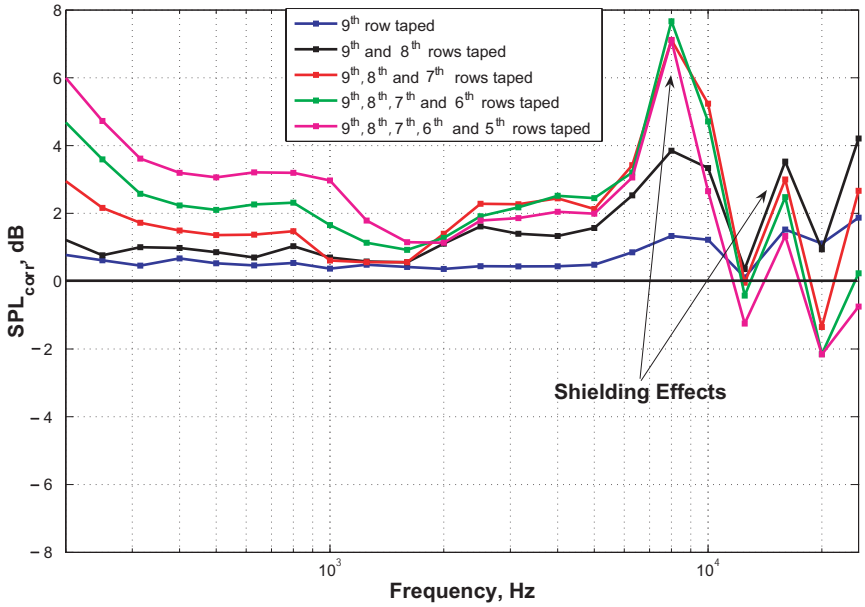

Figure 4-13: SPL normalized spectra for a 40% perforated plate at 30 m/s, rows taped from the top.

the corrected SPL values at low to mid frequencies are the corresponding correction numbers.

4.4 Summary

The important features of the perforated plate spectra can be summarized as follows. In the low frequency region $0 \leq f \leq 800$ Hz the noise signature due to the wind tunnel jet noise is obtained. The noise signature of the perforated drag plates are below the acoustic chamber background noise. This, combined with the fact that 540 Hz is the lowest usable far field frequency at all microphone locations, the noise spectrum of the perforated plate in the low frequency range could not be determined or measured directly.

The mid-frequency range ($800 \leq f \leq 2500$ Hz) is important to the full scale noise. It was hypothesized that this noise signature, which does not scale with St_d, is due to the isotropic turbulence structures of the jetlets and hence has no directivity. A semi-empirical noise prediction tool, described in Chapter 6, will be used to predict

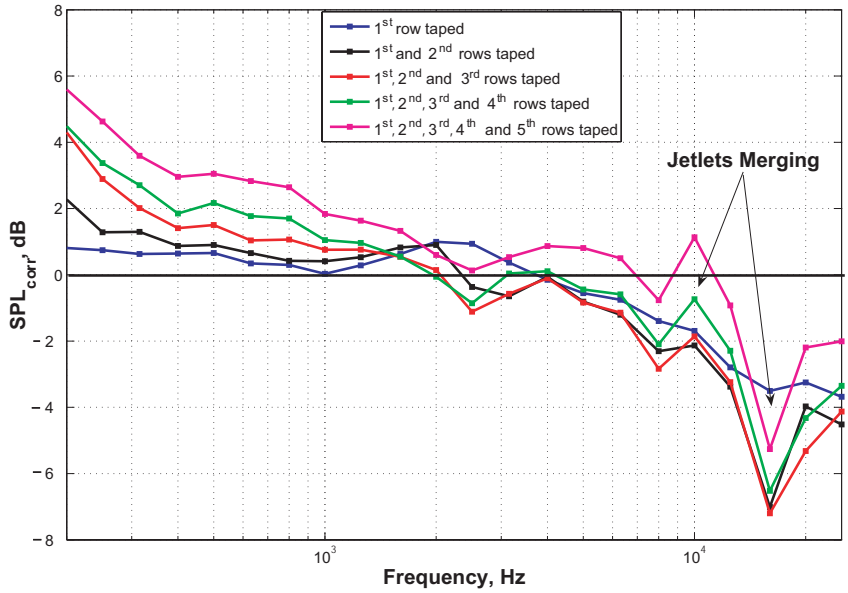

Figure 4-14: SPL normalized spectra for a 40% perforated plate at 30 m/s, rows taped from below.

the noise signature of the perforated plates in the mid-frequency range.

The high frequency region (2.5 kHz $\leq f$) scales with St_d. Two distinct peak frequencies are identified above 10 kHz for the full-scale configuration where the velocities are in the range of 60 to 100 m/s. In this, the assumption is made that the full scale perforated drag device has the same perforation diameter. This implies that the other length scale, the size of the plate L is not important for the peak frequencies when scaled to full size.

An assessment of the interaction of the MIT acoustic chamber open jet with the perforated plates was conducted. It was observed and concluded that the primary noise source responsible for the observed peaks in the high-frequency range is the merging of the jetlets. The shear layer interacts with the perforated plate through the top 5 rows, shielding the noise generated by the jetlets merging in the lower rows of perforations.

It was also found that there is a large acoustic shielding effect for mid to high frequencies while at low to mid frequencies, the shielding effect is negligible.

Chapter 5

Acoustic Phased Array Experiments

One of the main challenges in designing low-noise high-drag deployable devices is the lack of analytical models to predict the noise emitted by such designs. Such analytical models could simplify the design process of quieter drag devices, and the goal of the preliminary MIT tests and the experiments described here is to establish such a prediction capability.

Aeroacoustic tests of seven perforated drag plates in four different configurations (two spoiler configurations and two drag rudder configurations) were conducted in the closed jet Markham wind tunnel at Cambridge University. The Markham wind tunnel is equipped with a phased microphone array. The acoustic phased array provides a powerful measurement capability since it can identify noise 15 dB below the wind tunnel background noise [9]. This noise identification is done by processing only the sound that is correlated between pairs of array microphones. In comparison, the preliminary test campaign conducted in the MIT acoustic chamber was limited by the acoustic chamber characteristics such as size and background noise level.

This section focuses on the experimental aeroacoustic analysis of different perforated drag plates. The results, documented here, provide a valuable database for the design of perforated deployable drag devices.

5.1 Overview of the Acoustic Phased Array Experiments

As mentioned earlier, the idea behind a quiet spoiler/drag rudder is to alter the noise production mechanism by perforating the spoilers/drag rudders. It is hypothesized that, the large length scales responsible for the noise radiated by unsteady vortical structures can be changed to small length scales relevant in jet noise (jetlets due to the perforations).

Hypothesis

The hypothesis for these aeroacoustic experiments is that perforating the drag plates reduces low frequency noise and shifts the acoustic energy to high frequencies.

Objectives

The objectives of these experiments are to:

1. assess the acoustic benefits and impact on drag of a perforated spoiler/drag rudder,
2. identify the regions of such a perforated plate where bluff-body and turbulence mixing noise is generated,
3. assess different installation configurations of perforated drag devices for low noise,
4. determine the scaling laws of the noise spectra,
5. compare and assess the acoustic results with the results obtained from the preliminary tests conducted at MIT.

Success Goals

As mentioned earlier, the first success goal is to demonstrate a net benefit in the acoustic signature of perforated drag plates when compared to a solid plate generating the same amount of drag.

The second success goal is to show that low frequency noise is reduced and mid frequency generated turbulence mixing noise is shifted to high frequencies.

5.1.1 Acoustic Phased Array

The main challenge of aeroacoustic tests conducted in low-speed closed-loop wind tunnels is their enclosed reverberant environment. Wind tunnels, such as the Markham wind tunnel at Cambridge University, are designed primarily for aerodynamic tests and have high background noise levels. The solution to this problem is using a phased microphone array for acoustic measurements.

Although, acoustic phased array measurements require a substantial investment in time, money, and effort they provide information that cannot be provided in any other way. Phased arrays in closed wind tunnels usually consist of microphones flush-mounted in the wall of the test section. The wall boundary layer adjacent to the microphones creates a signal that is typically 10-20 dB higher than the acoustic radiation of the test article [9]. This interference can be removed by processing only the sound that is correlated between pairs of array microphones. Thus, phased acoustic arrays have improved signal-to-noise ratio and are good for source localization.

Sound pressure level data for the experiments described herein were acquired using an acoustic phased array mounted in the Markham wind tunnel at Cambridge University. To obtain high resolution at both low and high frequencies, two different arrays were used. The low frequency array has a frequency range of 500 to 5,000 Hz. The high frequency array is designed for a frequency range of 5,000 to 50,000 Hz. Both have a total of 90 microphones flush mounted in the wind tunnel floor [28].

The data acquisition system used has 48 channels. It consists of a signal conditioner and a data logger. The DAQ system has a maximum sample rate of 250 kHz

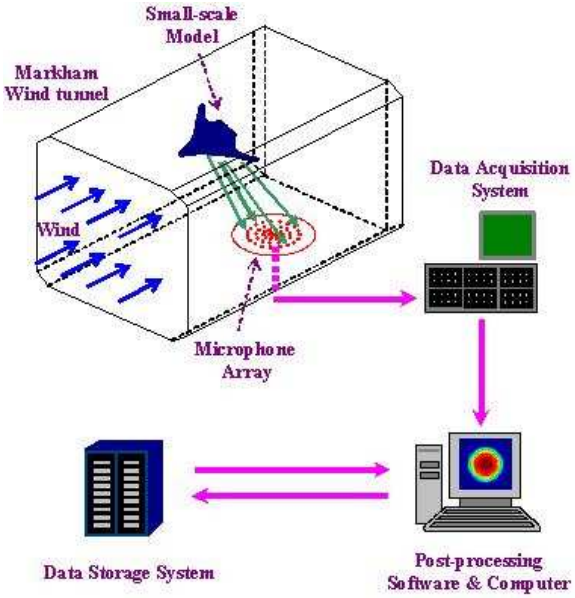

Figure 5-1: Markham array system (picture courtesy of Ho-Chul Shin).

per channel and 16-bit resolution. The data storage system has a 1.2 TB RAID [28]. Figure 5-1 shows a schematic of how the acoustic data is acquired from the acoustic array.

Both acoustic arrays were calibrated using a circular cylinder and a points source at a known position [28]. Two different calibration procedures were used to make sure that the array microphones and data acquisition system were working properly. The data from the array microphones were synchronously measured at a sampling frequency of 120 kHz and a measurement duration of 60 s.

5.1.2 Post Processing Techniques

The processing methods and computer programs used cannot be discussed in detail because of their proprietary nature. The Markham wind tunnel has a high background noise level due to the fan and the boundary layer development on the walls. It is a closed jet wind tunnel facility designed for low-speed aerodynamic tests, not for acoustics tests. However, thanks to the phased array and the post processing techniques used, noise sources below the wind tunnel background noise can be identified.

The procedure for the data analysis is as follows [28]. The time domain data is transformed into the frequency domain using a Fast Fourier Transform (FFT) for a pre-selected bandwidth. Then frequency-domain beamforming is used to successively focus the phased array to each point in a grid and thereby measure the apparent source strength distribution. This process, which is done off-line after the data has been digitally recorded, depends on a mathematical model for the acoustic propagation from each grid point to each microphone, and allows separation of source and background noise. The mathematical noise propagation model used here was of monopole type.

Beamforming algorithms are array process algorithms that focus or steer an array of grid points. The beamforming post processing used here, calculates the source strength at each grid point such that the difference between the measured signal and the simulated signal from the propagation model is minimal. The propagation model has an assumed monopole strength (to be found) and a certain direction of propagation with spherical loss depending on the microphone position and a scanning grid point. The most suitable source strength is found using a least-square method [28]. This is done on a frequency-by-frequency basis. After the data is processed, 1/3-octave band frequency image maps are obtained.

A number of special measures are taken in the beamforming process, used in this study. First the main diagonal in the cross power matrix (auto powers) is discarded to suppress the influence of tunnel background noise and more specifically high boundary layer noise. Second, the array scan plane is placed at a distance of 0.6 m between the array and the model reference grid to maximize the resolution, taking into account the Markham wind tunnel geometry [28].

For qualitative comparison of different plates, configurations and conditions, the array results are also processed to obtain narrowband spectra and again, the main diagonal in the cross power matrix is discarded. The acoustic data sampled at 120 kHz is processed using a block size of 4096, yielding a narrowband frequency resolution of 29 Hz. Five microphone pairs are used to obtain the narrowband cross spectra. The microphone pairs are chosen such that they are able to capture both the large and

small length scale structures, and the directivity pattern of the noise source.

The experimental data is monitored on-line by observing the time domain signal and SPL spectra in real time during the acquisition. The on-line monitoring is used to make sure that the array microphones and data acquisition system are working properly.

5.1.3 Design of Experiments

The design of acoustic phased array experiments needs careful planning. The main challenge is to choose the size of perforated drag plates such that their noise characteristics are above that of the wind tunnel background noise and within the desired frequency range.

To size the perforated plates tested in the Markham wind tunnel at Cambridge University, the data obtained from the MIT acoustic tests were used, after appropriate scaling.

The dimensional analysis on perforated drag plates in Section 2.2 revealed that for the simplified case of a square plate with a uniform perforation pattern the functional dependence of the sound pressure level is

$$SPL = f\left(\frac{s}{L}, St_L, Re_L, M, \frac{d}{L}, \psi, \theta, \frac{r}{L}\right), \tag{5.1}$$

where s is the perforation separation (Figure 2-3).

Both the SPL and frequencies are scaled based on the scaling factor, L/L_{MIT}. Here L is a candidate plate length (to be found) and L_{MIT} is the size of the perforated plates tested at MIT. The noise sources are assumed to be sufficiently incoherent that an increase in source area causes an equivalent increase in acoustic power or pressure square, i.e. area doubling caused power doubling [9]. Thus, for the sound pressure level scaling

$$SPL_L = SPL_{L_{MIT}} + 20\log_{10}\left(\frac{L}{L_{MIT}}\right), \tag{5.2}$$

where $L_{MIT} = 0.18$ m. The magnitude of SPL of the MIT acoustic chamber data is

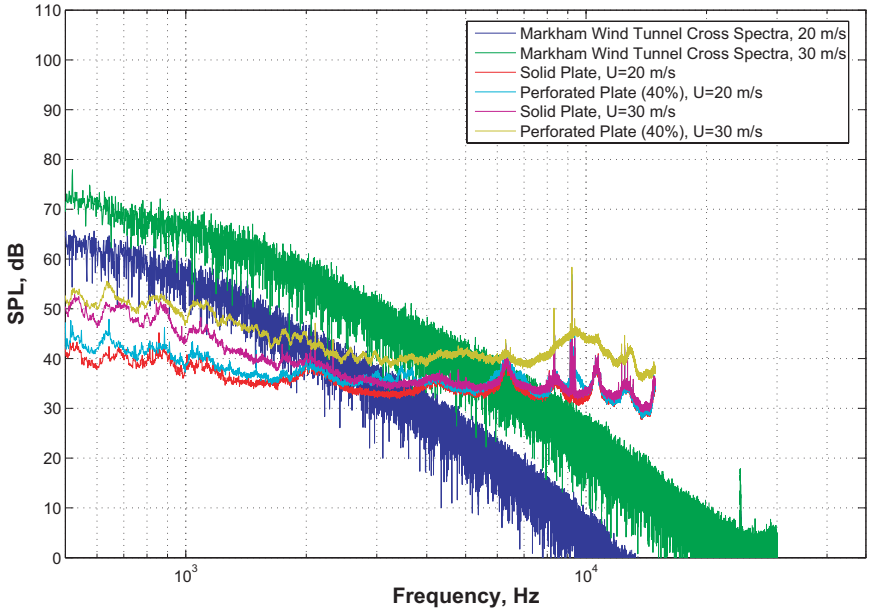

Figure 5-2: Markham wind tunnel background cross spectra vs 40% perforated plate spectra, scaled for L=0.3 m.

also corrected for microphone location.

Similarly, it is assumed, as suggested by Equation 5.1, that to first order the acoustic source wavelengths vary inversely with source dimension. Thus, the frequency of the MIT acoustic chamber data is corrected as follows:

$$f_L = f_{L_{MIT}} \left(\frac{L}{L_{MIT}} \right)^{-1}. \tag{5.3}$$

In order to find how the Markham test plates scale with characteristic lengths such as the length of the plate L, more than one plate size should be tested.

Figures 5-2, 5-3 and 5-4 show the Markham wind tunnel background noise spectra obtained from cross spectra of two microphones 0.04 m apart. These figures also show the corrected for size 40% perforated plate data obtained at the MIT acoustic chamber. The data on the three figures is for 20 and 30 m/s wind tunnel speed.

It can be seen that for plate lengths $L = 0.2$ m and $L = 0.1$ m most of the distinct features (the peaks discussed in Section 4.2) in the 40% porous plate spectra are above the Markham background noise and within the frequency range (500 - 50,000

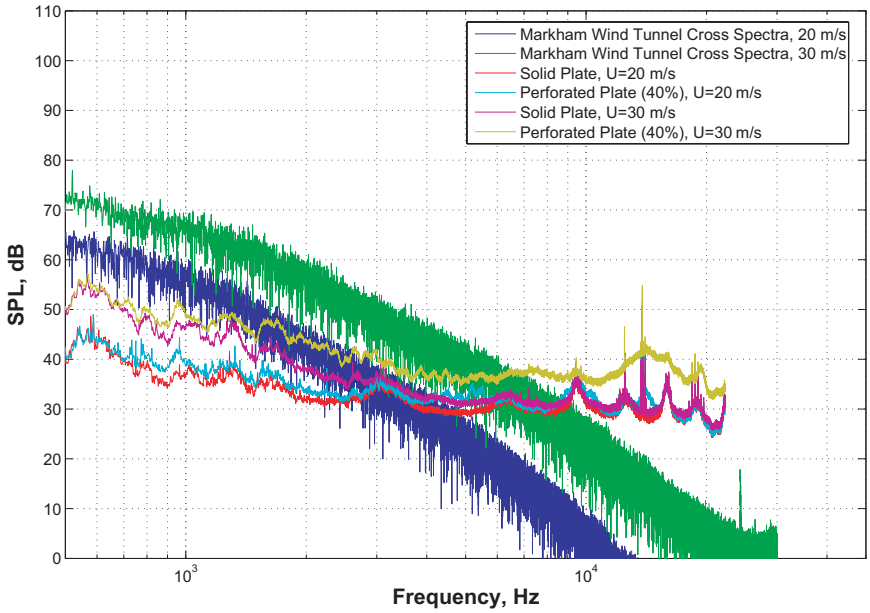

Figure 5-3: Markham wind tunnel background cross spectra vs 40% perforated plate spectra, scaled for L=0.2 m.

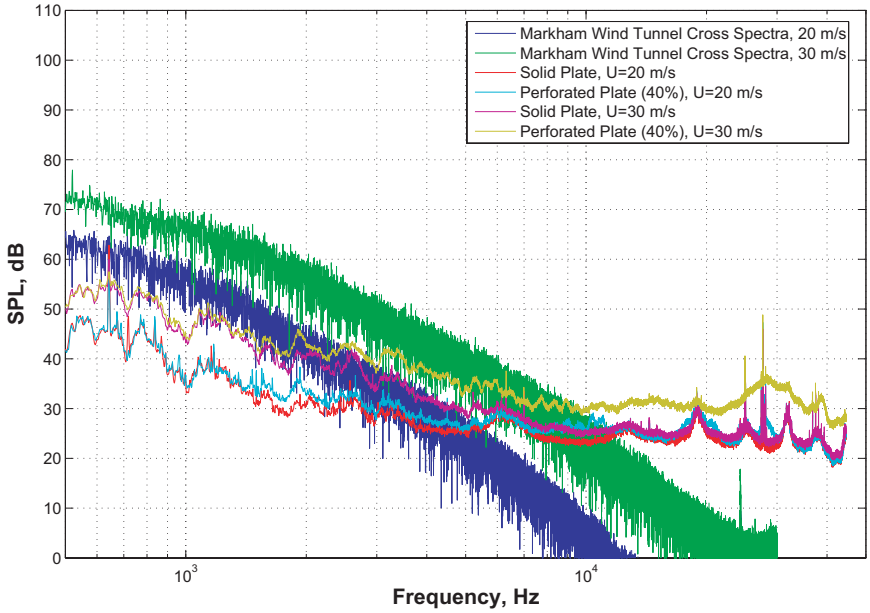

Figure 5-4: Markham wind tunnel background cross spectra vs 40% perforated plate spectra, scaled for L=0.1 m.

Hz) of the Markham wind tunnel acoustic arrays. For $L = 0.3$ m the frequency shift is not enough and some of the important features are below the Markham background spectra, while if $L < 0.1$ m the frequency shift to the right is too high and the plate spectra have much lower sound pressure levels. Thus, two plate sizes, $L_1 = 0.1$ m and $L_2 = 0.2$ m were chosen for the acoustic tests conducted in Markham wind tunnel at Cambridge University.

Once the candidate plate sizes were determined, the experiments were designed as follows. The non-dimensional geometric parameters which can be varied are s/L and d/L. To confine the design space, it is assumed that the peak frequencies will scale as Strouhal number, based on the ambient speed of sound, $St_a = fd/a = 0.19$ [6]. This Strouhal number is used to scale the peak frequencies of the spectra since it is suggested that the perforation diameter d is the relevant length scale. The desired frequency range for the peak frequencies is 4,500 - 50,000 Hz. 4,500 Hz is the lowest frequency for which the 40% porus plate spectra, scaled to L_2, are above the Markham background noise level (see Figure 5-3). The Markham acoustic array spectra above 50 kHz are contaminated by electronic noise. Thus, the minimum and maximum perforation diameters that will yield peak frequencies within this range are $d_{min} = 0.00129$ m and $d_{max} = 0.01436$ m. In order to be able to measure the acoustics of both plate sizes $L_1 = 0.1$ m and $L_2 = 0.2$ m at the same perforation diameter, $(d/L)_{min} = d_{min}/L_1 = 0.0129$ and $(d/L)_{max} = d_{max}/L_2 = 0.0718$.

For a uniform perforation pattern s/L takes only discrete values (see Section 2.2) and

$$\frac{s}{L} = \sqrt{\frac{1}{N}}, \tag{5.4}$$

where N is the number of the perforations in a perforated drag plate.

Figure 5-5 shows the parameter space of the plates tested in the Markham wind tunnel. The plates will be further referred to by their number indicated in Figure 5-5. The perforated drag plates tested at the MIT acoustic chamber are also shown. The six plates chosen for the Markham acoustic tests are such that the plate pairs 1 and 4, 5 and 6, and 2 and 3 have the same porosity. The porosity for a square plate

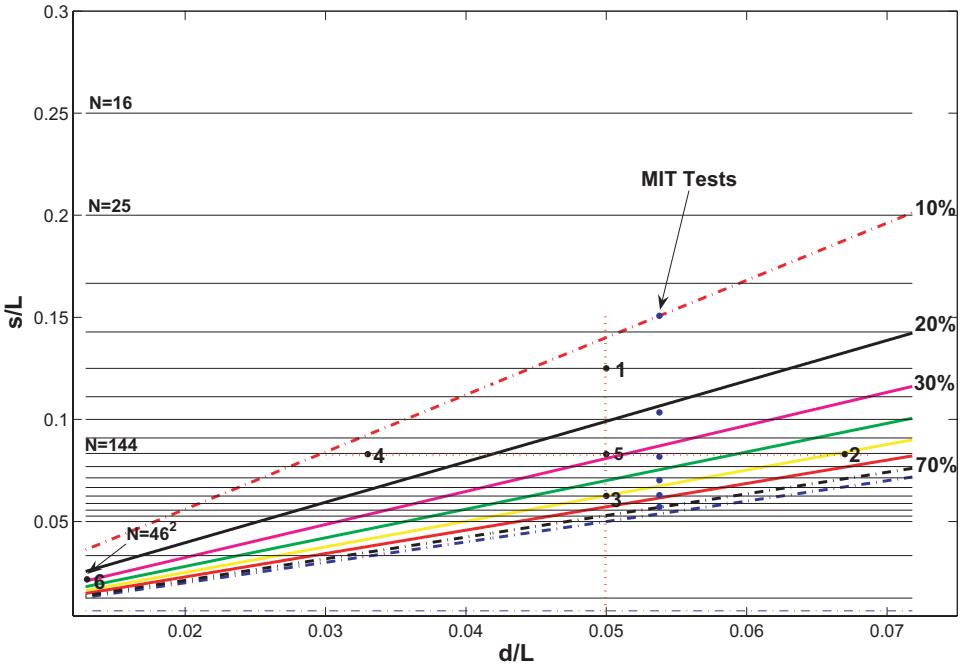

Figure 5-5: Parameter space used in experiments.

with a uniform perforation pattern is

$$\beta = \frac{\pi}{4}\left(\frac{d}{L}\right)^2\left(\frac{s}{L}\right)^{-2}, \tag{5.5}$$

and therefore constant porosity curves are represented by straight lines on Figure 5-5.

The perforated plates 1 to 5 are chosen such that they form a cross in the parameter space. This is convenient as noise characteristics of three plates at a time can be checked for variation with d/L or s/L, respectively while keeping the other non-dimensional group constant. Perforated plate 6 is chosen such that the lower left region on Figure 5-5 can be assessed for its noise reducing capabilities.

Finally, Table 5.1 shows the design characteristics of the perforated plates. N is the number of perforations. The plates were manufactured using a laser engraving machine at the MIT BioInstrumentation Laboratory. It was not only a very accurate means to fabricate the perforated plates but also an effective way; 52 plates with 17208 holes in total were manufactured within a couple of days. The material used was a 0.0045 m thick acrylic plate. In the fabrication process precautions were made

Table 5.1: Design characteristics of the perforated plates.

Plate	N	d/L	s/L	Porosity
Perforated Plate 1	64	0.050	0.1250	0.1257
Perforated Plate 2	144	0.067	0.0830	0.5118
Perforated Plate 3	256	0.050	0.0625	0.5027
Perforated Plate 4	144	0.033	0.0830	0.1242
Perforated Plate 5	144	0.050	0.0830	0.2850
Perforated Plate 6	2116	0.013	0.0217	0.2819

to relieve the acrylic plates from deforming due to the heat dissipated during laser cutting.

5.1.4 Test Setup

Four different perforated drag plate installation configurations were tested. Two of them are spoiler configurations, as shown in Figures 5-6 and 5-8, and the other two are drag rudder configurations, as depicted in Figures 5-10 and 5-12.

The 1.535 m by 1.0 m by 0.006 m horizontal plate made of aluminum holds the perforated plates and was supported by two endplates. The endplates, secured through two side blocks to the Markham wind tunnel rails, had holes drilled such that the vertical position of the horizontal plate could be changed. The side blocks could be translated along the wind tunnel rails such that the horizontal plate was also able to be shifted axially. The horizontal plate was at 0° angle of attack. The position of the horizontal plate was changed such that the perforated plate reference scanning grid was always at 0.6 m from the acoustic array center.

Figure 5-6 shows the spoiler test configuration 1. The perforated drag plates in this configuration were mounted on the bottom side of the horizontal plate through two L-brackets. The perforated plates were located exactly above the phased array center. The reference grid for this setup was a square area $3L$ by $3L$ with a grid centered at the geometric center of the perforated plates (see Figure 5-7). Here L is the length of the tested perforated plate.

Figure 5-8 shows the spoiler test configuration 2. The horizontal plate trailing edge was located exactly above the center of the phased array. The reference grid

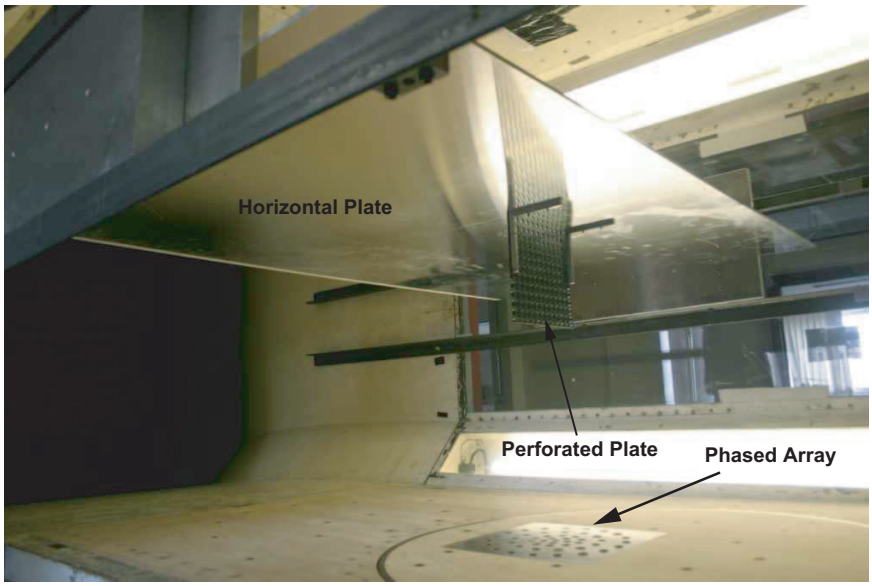

Figure 5-6: Spoiler test configuration 1. The wind tunnel free stream is from left to right.

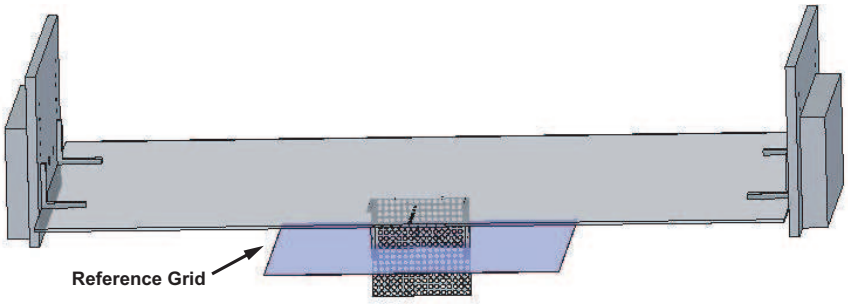

Figure 5-7: Phased array reference grid for spoiler test configuration 1.

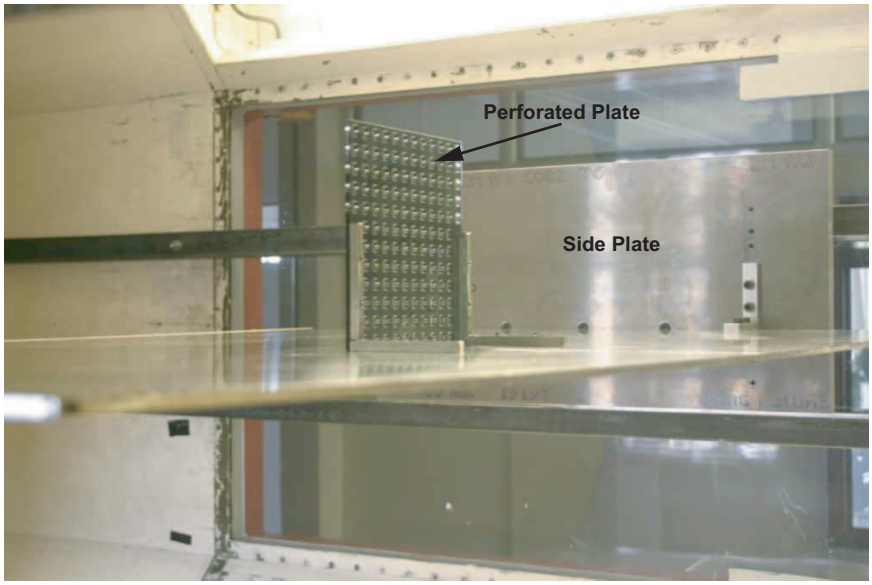

Figure 5-8: Spoiler test configuration 2. The wind tunnel free stream is from left to right.

for this setup was also a square $3L$ by $3L$ grid at a distance of $0.5L$ from the top surface of the horizontal plate (see Figure 5-9). Again, L is the length of the tested perforated plate.

Figure 5-10 shows the drag rudder test configuration 1. The perforated drag plates were mounted on the horizontal plate trailing edge and were above the center of the phased array. The square reference grid for this setup was $3L$ by $3L$ and is shown in Figure 5-11.

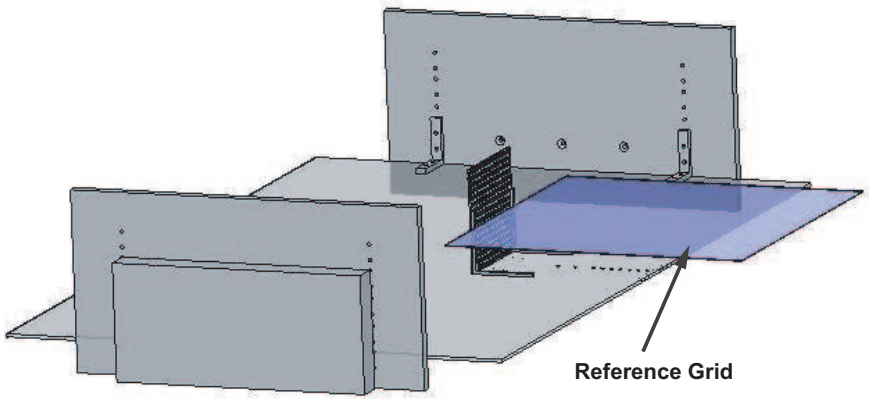

Figure 5-9: Phased array reference grid for spoiler configuration 2.

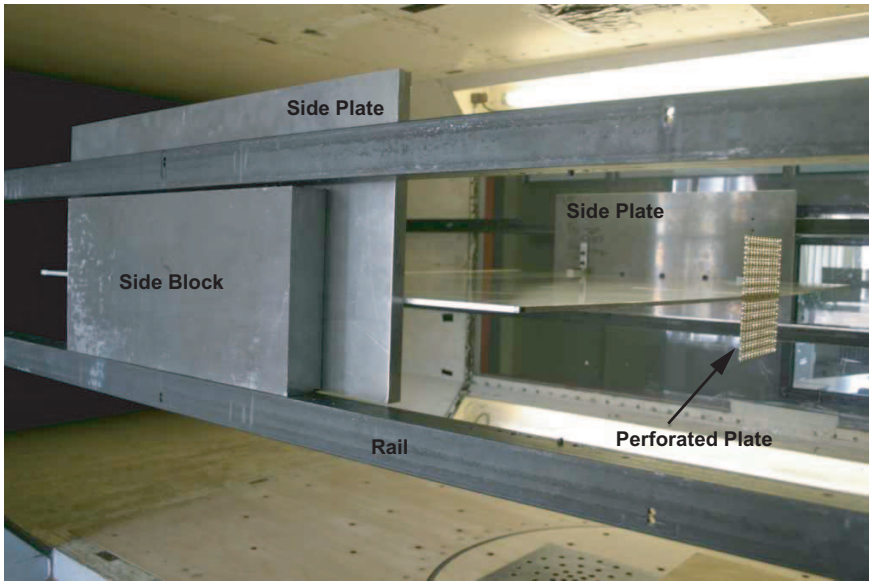

Figure 5-10: Drag rudder test configuration 1. The wind tunnel free stream is from left to right.

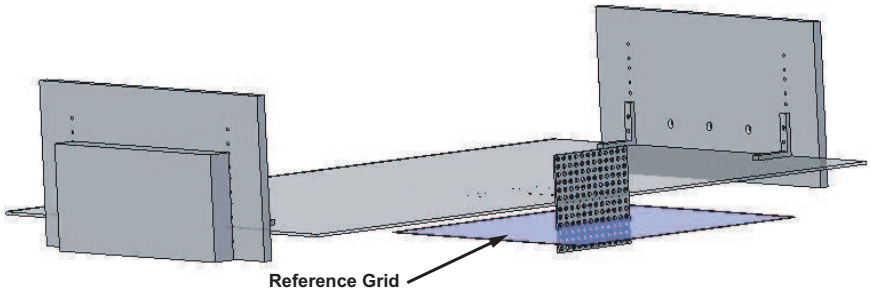

Figure 5-11: Phased array reference grid for drag rudder test configuration 1.

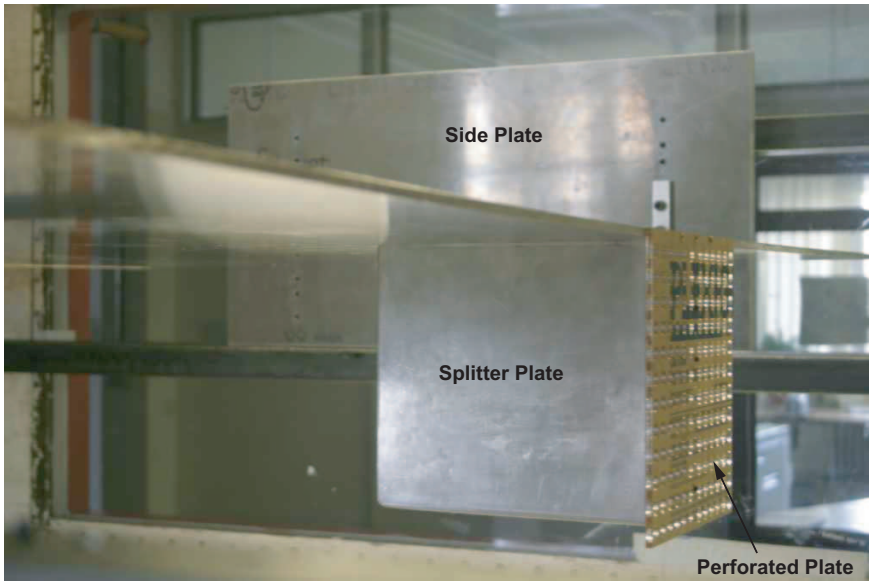

Figure 5-12: Drag rudder test configuration 2. The wind tunnel free stream is from left to right.

Figure 5-12 shows the drag rudder test configuration 2. The perforated drag plate positioned above the phased array center, was mounted on the horizontal plate trailing edge. It was also secured to a winglet type splitter plate. The edges of the winglet splitter plates were rounded to reduce noise scattering effects. The reference grid for this setup ($3L$ by $3L$) is shown in Figure 5-13.

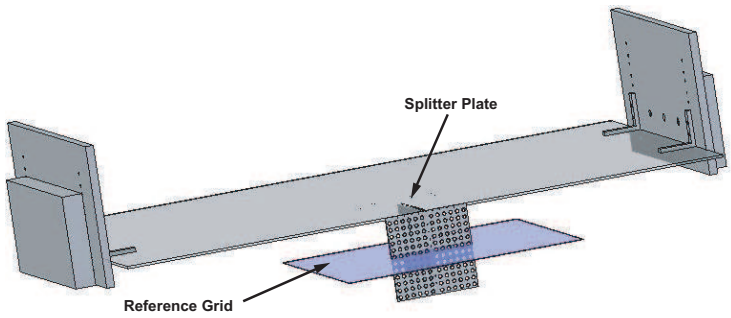

Figure 5-13: Phased array reference grid for drag rudder test configuration 2.

5.1.5 Boundary Layer Matching

It is important to match the boundary layers between the model and the full-scale test articles such that the model data does accurately represent the physical phenomena when scaled to full size. This section presents the considerations made to match the boundary layer thickness ratio $\delta(x_s)/L$ between full size and model size. Here $\delta(x_s)$ is the boundary-layer thickness at the spoiler location x_s measured from the leading edge. L is the spoiler height.

The flow immediately upstream of the leading edge of a flat plate is uniform at the free stream location. Downstream of the leading edge, the influence of friction will begin to retard the flow adjacent to the surface, and the extent of this retarded flow will grow higher above the flat plate as it moves downstream.

The flow just downstream of the leading edge is laminar. However, after a certain distance, instabilities will occur; these instabilities in the laminar flow will rapidly grow causing transition to turbulent flow. This transition takes place over a finite region. For purpose of analysis the transition region is modeled as a single point, referred to as the transition point, upstream of which the flow is laminar and downstream of which the flow is turbulent. The boundary layer on an airfoil usually changes from laminar to turbulent at $Re_x = 10^6$.

For an aircraft such as a Boeing 747 at an approaching speed of 79 m/s the critical Reynolds number and the subsequent boundary layer transition occur at only 0.19 m from the leading edge (1.73% of the wing chord), such that the boundary layer is turbulent over most parts of the wing. Also, the spoiler projection of a Boeing 747 is $L/c_{ws} = 10\%$, where L is the height of the spoiler and c_{ws} is the wing chord at the spoiler location.

The length of the horizontal flat plate is small and the boundary-layer is laminar across the entire plate. On a full sized aircraft the boundary layer turns turbulent very close to the leading edge. This can affect the noise emitted by the perforated drag plates. Drag will also be affected: the momentum of the fluid elements close to the surface is larger in a turbulent flow, such that a turbulent flow is less likely to

separate from body surface. It is important that the experimental horizontal plate has similar boundary layer such that the results are valid for a full sized wing.

The leading edges of the horizontal plate were rounded to reduce noise scattering effects. The boundary layer was tripped using three layers of tape cut in sawtooth form over the entire span at 0.05 m from the leading edge on the suction and pressure sides of the horizontal plate. The width of the tape was 0.015 m. The strip thickness was 0.0005 m. A stethoscope was employed to verify whether or not the trips induced the desired boundary layer transition. The stethoscope was attached to an L-shaped total pressure tube, which was traversed manually over the surface of the horizontal plate. Transition from a turbulent boundary layer was observed by listening.

For incompressible flow over a flat plate, the turbulent boundary-layer thickness is given by

$$\delta(x) = \frac{0.37x}{\sqrt[5]{Re_x}}. \tag{5.6}$$

Thus, $\delta \propto x^{4/5}$ and turbulent boundary layer thickness grows more rapidly with distance along the surface as compared to $\delta \propto x^{1/2}$ for laminar flow. This simplified, empirically based result is used to match the boundary layers between full scale and model scale. The boundary layer thickness at the spoiler location, $\delta(x_s) \propto x_s^{4/5}$ is different for the model and full size spoiler. To match the characteristics of the flow at the spoiler location, $\delta(x_s)/L$ should be the same.

If spoilers are installed on the current Silent Aircraft eXperimental SAX10 design, it is suggested that they be mounted at the rear spar location on the wings. For the outer wing sections, the spar is located at 67% of the local wing chord [5].

Based on the boundary layer thickness calculations for SAX10 [5], it was found that the chord of the horizontal plate should be at least 4.5 m to match the full size $\delta(x_s)/L$.

Thus, it was decided that exact boundary layer matching was not possible. The horizontal plate chord of 1 m was chosen such that the spoiler projection of the small plates ($L_1 = 0.1$ m) is 10% and the same for both model and full size spoiler. Thus, the projection of the small perforated plates ($L_1 = 0.1$ m) is 10%, while the projection

of the large ($L_2 = 0.2$ m) perforated plates is 20%.

5.1.6 Test Campaign

Three different free stream velocities were tested: 20, 30 and 40 m/s. The maximum speed of the tests was constrained by the Markham wind tunnel performance specifications and increased background noise levels at high speeds. The purpose of testing at three different velocities is to determine the noise magnitude and frequency variation of the sound spectra with airspeed and then to scale them up to the approach velocity of the candidate Silent Aircraft design SAX10.

Four different test setups were tested: two spoiler and two drag rudder test configurations. The objective is to assess the different installation configurations and then to choose the most beneficial one for noise reduction which is envisioned to be incorporated in the design of the Silent Aircraft.

For each test configuration one solid pair and six perforated pairs of plates were tested. Each of the seven pairs of plates consists of a small ($L_1 = 0.1$ m) and a large ($L_2 = 0.2$ m) plate. On the other hand, each of the six perforated plate pairs correspond to a different point in the parameter space (1 to 6) in Figure 5-5, i.e. the plates within the pair have the same s/L and d/L. The purpose of testing two different sizes is to be able to asses how the noise characteristics (SPL and frequency) scale with plate size.

The location of the horizontal plate was changed such that the reference grid for each test configuration was always at 0.6 m from the center of the acoustic array.

Acoustic tests of the horizontal plate alone for each configuration were conducted before mounting the test plates. Tests with horizontal plate only were used as a benchmark to identify the noise spectral features due to the perforated plates only.

Once the test data was acquired, it was post processed with the techniques discussed in Section 5.1.2. Image source maps in 1/3-octave band frequency were obtained for each test case.

For qualitative comparison of different plates, configurations and conditions, the array results were processed to obtain narrowband spectra. The experimental results

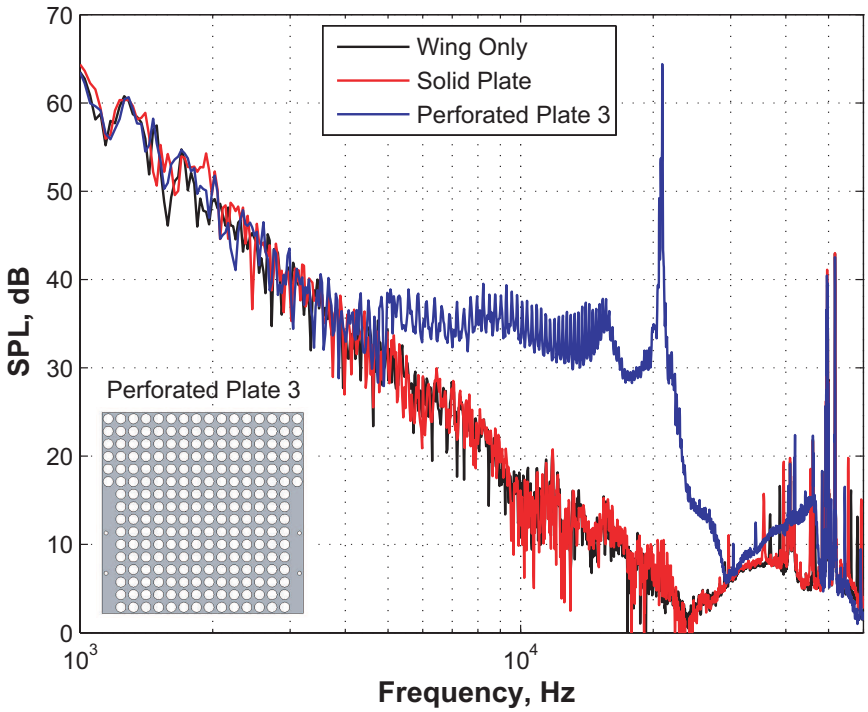

Figure 5-14: Noise cross spectra of small ($L = 0.1$ m) perforated plate 3 at 30 m/s in spoiler configuration 1.

of the aeroacoustic test campaign are discussed next.

5.2 Discussion of Experimental Results

A sample spectrum of the acoustic phased array tests is shown in Figure 5-14. Perforated plate number 3 has $d/L = 0.050$, $s/L = 0.0625$ and a porosity $\beta = 50.27\%$. Similar to the test at MIT, distinct peaks at high frequency are observed. Thus, small length structures are characteristics of the noise generation mechanism associated with the perforated plate.

As mentioned before, the narrowband acoustic data ($\Delta f = 29$ Hz) was obtained from the cross spectra of five microphone pairs. The microphone pairs were chosen such that some of the pairs capture correctly the large length scale structures and others the small length scale structure. The data analysis described in this Section, was confined to only one microphone pair that was considered to correctly capture

the small length scale structures, responsible for the high frequency distinct peaks. The spectra for each of the plates, configurations and free stream velocities from this microphone pair are shown in Appendix B.

As expected, the solid plate exhibits no distinct peaks in the high frequency region. Distinct noise features, such as bluff-body vortex shedding of the solid plates ($\beta = 0$) are at frequencies lower than 500 Hz which is the lowest frequency the acoustic phased array can detect correctly. The Markham wind tunnel also has high levels of background noise at low frequency (SPL of 80 dB at 100 Hz). Thus, the solid plate was not included in the analysis that follows because the spectra are almost identical with the wind tunnel background noise. To obtain the low frequency content hot wire tests are planned in future.

One of the most interesting observations of the test campaign is the presence of intense, narrowband tones in the noise spectra for various plates at different operating conditions (see Figures 5-15 and 5-16). After carefully assessing the acquired data it is found the tones are observed for small plates ($L_1 = 0.1$ m) at $f_T = 19 \div 21$ kHz and for large plates ($L_2 = 0.2$ m) at $f_T = 12.5 \div 18$ kHz. When observed for a specific perforated plate the frequency of the tone does not change with free stream velocity but plate size only.

Figures 5-15 and 5-16 show the noise cross spectra for small ($L = 0.1$ m) perforated plate 5 ($d/L = 0.050$, $s/L = 0.083$ and $\beta = 28.50\%$) at $U_\infty = 30$ m/s and $U_\infty = 40$ m/s in spoiler configuration 1. As mentioned before, the acoustic test data was post-processed and 1/3-octave band frequency image maps were obtained. The source maps at the 1/3-octave band center frequency nearest to the peak frequency of the tones are also shown in Figures 5-15 and 5-16. The direction of the flow and the plate position are shown on the source maps.

As can be seen from the source maps, their strongest noise producing regions are the edges of the perforated plates. The maximum strength of the source regions at the tone peak frequencies is at least 15 dB above the other source maps maximum SPL. Thus, the dynamic disturbances of the flow near the plate edges are suggested to be the main cause of these tones.

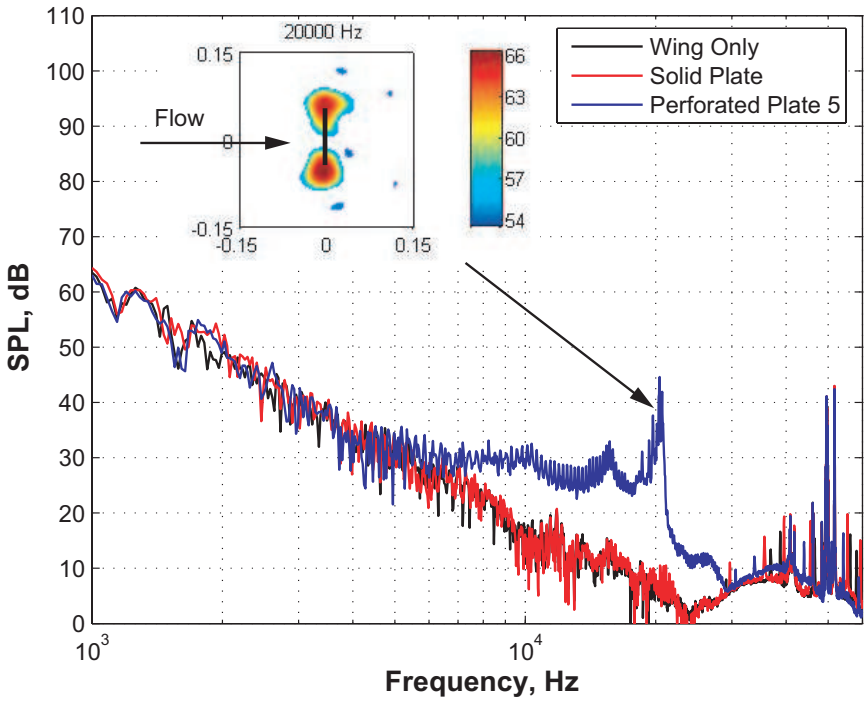

Figure 5-15: Noise cross spectra of small ($L = 0.1$ m) perforated plate 5 at $U_\infty = 30$ m/s in spoiler configuration 1.

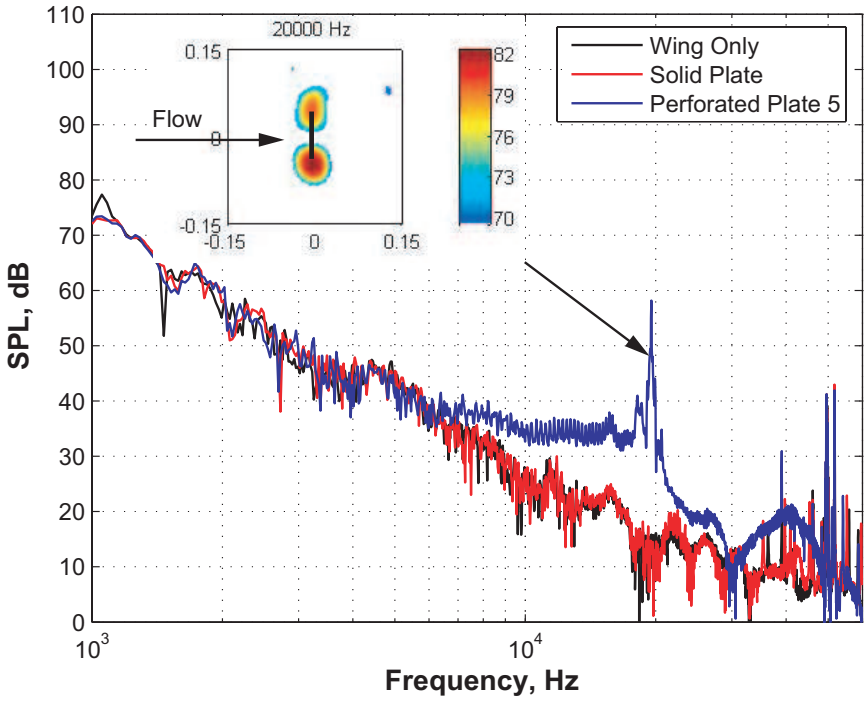

Figure 5-16: Noise cross spectra of small ($L = 0.1$ m) perforated plate 5 at $U_\infty = 40$ m/s in spoiler configuration 1.

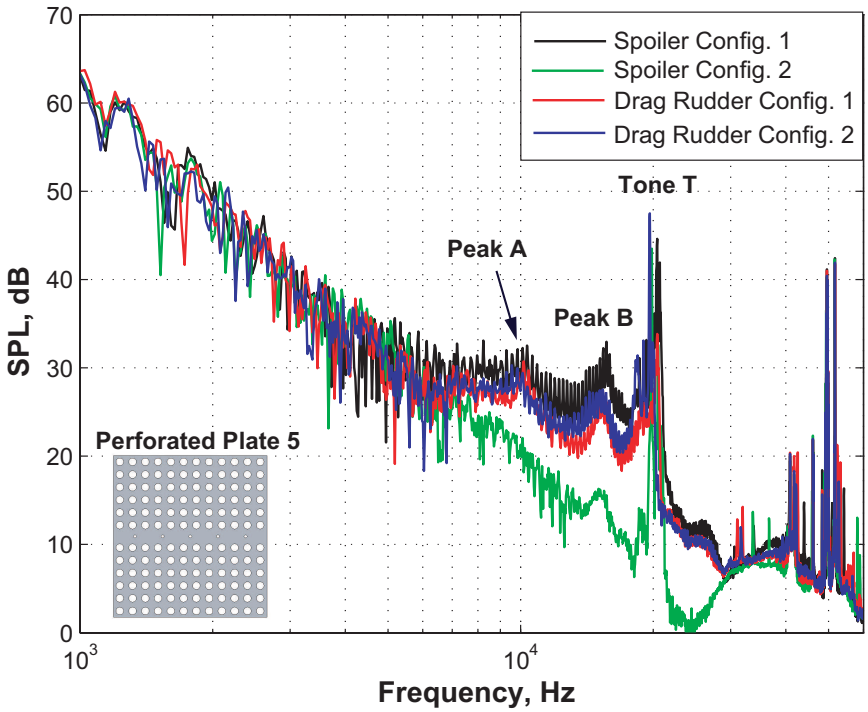

Figure 5-17: Noise cross spectra of small ($L = 0.1$ m) perforated plate 5 at $U_\infty = 30$ m/s for the four configurations.

Figure 5-17 shows the noise cross spectra for perforated plate 5 at $U_\infty = 30$ m/s for the four different test configurations.

The tone marked by **T** is present in all of four spectra. A similar situation is observed for perforated plates 1, 2, 3 and 4. Therefore, this tone is considered to be independent of the installation configuration. Plate 6 is the only plate for which no distinct tone was observed in the spectrum. Perforated plate 6 also has the smallest $(s-d)/2$, which is the distance between the plate edge and perforations (see Figure 5-20). Such tones sometimes result from blunt edge vortex shedding. Here the thickness of the plate could play a major role together with $(s-d)/2$. The full investigation of the true nature of the observed tones is left for future work.

One of the objectives of these acoustic phased array tests is to find the scaling laws for the perforated plate noise spectra. These scaling laws are envisioned to be used in a prediction model for the acoustic signature of the full size drag devices.

In order to find the magnitude and frequency scaling laws it is convenient to first

define the distinct features in the noise spectra by their sound pressure level and frequency, and then to analyze the data analytically.

For each spectrum the distinct peaks were identified and then labeled, starting at **A**, and then **B**, **C**, **D** and **T**, which denotes the discussed tone. Figure 5-17 shows peaks **A** and **B**, and a tone **T** identified in the spectra of perforated plate 5. Figure 5-17 also shows that the peaks which are present in the spectra of spoiler test configuration 1 are also present in the other three configurations, although of different magnitude in SPL. This was the case for all perforated plates. Therefore, also due to time constraints, the scaling analysis presented next was confined only to the spoiler installation configuration 1. This test configuration also resembles the spoiler setup in the MIT acoustic chamber and allows a direct comparison.

The magnitudes and frequencies of the identified peaks (**A**, **B**, **C**, **D**, and **T**) are stored in MATLAB® using two five dimensional arrays. The first dimension of the arrays corresponds to the different test configurations tested. The second dimension corresponds to the free stream velocity. The third dimension corresponds to the plate size $L_1 = 0.1$ m and $L_2 = 0.2$ m. The fourth dimension of the array corresponds to the five peaks **A**, **B**, **C**, **D** and **T**. The fifth dimension corresponds to the different perforated drag plates. There is one array in which the peak frequencies are defined and another array that captured the magnitude of the peaks. When a peak is not well defined a value of zero is entered in the array for the frequency and the magnitude. This is done such that an analytical investigation is possible.

Tables A.1 and A.2 tabulate the distinct peak frequencies and magnitudes, respectively, for the small plates ($L_1 = 0.1$ m) in spoiler configuration 1.

On the other hand, Tables A.3 and A.4 show the distinct peak frequencies and magnitudes, respectively, for the large plates ($L_2 = 0.2$ m) in spoiler configuration 1.

The present analysis is confined to the first two spectral peaks observed, **A** and **B**, which are always easily identifiable. The objective is to get some physical insight on what might be the root cause for the observed peaks. The approach is first to define the possible velocity and length scales important for a perforated plate and then to try to collapse the peak frequencies on a Strouhal number basis.

To search for the scaling in the peak frequencies a Strouhal number is defined according to $St_{LS} = fLS/VS$, where LS and VS are candidate length and velocity scales, respectively. Sections 5.2.1 and 5.2.2 first define the candidate velocity and length scales and then a possible scaling law is investigated by plotting f/VS and St_{LS} as a function of the non-dimensional parameters defined in Equation 5.1. Important non-dimensional parameters, describing a perforated plate are d/L, s/L, $(s-d)/L$ and the porosity β.

5.2.1 Velocity Scaling

The most obvious velocity scale to be used for scaling of the peak frequencies is the free stream velocity U_∞. Other velocity scales, such as the mean velocity at the entrance of each perforation, were also considered but the results for $VS_1 = U_\infty$ are presented here only.

In order to find if there indeed exists a velocity scaling of the peak frequencies, f/U_∞ is plotted as a function of d/L, s/L, $(s-d)/L$, β, s, d and L. The analysis shows that peak f/U_∞ value collapses on plate by plate basis for plates with the same lengths.

Figures 5-18(a) and 5-18(b) show f/U_∞ of the peak **A** plotted separately for small and large pates on a plate by plate basis. The peak frequencies were determined by inspection of the perforated plate spectra and an error bar of 10% was assumed to account for this. It can be seen that the peak f/U_∞ values collapse within the error bars.

The same was observed in the analysis of the peak **B** as shown in Figures 5-18(c) and 5-18(d). Therefore, it is conjectured that the peak frequencies of **A** and **B** scale with the free stream velocity.

It is important to point out that the peak frequencies observed in the spectra of the perforated plates tested in the MIT acoustic chamber also scaled with the free stream velocity (Section 4.2.4).

Figure 5-18(c) and Table A.1 show that only for the small perforated plate 4 a distinct peak **B** was only observed at free stream velocity of 20 m/s. It is hypothesized

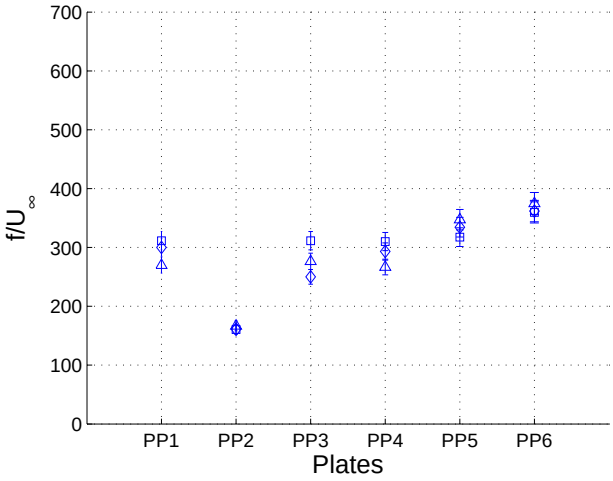

(a) Peak **A** for small plates ($L_1 = 0.1$ m).

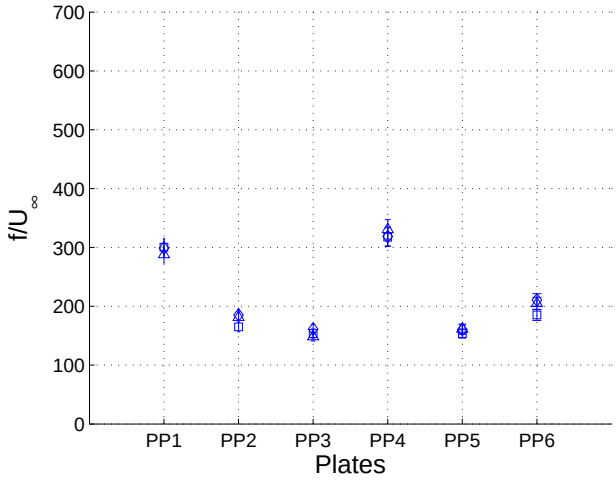

(b) Peak **A** for large plates ($L_2 = 0.2$ m).

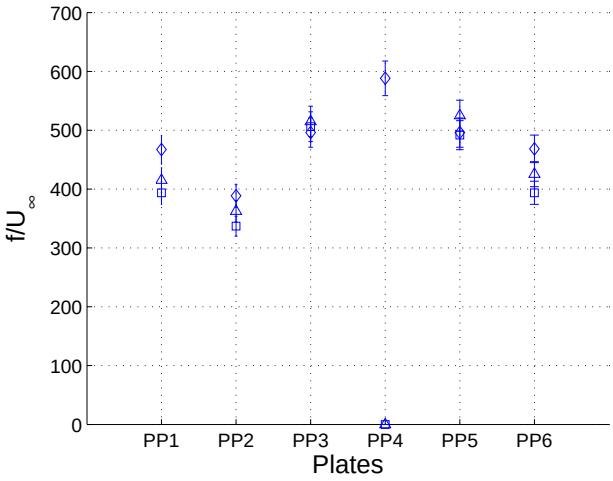

(c) Peak **B** for small plates ($L_1 = 0.1$ m).

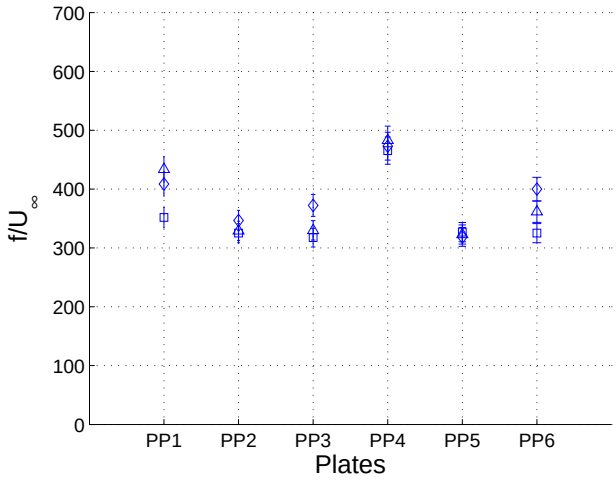

(d) Peak **B** for large plates ($L_2 = 0.2$ m).

Figure 5-18: Velocity scaling of the peak frequencies.
'◇' 20 m/s; '△' 30 m/s; '□' 40 m/s.

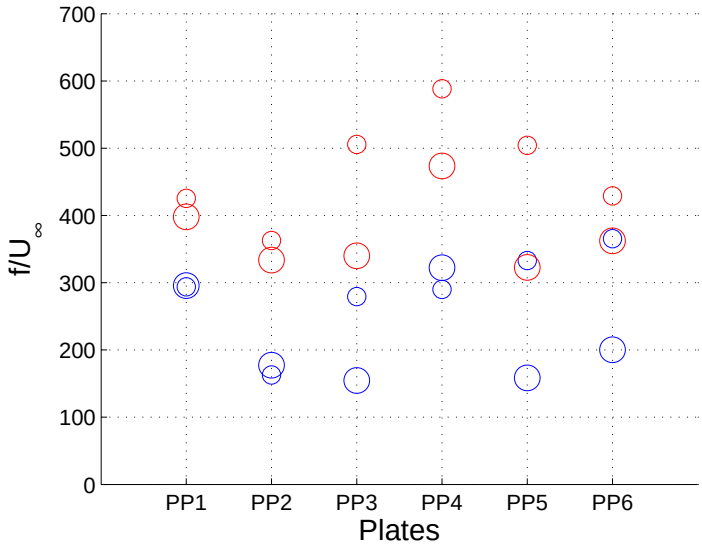

Figure 5-19: Average velocity scaling of the peak frequencies.
'○' Peak **A** for small plates; '◯' Peak **A** for large plates; '○' Peak **B** for small plates; '◯' Peak **B** for large plates.

that peaks **B** exist also for 30 m/s and 40 m/s but are not well defined. Thus, for later analytical analysis it is assumed that these peaks **B** also exist at 30 m/s and 40 m/s, and the peak **B** value of f/U_∞ at 30 m/s and 40 m/s is assumed the same as the value of f/U_∞ at 20 m/s. This is done in order to facilitate the process of searching for a possible length scale presented next.

In what follows, candidate length scales LS are obtained first. The Strouhal number $St_{LS} = fLS/U_\infty$ is then plotted as a function of d/L, s/L, $(s-d)/L$ and β. It is observed that the peak f/U_∞ values are within the error bars for a perforated plate with specific size. In order to make the visualization easier an average of the these peak specific f/U_∞ value is determined for each plate and size. Figure 5-19 shows the average values used in the search for a length scale.

5.2.2 Length Scaling

As shown above, the frequency scales with the free stream velocity. To get a better physical insight on what might be the generation mechanism behind the observed peaks, possible length scales are investigated first.

Candidate Length Scales

The length scales considered to be important for the peak frequency scaling are as follows:

1. $(s-d)$ - the width of the strip between two consecutive perforations (see Figure 5-20). Similarly, length scale $(s-d)/2$ can also be considered. This is the distance between the plate edge and the nearest perforation (Figure 5-20). Thus, the first length scale which was considered in this study is $LS_1 = (s-d)$.

2. d - the diameter of the perforations. It is an important length scale since the peaks might be due to the jetlets formed at the exit of each perforation. Therefore, $LS_2 = d$.

3. s - the separation between two neighboring perforations. The peaks might be due to jet-to-jet interaction and the spacing could play a major role in the peak frequencies; $LS_3 = s$.

4. L - the size of the tested square plates. Perforated plates and screens are used to dampen the turbulence levels in wind tunnels. The length or size of the plate together with the perforations determine the flow regime and level of turbulence behind the plate. Thus, the fourth length scale under consideration is $LS_4 = L$.

For each of the candidate length scales the Strouhal number $St_{LS} = fLS/U_\infty$ is plotted as a function of d/L, s/L, $(s-d)/L$ and β. The plots are given in Appendix C. The analysis shows that among the length scales considered none was found to collapse the data on a Strouhal number basis.

For simplicity only Figure 5.2.2 is discussed here. The figure shows $St_L = fL/U_\infty$ as a function of porosity β. It is interesting to point out that the peak **A** values in St_L for plates 2, 3, 5, and 6 are within the interval [30, 40]. The corresponding values for plates 1 and 4 are scattered between 30 and 95. The peak **B** values do not seem to have the same relationship. It is believed that both peaks must be due to the

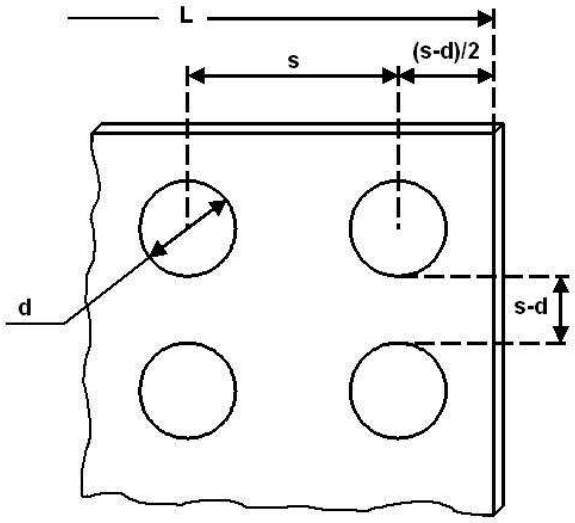

Figure 5-20: Schematic of a perforated plate.

same noise mechanism and have similar characteristic length scales. Also the small perforated plate 2 has a peak **A** value of St_L at approximately 18.

In summary, the frequencies of the first two identifiable peaks, **A** and **B**, were found to scale with velocity but a characteristic length scale was not found. The candidate length scales considered in this analysis were chosen such that they correspond to the most critical lengths thought to be important for the noise generation mechanisms of perforated drag plates. It is hypothesized then that a characteristic length scale does not exist. This will be the case if the noise is mainly due to isotropic turbulence generated behind such a perforated plate.

The next section presents the noise assessment of the perforated plates and configurations from a drag and noise perspective.

5.3 Noise Assessment of the Perforated Plates and Configurations

The objective of this assessment is to identify the region in the parameter space which is the most beneficial for noise reduction. To have a fare comparison this assessment must be done on an equivalent drag basis.

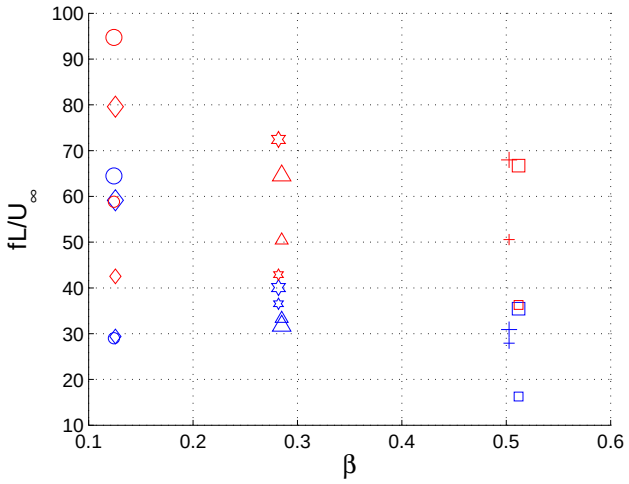

Figure 5-21: St_L variation with plate non-dimensional parameters. Peak **A** data is in blue, while peak **B** data is in red. Small and large markers correspond to the small and large plates, respectively.
'◇' PP1; '□' PP2; '+' PP3; '○' PP4; '△' PP5; '⊛' PP6.

The drag coefficient and Strouhal number variation with plate porosity, obtained experimentally by Castro [14], were used in this assessment. Table 5.2 shows the six perforated plates with their corresponding porosity based on which the drag coefficient and Strouhal number were determined [14]. The corresponding characteristics are also shown for a solid plate. The drag coefficients vary between the plates. This is expected as discussed in Section 2.3. In order to compare the noise signature, a reference plate or plates should be chosen and the rest of the plates must be scaled such that all plates generate the same amount of drag.

A solid plate with $L = 0.2$ m was chosen as a reference plate. In this way all the plates (small and large) can be compared on the same drag basis. The perforated plates are scaled in size such that they generate the same amount of drag, expressed as

$$D = \frac{\rho U_\infty^2}{2} C_{D_{PP}} A_{PP}, \tag{5.7}$$

where $C_{D_{PP}}$ and A_{PP} are the perforated plate drag coefficient and area, respectively.

Table 5.2: Porosity, drag coefficient and Strouhal number of the tested perforated drag plates.

Plate	β	C_D	St_L
Solid Plate	0	1.89	0.140
Perforated Plate 1	0.1257	1.69	0.150
Perforated Plate 2	0.5118	1.00	0.212
Perforated Plate 3	0.5027	1.00	0.212
Perforated Plate 4	0.1242	1.69	0.150
Perforated Plate 5	0.2850	1.24	0.135
Perforated Plate 6	0.2819	1.24	0.135

Table 5.3: Area increase factors for the tested perforated plates.

Plate	**AIF**	
	L_1	L_2
Perforated Plate 1	4.47	1.12
Perforated Plate 2	7.56	1.89
Perforated Plate 3	7.56	1.89
Perforated Plate 4	4.47	1.12
Perforated Plate 5	6.10	1.52
Perforated Plate 6	6.10	1.52

Thus, for plates 1 to 6 the area increase can be calculated from

$$AIF = \frac{C_{D_{SP}}}{C_{D_{PP}}} \frac{A_{SP}}{A_{PP}}. \tag{5.8}$$

The drag coefficients from Table 5.2 were then used to calculate the area increase. The results are summarized in Table 5.3.

Next a noise metric should be chosen based on which the plates are assessed and compared. As such, the overall sound pressure level (OASPL) was chosen. In order to get the OASPL of the plates only, the noise spectra of the horizontal plate alone were subtracted from the noise spectra of the plates on absolute level. However, at low frequencies the Markham wind tunnel is noisy (SPL of 80 dB at 100 Hz) and the perforated plate noise spectra within this region are essentially contaminated by the

background noise.

On the other hand, the overall sound pressure level of the plates, should also account for the low frequency region. The low frequency model developed in Section 6.1.1 is used to calculate the spectra in this region. The model assumes a Gaussian distribution to model the spectrum of the drag coefficient. Thus, if the plates generate the same drag, the OASPL within this region will be identical. For the present purpose, only the relative difference between the OASPL is needed for noise assessment of the plates. Thus, this model is not used here.

An attempt was made to determine the low frequency spectra of the same plates by conducting acoustic tests in the acoustic chamber at MIT. For this purpose the plates were mounted in the drag rudder configuration 1 but a single rod instead of a horizontal plate was used to hold the plate in place. The rod of diameter 0.011 m creates shedding noise at 540 Hz which is above the low frequency range that was being examined. The results are not shown here as the background noise in the acoustic shed was found to be also high (SPL of 65 dB at 20 Hz) and a proper spectra in the low frequency region was not obtained. In order to get the low frequency spectra, hot wire measurements are needed. This, as already mentioned, is left for future work.

The perforated plate area is increased by the area increase factor, AIF such that all the plates generate the same drag. The OASPL levels obtained from the measurements in the Markham wind tunnel should also be scaled to account for the area increase. Next, the assumption was made that noise sources within a perforated plate are sufficiently incoherent that an increase in plate (source) area causes an equivalent increase in the acoustic power. The correction for the area increase was applied to the OASPL as follows

$$OASPL_{PP_{corr}} = OASPL_{PP} + 10\log_{10}(AIF_{PP}), \tag{5.9}$$

where $OASPL_{PP}$, AIF_{PP} and $OASPL_{PP_{corr}}$ are the OASPL obtained from the acoustic measurements, the area increase factor from Table 5.3 and the corrected OASPL

Table 5.4: OASPL corrected for drag.

Plate	**L1**	**L2**
	40 m/s	40 m/s
Perforated Plate 1	86.4237	86.0692
Perforated Plate 2	86.3331	88.1836
Perforated Plate 3	85.6723	105.5221
Perforated Plate 4	87.6728	87.6984
Perforated Plate 5	87.9989	87.9790
Perforated Plate 6	84.9916	84.5689

for the area increase, respectively.

A comparison was made based on the corrected OASPL for 40 m/s, which is the test velocity closest to the full scale Silent Aircraft SAX10 approach velocity of 75 m/s. The overall sound pressure levels corrected for the area are shown in Table 5.4. $L1$ and $L2$ are the plates corrected for an area increase from the small (L_1) and large (L_2) plates, respectively. It can be seen that the corrected OASPL of the small plates is approximately the same as the corrected OASPL of the large plates. The only substantial difference is for plate 2 and 3. This difference is due to the fact that for these plates distinct tones were observed. At 40 m/s the large perforated plate 3 has a very distinct tone of around 100 dB (see Figure B-21). From Table 5.4 it can also be seen that perforated plate 6 has the lowest values of OASPL.

If plates 1, 2, 3 ,4 and 5 are compared since they are in the same region in the parameter space Figure 5-5, the small plate 3, which also has the highest porosity, has the lowest OASPL. However, comparing plates 1 through 5 to plate 6, a noise reduction of up to 3 dB in OASPL levels is achieved. Plate 6 has the same porosity as plate 5 but the overall sound pressure levels are lower even compared to plate 3.

As mentioned before, perforated plate 6 was the only plate for which no tones were observed. It was hypothesized that this is due to the fact that this plate has very porous edges. This relieving to the plate edge effect is may be the main cause of the lower OASPL values.

Based on the discussed above, perforated plate 6 seems to be the most beneficial

Table 5.5: Calculated speed dependance n of plate noise levels for perforated plate 6.

Velocities for scaling	Peak **A**		Peak **B**	
	L_1	L_2	L_1	L_2
20 m/s to 30 m/s	2.8508	4.3500	3.4584	2.8565
20 m/s to 40 m/s	3.5810	4.3982	4.1823	3.6807
30 m/s to 40 m/s	4.6103	4.4662	5.2025	4.8424
Average	3.68	4.04	4.28	3.79

plate from both a drag and noise perspective.

In order to establish a prediction model for the full size drag device, an attempt was made to scale the SPL spectra of the most beneficial perforated plate 6 with plate size and free stream velocity. To investigate how the SPL of plate 6 varies with velocity, it is useful to normalize the noise spectra levels. The scaling was done based on peaks **A** and **B** which are the most distinct features in the spectra and are found to scale with velocity. Thus, the normalized sound pressure level, $SPL_{P_{norm}}$ is given by

$$SPL_{P_{norm}} = SPL_P - 10\log_{10}(U_\infty^n), \tag{5.10}$$

where SPL_P is the peak sound pressure level determined from the acoustic measurements and n denotes the exponent of the speed dependance. This is a good approximation since sound intensity p_a^2 is proportional to tunnel speed U_∞^n, with p_a being the acoustic pressure.

A set of values of n were obtained for peaks **A** and **B** scaling the SPL between the free stream velocities for which data were available. Table 5.5 summarizes the exponents n for perforated plate 6.

Figures 5-22 and 5-23 show peak **A** and **B** sound pressure levels plotted as functions of the free stream velocity. The peak SPL are plotted with error bars to account for the uncertainty with which the peak SPL were determined. The assumed uncertainty is -3 dB. Thus, it is possible that the magnitudes of the peaks could be collapsed using the power law given in Equation 5.10. Indeed, as can be seen from Table 5.5 peak **A** for the large plate can be collapsed using an average n of 4.4. It is

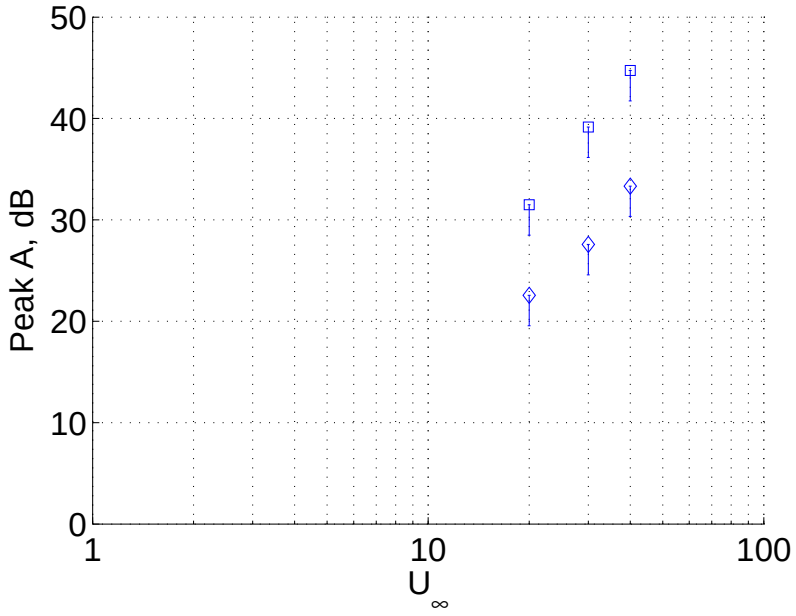

Figure 5-22: Peak **A** sound pressure levels as a function of the free stream velocity.

not be clear if a velocity scaling of the peak SPL exists, because of the sensitivity to the choice of peak SPL. If such velocity power indeed exists, then n will probably be around 4.0.

In order to investigate how the sound pressure level scales with the plate size a comparison can be made between the large and small plate. The ratio of all the geometric characteristics, except the plate thickness which was kept the same, is equal to 2.0. Therefore, if it is assumed that the noise sources for the perforated plate are incoherent then an increase in source area causes an equivalent increase in the acoustic power, or for ratio of 2 the corresponding increase should be $20\log_{10}(2) = 6$ dB. Here the overall sound pressure levels of the small and large plates at 40 m/s are compared. This is done because no characteristic length was found to scale the peaks and therefore collapsing on a peak by peak SPL basis is not appropriate. The OASPL of the small perforated plate at 40 m/s is 77.1 dB, while the OASPL for the large plate at 40 m/s is 82.8 dB. Thus, the difference in the overall sound pressure levels is 5.7 dB. It was assumed, therefore, that the overall sound pressure levels scale with size, such that an increase in source area causes an equivalent increase in the

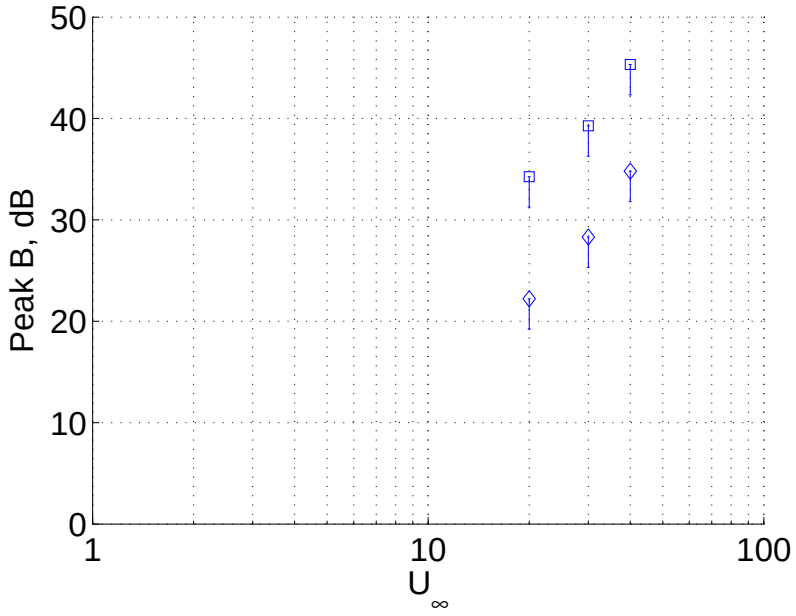

Figure 5-23: Peak **B** sound pressure levels as a function of the free stream velocity.

acoustic power.

Finally, a comparison was made between the four different configurations tested. Figure 5-24 shows the noise spectra of perforated plate 6 at 40 m/s which is the closest speed to the full scale SAX10 approach speed of 75 m/s. The shown spectra are for the large plate with $L_2 = 0.2$ m.

As can be seen from Figure 5-24, all configurations have equivalent distinct features (peaks). However, while spoiler configuration 1, and the two drag rudder configurations have comparable sound pressure levels, the spectra of the spoiler configuration 2 is approximately 20 dB below these spectra. This was observed for all plates but only the spectra of perforated plate 6 are shown, which is considered to be the most beneficial plate from both a drag and a noise perspective. Therefore, the most beneficial plate for noise reduction is spoiler configuration 2, a perforated plate mounted on the wing shielding the noise for an observer on the ground.

To summarize, the most beneficial plate in terms of noise reduction was found to be perforated plate 6 ($d/L = 0.013$, $s/L = 0.0217$ and $\beta = 28.19\%$). The quietest configuration is a spoiler configuration with the spoiler mounted on the top surface

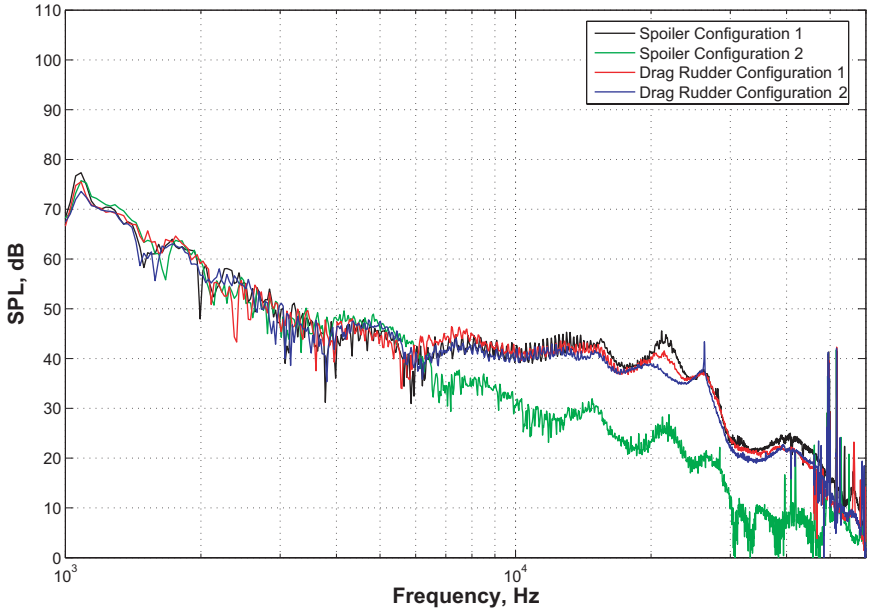

Figure 5-24: Noise cross spectra for the large ($L_2 = 0.2$ m) perforated plate 6 at $U_\infty = 40$ m/s for the four installation configurations.

of the wing. In order to scale to full size, a velocity scaling law of the observed peaks is suggested with the caveat that there is peak SPL data. If such a power low indeed exists, then the exponent n will probably be around 4.0. The overall sound pressure levels were found to scale with size, such that an increase in source area causes an equivalent increase in the acoustic power.

5.4 Summary

Using advanced equipment such as the acoustic phased array it was possible to identify the noise sources of perforated plates in a closed loop wind tunnel.

The analysis of the test results showed that there are two peaks, identifiable in all plates and configurations, whose frequencies scale with velocity. Different candidate length scales were used to collapse the data but an universal characteristic length could not be found.

A recommendation for the Silent Aircraft was made for a potential drag device. In the parameter space plate 6 was identified to be the most beneficial drag device

for noise reduction. The quietest drag device installation configuration, the spoiler mounted on the top surface of the wing, was also assessed.

An attempt was made to scale the spectra of the candidate plate for a quiet drag device in terms of plate size and free stream velocity. The overall sound pressure levels were found to scale with size, and with the free stream velocity to the power 4.0.

An open question is still the low frequency noise signature of the perforated plates. Only highly anechoic acoustic chamber or hot wire measurement are suggested to shed light on the low frequency noise. This is left for future work.

Chapter 6

Drag Rudder Noise Assessment for SAX10 Design

This section includes the methodology and fidelity of the drag rudder noise estimation for the current Silent Aircraft eXperimental SAX10 design (Figure 1-5). The technical approach involves two prediction models: one for low frequencies and the other for high frequencies. The preliminary drag rudder design together with the full-scale noise signature are provided next. The chapter is concluded with recommendations for the current Silent Aircraft.

6.1 Technical Approach

6.1.1 Bluff-body Noise Model (Low Frequencies)

The characterization of the MIT Acoustic Chamber showed that 540 Hz is the lowest frequency for which the microphones are in the far field. Thus, the bluff-body noise, which occurs at low frequencies, cannot be measured directly. In what follows is a simplified noise prediction tool (based on a dipole sound source) that was developed to predict the noise caused by this mechanism.

Aerodynamic loads on foreign bodies are acoustically equivalent to dipole sources of sound, much less efficient radiators than monopoles when the sources are compact

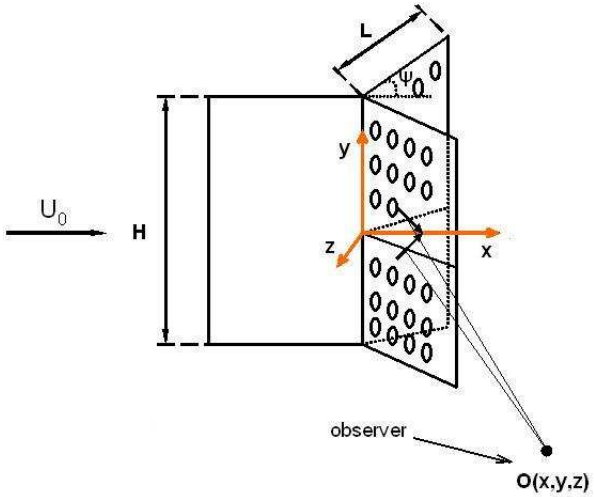

Figure 6-1: Dipole model.

but nosier than their surrounding turbulent flow. The radiated sound intensity from an acoustically compact rigid body is proportional to the mean square of the time derivative of the force:

$$\overline{p_a^2(x)} = \frac{1}{16\pi^2 a_\infty^2} \frac{\cos^2\theta}{r^2} \overline{\left(\frac{\partial F(t)}{\partial t}\right)^2}. \tag{6.1}$$

In Equation 6.1, θ is measured from the direction of the fluctuating force vector, r is the distance to the observer and a_∞ is the speed of sound. The bluff-body noise source of the drag rudder is modeled by dipoles that are located in the geometric center of each of the perforated drag plates (Figure 6-1).

No lift is generated by the drag rudder and so the only force for the drag rudder is the drag force in the x-direction. The drag oscillatory force is assumed harmonic and may be written as

$$F_x(t) = \frac{\rho U_0^2}{2} C_D(\beta) A_{plate} e^{jw_d t}, \tag{6.2}$$

where w_d is frequency in rad/s and $C_D(\beta)$ is the drag coefficient as a function of the plate porosity [14]. Since for low Reynolds number, Re, the drag fluctuations are due to disturbances that are spatially symmetric about the wake axis and are generated twice as each vortex pair is produced, the fundamental frequency of the

drag fluctuations, w_d, is $2w_s$. Also, $w_s = 2\pi f_s$. Here f_s is the vortex shedding frequency in Hz.

The unsteady drag force is assumed harmonic, so the mean square of the time derivative of the drag force is

$$\overline{\left(\frac{\partial F(t)}{\partial t}\right)^2} = \frac{1}{2} w_d^2 \left(\frac{\rho U_0^2}{2}\right)^2 C_D^2(\beta)(A_{plate})^2. \tag{6.3}$$

The fluctuations in drag force may be expressed in terms of the spectral distribution $F_x(f)$ through a Fourier Transformation as

$$F_x(f) = \frac{\rho U_0^2}{2} C_D(f) A_{plate}, \tag{6.4}$$

where f is the frequency in Hz. For low Reynolds number, Re, $f = f_s$ is the vortex shedding frequency in Hz. The value of f_s, for a 40% porosity perforated drag plate over a range of Reynolds numbers ($2.5 \times 10^4 \leq Re_L \leq 9 \times 10^4$), is given by Castro [14] in terms of the non-dimensional shedding Strouhal number, $St_s = f_s L/U_0 \cong 0.15$. Figure 6-2 shows the propagated bluff-body noise in the $X - Z$ plane at the peak frequency for the low Reynolds number case. The noise signature of the superposition of the two dipoles can be seen.

The Reynolds number for the full-scale drag rudder is 2×10^6. At high values of Re, vortex shedding has a broad frequency distribution resulting in a broadband drag coefficient spectrum. To simplify the analysis, a Gaussian distribution was being used to model the drag coefficient spectrum:

$$C_D(f) = C_D(f_s) \frac{1}{\sigma\sqrt{2\pi}} e^{-\frac{(f-f_s)^2}{2\sigma^2}}, \tag{6.5}$$

where f_s is the center frequency of spectral distribution, $C_D(f_s) = 1.1$ is the drag coefficient for a 40% porosity perforated drag plate at low Reynolds number and $\sigma = 1/3\Delta St(U/L)$ is the scale parameter with $\Delta St = \Delta f L/U_0$. Δf is the $3\Delta\sigma$ difference in frequency ($f_{3\sigma} - f_s$).

Figure 6-3 shows the SPL of the low frequency bluff-body noise for different values

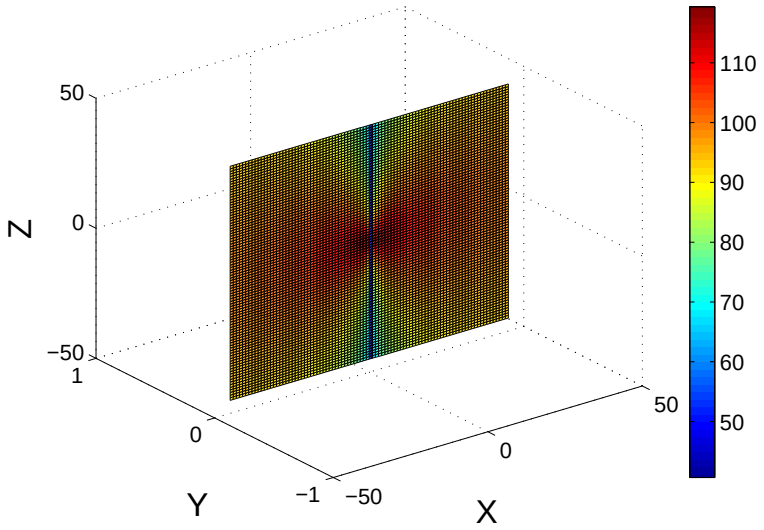

Figure 6-2: Bluff-body noise signature for $\psi = 90°$ in the $X-Z$ plane for $C_D(f_s)$=1.1. Orientation defined in Figure 6-8.

of ΔSt. The single point is the drag coefficient value for low Reynolds number flow. Based on the data given by Schewe [29], the value of ΔSt was taken as 0.2. The drag coefficient and acoustic spectra are plotted in Figures 6-4 and 6-5, respectively. The peak value for the high Reynolds number acoustic spectrum (Figure 6-5) is 20 dB lower than the low Reynolds number spectral peak due to spectral broadening. Thus, the low frequency noise for high Reynolds number has lower SPL, although the OASPL for the low-frequency content will be the same.

6.1.2 Turbulent Mixing Noise Model (High Frequency)

Higher frequency noise (high compared to the bluff-body noise) from perforated drag rudder is due to the interaction of the turbulence within the wake and the turbulence within the jetlets formed by the perforations. The high-frequency noise model of the perforated drag plate has two length scales. One is associated with the perforations (small length scale). The other is associated with the plate size (large length scale). Dimensional analysis (Section 2.2) revealed that the high-frequency noise signature

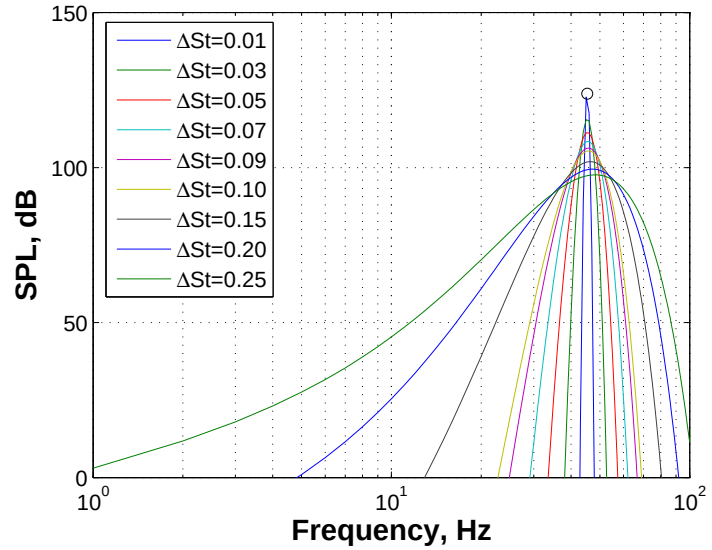

Figure 6-3: Low frequency bluff-body noise SPL for different ΔSt.

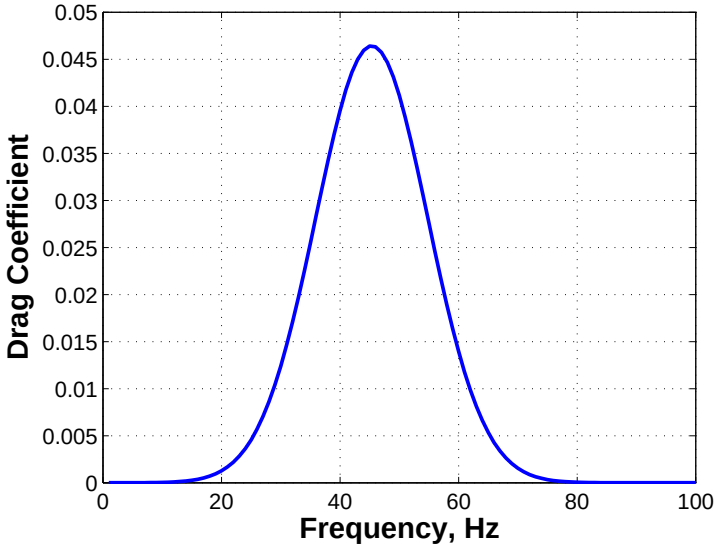

Figure 6-4: Drag coefficient frequency spectrum for $\Delta St = 0.2$.

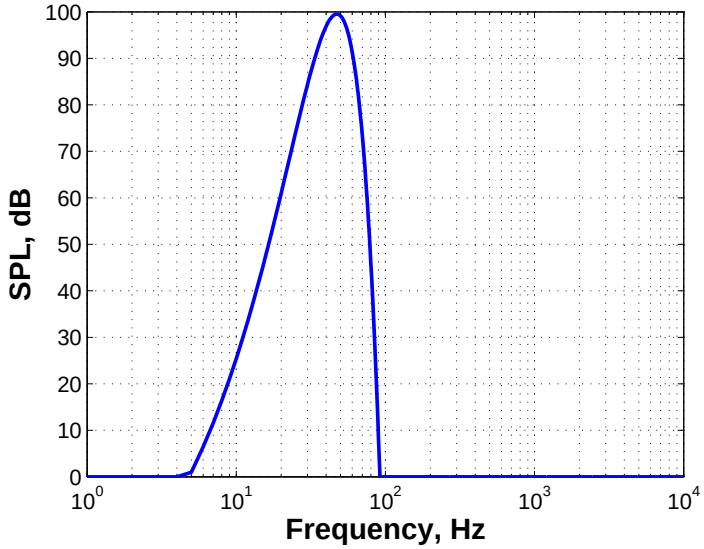

Figure 6-5: Low frequency bluff-body noise SPL. Observer is 100 ft (30.5 m) away from the source in direction of maximum sound emission.

is of the form

$$SPL = f\left(\frac{x}{L}, \frac{y}{L}, St_L, Re_L, M, \frac{d}{L}, \frac{H}{L}, \psi\right), \tag{6.6}$$

where M is the free stream Mach number, Re_L and St_L are the Reynolds and Strouhal numbers based on a characteristic rudder length, L, d is the perforation diameter, x and y are the perforation separation distances, and ψ is the deployment angle. The turbulence mixing noise is assumed to have uniform directionality.

To model the noise from the turbulent mixing, the acoustic measurements carried out in the acoustic chamber at MIT were used.

Figure 6-6 shows the sound pressure level for a perforated drag plate having 40% porosity at three different free stream test velocities. The data was scaled based upon $St_d = St_L \times d/L$. This Strouhal number was used to align the high frequency features of the spectra as it is believed that the perforation diameter is the driving length scale. Figure 6-6 has three marked Strouhal number ranges. The acoustic data within the lower range (under $St_d = 0.4$, 800 Hz) was deemed unreliable due to high wind tunnel noise levels. The acoustic data within the upper range (above $St_d = 1.3$, 2.5 kHz) is not important to the noise prediction model since these frequencies are

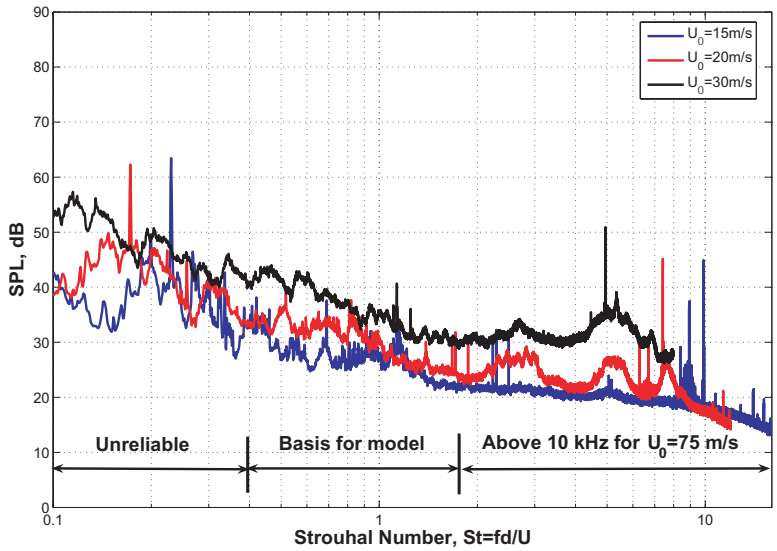

Figure 6-6: Measurements of SPL for a 40% perforated drag plate at free stream velocities of 15, 20 and 30 m/s.

above 10 kHz when scaled to the approach velocity of 75 m/s. The middle range was used to estimate the turbulence mixing noise from the perforated drag rudder.

The estimate of the full-scale perforated drag rudder turbulence noise was created from extrapolating the 20 m/s, 40% perforated drag plate experimental acoustic data (Figure 6-6) to the full-size drag rudder at the approach velocity of 75 m/s. The most important step in this process was determination of how the peak amplitude scaled with velocity. The difference between the 40% perforated spoiler acoustic spectra and the solid spoiler (not shown), on absolute level, was determined for 20 m/s and 30 m/s. The amplitudes of these data were scaled using a velocity power law, $p_a^2 \propto U^n$. The values of n varied from 4.8 to 6 for frequencies between 1.1 and 1.4 kHz. These values of n were used with the ratio of the experimental perforated drag plate area to the full-scale drag rudder area to provide the peak amplitude noise estimate. The full-scale drag rudder perforation diameter was set to be the same as that of the experiments, so this parameter does not need to be scaled. The full-scale peak frequency was assumed to be at the center of the middle frequency range (1.1 to 1.4 kHz). The turbulence mixing noise spectrum was assumed to have an f^2 dependance for frequencies lower than the peak and a $1/f^2$ dependence for higher frequencies

[30]. The full scale SPL was also corrected for the distance to the observer using the inverse square law.

6.1.3 Uncertainty Analysis

The bluff-body noise mechanism which characterizes the low frequency spectrum of the perforated drag rudder noise signature is modeled using dipole point sources. This assumes that all the acoustic energy due to the aerodynamic load is in the center of each of the plates of the drag rudder.

The next assumption is connected to the mean square of the time derivative of the fluctuating force that was used to find the dipole strength. At low Reynolds number, vortical structures behind a bluff-body are shed at a single non-dimensional frequency. Based on this low Re drag coefficient was calculated [14]. At high Reynolds numbers the drag coefficient has some distribution over the frequency range and a Gaussian distribution was assumed to fit the test data obtained from circular cylinder lift coefficient measurements [29]. The uncertainty for low frequency noise is estimated at ± 5 dB due to uncertainty in ΔSt.

The turbulent mixing noise (high frequency noise) was estimated based upon extrapolation of experimental data. In the tests additional noise was generated due to the interaction of the perforated plate and the horizontal plate on which the test models were secured. This does not resemble the real situation where there is no splitter plate between the two perforated plates of the drag rudder. Also, the scaling of the two peaks was done based on only two data points (20 and 30 m/s) and the scaling velocity power coefficients could be different for scaling at higher velocities (75 m/s). An error estimate of ± 9 dB was assumed.

6.2 Design Implications

In order to assess the required drag that needs to be generated in a quiet way, the change in drag coefficient, ΔC_D, required for a given approach trajectory must be examined. The term ΔC_D represents the drag (or thrust) over and above that pro-

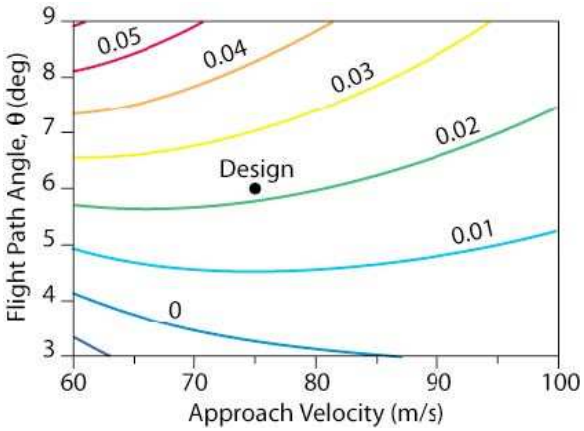

Figure 6-7: Change in drag coefficient, ΔC_D, required to balance the lift and drag over a range of approach trajectories [5].

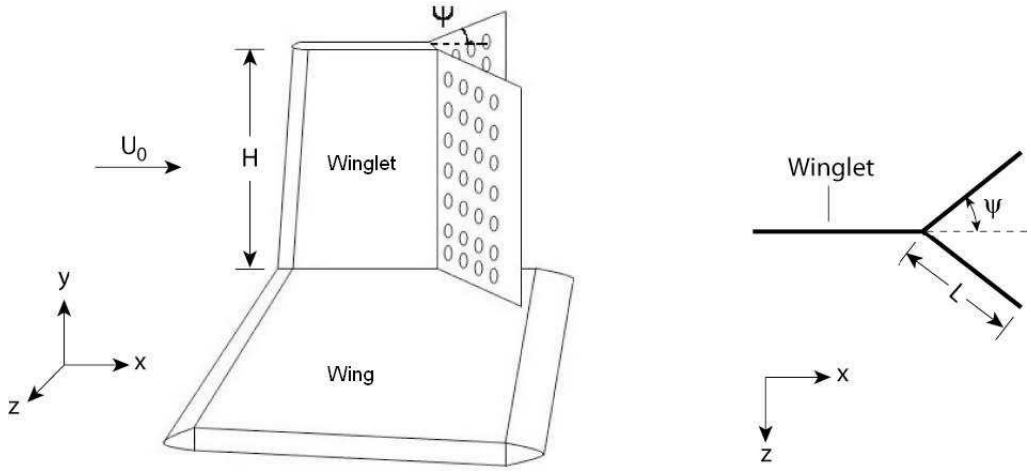

Figure 6-8: Drag rudder geometry (two views).

duced by the airframe not including the thrust of the engines at idle conditions. This drag has to be created to balance the lift and drag forces acting on the aircraft for a given flight path trajectory (defined by flight path angle and velocity) [31].

$$\Delta C_D = \Delta C_{D,req} - \Delta C_{D,prod} = \frac{D_r - D_p}{\frac{1}{2}\rho U_0^2 A}, \tag{6.7}$$

The value of ΔC_D is shown in Figure 6-7 as a function of flight path angle and approach velocity. It is proposed that the drag be generated by using drag rudders positioned at the winglets of the aircraft (Figure 6-8).

Using the data for the drag coefficient $C_{D,drag\ rudder}$ as a function of the plate porosity [14], the required chord percentage x of the winglet to be used for a drag rudder can be calculated:

$$x = \frac{\Delta C_D A}{C_{D,drag\ rudder} n (A_{winglet} \sin\psi)}\%. \tag{6.8}$$

The area, $A = 754$ m^2, is the SAX10 wing area, $A_{winglet} = 13.3$ m^2 is the winglet area, $n = 4$ is the number of perforated drag plates (two on each winglet), and ψ is the drag rudder deployment angle.

For the current noise assessment, the drag rudder was assumed to have a porosity of 40% and deployment angle of 90°. The 40% porosity plate was chosen as a tradeoff between the increased size (50% larger than a solid drag plate) required to obtain ΔC_D and the anticipated decrease in noise caused by the decreased turbulence length scales. For a 40% perforated drag plate, $C_{D,drag\ rudder}$ is 1.1 [14] and approximately 30% of the winglet would need to be deployed as a drag rudder.

6.3 Full Scale Noise Signature of Perforated Drag Rudders

Using the procedures described above for the low and high frequency ranges, a full scale noise spectrum of Figure 6-9 was generated. This spectrum represents the noise at a 100 foot (30.5 m) hemisphere in the direction of maximum sound emission of large length scales (bluff-body noise). The SPL spectrum was obtained by adding, on absolute levels, the two noise signatures. The 1/3-octave-band sound pressure level is also shown in the figure.

For each of the 1/3-octave-band center frequencies the noise has been propagated to a 100 foot (30.5 m) hemisphere. Two frequency bands are shown in Figures 6-10(a) and 6-10(b). These are for center frequencies of 50 and 1600 Hz which represent the peak frequencies of the bluff-body dipole noise (low frequency) and turbulence mixing noise (high frequency). Figure 6-10(a) shows the bluff-body noise directivity

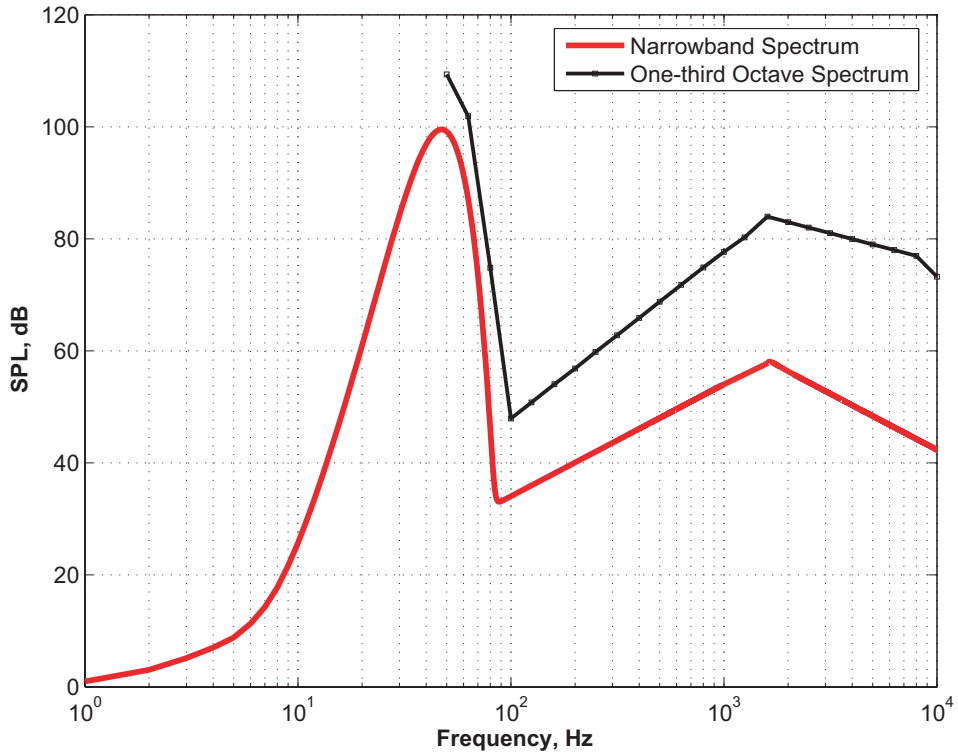

Figure 6-9: Full scale drag rudder noise scaled from measurements and dipole model. Observer is 100 foot (30.5 m) from rudder direction of maximum sound emission.

(the dipole directivity is shown by the lowered intensity along $x = 0$). Figure 6-10(b) shows the assumed uniform directivity for the turbulence mixing noise.

Figures 6-10(a) and 6-10(b) are for a single drag rudder. However, SAX10 has two drag rudders, one on each winglet. The two noise signatures were summed, on absolute basis, to yield the noise hemisphere. Overall sound pressure levels (OASPL) for the noise hemisphere are shown in Figure 6-10(c) in terms of A-weighted decibels (dBA). The values are between 50 Hz and 10 kHz.

6.4 Noise Audit

A noise audit and performance of the current state of the Silent Aircraft configuration as of January 2005 has been carried out [5]. For each airframe component, noise spectra were computed on 2° azimuthal and polar increments at a radial distance of 100 foot (30.5 m) to create a noise hemisphere. Then the acoustic energy from the aircraft was propagated to the ground. For the SAX10 design noise audit, the propagation calculation, based on ESDU [32] propagation modules, captured geometric attenuation due to the spherical spreading, atmospheric attenuation, lateral attenuation, and ground reflections [33]. Figure 6-11 gives an overview of these propagation effects, which are applied in the numbered order in the figure.

Noise footprints were calculated for specific points on the trajectory. Even though the noise levels from the perforated drag rudder are larger than those of the other airframe components, the addition of the perforated drag rudder leads to a 4 dBA reduction in cumulative sound pressure levels because it allows a 6° flight path [5].

6.5 Recommendations

Based on the acoustic phased array tests performed in the Markham wind tunnel at Cambridge University, a recommendation for the Silent Aircraft was made for a potential drag device. The most beneficial for noise design region is where the porosity of the plates is achieved by many small perforations of $d/L = 0.013$ spaced closely

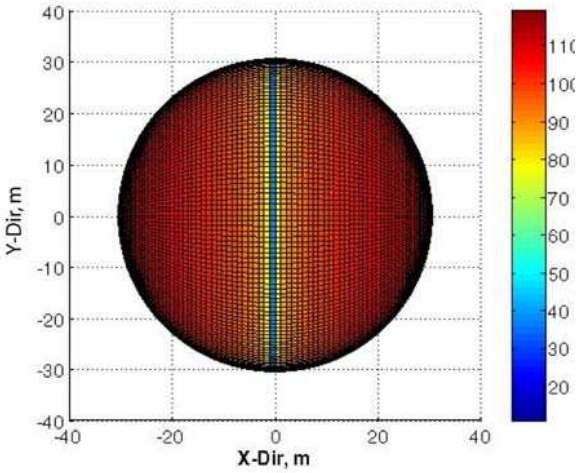

(a) Drag rudder noise signature at 50 Hz

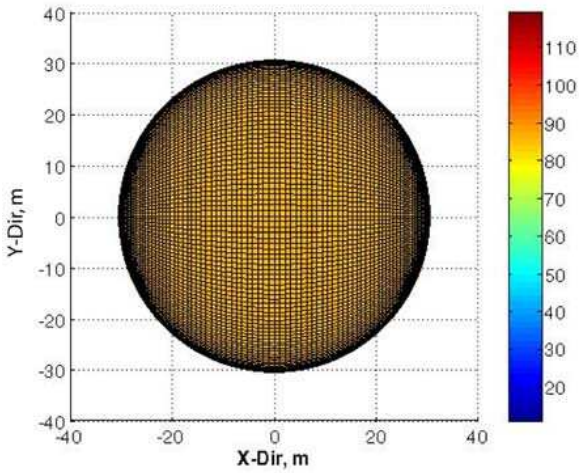

(b) Drag rudder noise signature at 1600 Hz

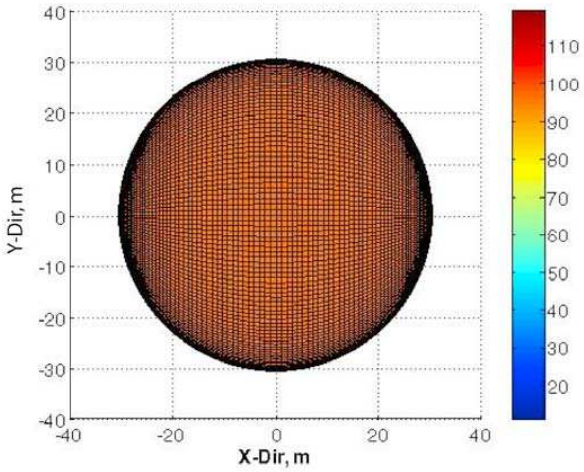

(c) Perforated drag rudder noise hemisphere for SAX10. Values are cumulative A-weighted noise (OASPL, dBA) between 50 Hz and 10 kHz.

Figure 6-10: Perforated drag rudder noise hemispheres

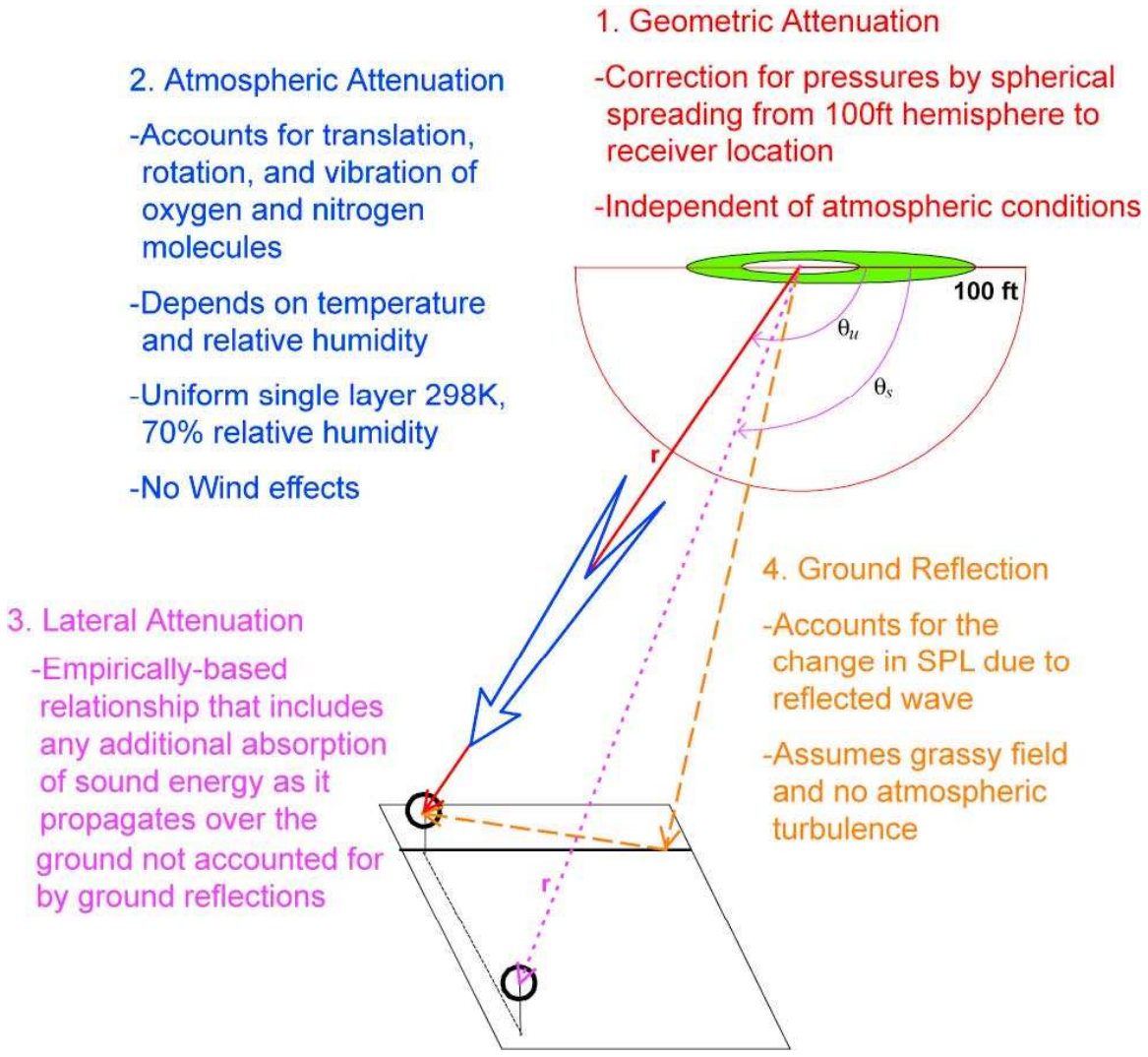

Figure 6-11: Overview of propagation effects [33].

by $s/L = 0.0217$. Here large and small are defined with respect to the length of a perforated plate. The small distance of the perforations to the plate edge relieves the plate edge and a tone (observed for some spectra) is not produced.

The quietest drag device configuration was also identified. A perforated spoiler mounted on the upper airfoil surface is quieter than a drag rudder configuration because some of the turbulent mixing noise sources are shielded from the ground by the airfoil. This will further reduce the aircraft airframe noise on a 6° flight path.

An attempt was made to scale the spectra of the candidate for a quiet drag device perforated plate 6 for plate size and free stream velocity. In order to scale to full size, a velocity scaling law of the observed peaks is suggested with the caveat that there is peak SPL data. If such a power low indeed exists, then the exponent n will probably be around 4.0. The overall sound pressure levels were found to scale with size, such that an increase in source area causes an equivalent increase in the acoustic power.

Chapter 7

Conclusions and Future Work

7.1 Conclusions

The objective of the Silent Aircraft Initiative (SAI) is to achieve a step-change in aircraft noise reduction and this will require a radically different approach to the problem. In order to reduce airframe and propulsion system noise levels below the background noise in a well-populated area, noise must be a prime design variable. It is also clear that conceptually new aircraft configuration should be studied. A blended-wing-body type aircraft configuration with aerodynamically-smooth lifting surfaces is a potential candidate to achieve the airframe noise reduction goals. However, mitigating airframe noise emissions by removing the high-lift devices (leading edge slats and trailing edge flaps) invariably leads to a reduction in the drag. Thus, one of the most critical tasks in noise reduction is to develop technologies to increase drag in quiet ways.

So far, relatively little analysis has been done to investigate the possibility of generation drag quietly. It is misleading to only consider noise suppression without considering the associated performance (drag generation) penalty. Therefore, silent drag concepts should be investigated to determine how much drag could be produced with satisfactory noise reduction.

One way to dissipate the energy on approach is to use low-noise high-drag structures. Conventional spoilers create drag in a very noisy manner. The processes that

lead to drag on such bluff bodies involve unsteady wakes and inevitably generate noise.

The idea behind a silent spoiler/drag rudder is to alter the noise production mechanism by perforating the solid plates. The large length scales responsible for the noise radiated by unsteady vortical structures can be changed to small length scales driving jet noise. Jet and jet noise studies [6, 7] suggest that the peak frequency associated with mini-jets is shifted to higher frequencies and that the mini-jets interfere to produce a lower peak sound pressure level. On the other hand, atmospheric attenuation, increases nearly exponentially with increasing frequency, and spectral noise components contribute less to EPNL noise metric as the frequency increases above 4 kHz. Humans have a low sensitivity to acoustic frequencies above 10 kHz and noise at frequencies higher than 10 kHz is not included in the calculation of EPNL. This idea may be applied to the noise produced by a perforated plate resembling an array of low speed mini-jets. The perforated spoilers/drag rudders could help reduce noise produced by current and future generations of aircraft.

One of the main problems of designing quieter drag devices is that current analytical models do not accurately predict the noise that would be emitted by such designs. Therefore, it is necessary to build an actual model and conduct tests to determine the potential noise reduction using such silent drag devices.

The work presented in this thesis focused primarily on aeroacoustic tests and analysis of low-noise high-drag deployable structures such as perforated drag plates.

A preliminary acoustic campaign was conducted at the acoustic chamber at MIT. Acoustic tests of six perforated plates and one solid plate in a spoiler configuration were tested. The data from these preliminary tests was also used to size test articles for acoustic phased array tests conducted in the Markham wind tunnel at Cambridge University. These tests along with a discussion of the results were given.

Description of Noise and Drag Mechanisms of Perforated Drag Plates

Chapter 2 addressed the noise mechanisms and dimensional analysis of the important geometric and flow parameters that govern the noise generation of a perforated drag plate. A drag analysis to investigate the effect that perforations have on the drag generation of such perforated plates is also included.

The true noise sources of aerodynamic noise are the fluid disturbances themselves. The interaction of these disturbances with airframe structural discontinuities causes substantial sound radiation. Three major noise source mechanisms associated with a perforated drag plate were identified.

- **Bluff-body noise** due to the flow separation at the side edge. The unsteady motions in the shear layer are a major noise source.
- **Turbulence mixing noise** by the individual jetlets that comprise the perforated drag plate and their interaction with the bluff-body wake.
- **Panel vibration noise** due to the mechanical vibrations of the plate.

These three noise mechanisms are not separated but are strongly coupled. This makes the individual identification very complicated. This complication is reduced then by a dimensional analysis identifying the important non-dimensional groups that govern these noise mechanisms. Except the obvious Mach number, Strouhal number and Reynolds number, important for the noise generation are the vertical and horizontal perforation separation, and perforation diameter. The length scale based on which or with which these parameters were non-dimensionalized is the length, L, of the plate.

The optimal perforated drag plate is one that achieves a balance of reducing the noise without sacrificing the drag generating ability of the plate. A drag analysis was conducted to find an analytical relationship between the plate porosity and drag coefficient. This analysis is based on the theoretical work been developed by Taylor [13] and experimental data from Davies [16]. It became obvious that a more thorough

understanding of the flow behind a perforated plate is needed in order to model analytically the drag coefficient as a function of plate porosity.

Next a hypothesis was established concerning the flow behind a perforated plate. It was hypothesized that if the porosity is high enough the flow will change its characteristics from dominated by the vortex street to dominated by turbulence or from large length scale structures dominated to small length scale structures dominated.

A bluff body usually sheds two shear layers which are unstable and interact in the near wake, rolling up to form a vortex street. If the two separating shear layers are prevented from interacting in the usual way the vortex formation may be delayed and the vortex formation point moves downstream. When the plate is perforated extra air is injected between the two shear layers and they cannot meet but they still interact.

At low values of porosity the two shear layers are not prevented from interacting and they form a vortex street that will dominate the wake. As the porosity increases, more bleed air is introduced, the vorticity in the shear layers decreases. There is also a corresponding increase of base pressure and hence a decrease in drag. Thus, the vortex street strength gradually decreases when the porosity increases. This also reduces the noise levels at low frequencies that are mainly due to the vortices shed by the plate.

As the plate porosity increases, the extra air injected increases and if enough air is injected the two shear layers could be prevented from interacting at all. To conserve the mass balance across the wake there still has to be a reversed flow region, and this moves downstream with increasing β.

The observed abrupt changes in C_D and St by Castro [14] proved that there indeed exist two flow regimes behind the perforated plate, one at low porosity and the other at high porosity of the plate. The critical value of β seems to be of about 0.2. In one, appropriate to low values of porosity, the vortex street (large length scales) dominates the wake. In the other, at high values of porosity the small length scales dominate the wake.

MIT Acoustic Chamber Design and Instrumentation

Chapter 3 addressed the acoustic test equipment used for preliminary test campaign conducted in the MIT acoustic chamber. The procedure for microphone calibration is also included together with the description of the data reduction technique used.

Although the walls of the MIT acoustic chamber are covered with sound absorbing foam, the characterization of the chamber with acoustic point source showed that the microphones are not in the free field. A possible explanation is that the chamber is too small for free field conditions to exist. Reflections from the wall could also be a possible explanation. However, this was considered acceptable for the present preliminary acoustic tests. Further precautions were taken as to conduct the test after normal working hours, so other noise from laboratory work or air conditioning would not disrupt the data.

Next, the domain to obtain far-field data was determined to include all frequencies measured above 540 Hz. The amount of noise contamination was established as a function of the difference between the background noise and the test article noise spectra. In the MIT acoustic chamber, on average, the acoustic data was up to 10 dB above the background noise, which corresponds to at least 0.46 dB of contamination. Thus, the background noise contamination is an issue, so that it has to be subtracted from the acoustic measurements to get the correct sound pressure level magnitude of the noise source under investigation. The subtraction should be done on an absolute basis.

It was found that the peak frequency of the noise due to the wind tunnel free jet does not change with velocity which is agreement with Tam [6]. However, when non-dimensionality the value for the MIT 1 by 1 Low Speed Wind Tunnel facility is higher, 0.27, compared to the data of Tam. This difference might be due to the flow in the duct not the acoustic equipment.

Finally, the desired frequency test range was identified 1-10 kHz. The 1-10 kHz frequency range is free of external noise such as noise due to the electronic equipment, and the background noise has a flat spectrum in this frequency range. Within this fre-

quency range the design of experiments is conducted for the preliminary experiments at MIT.

Preliminary Experiments in the MIT Acoustic Chamber

Chapter 4 gave an overview of the aeroacoustic tests performed of six perforated (porosities from 10% to 60%) and one solid (0% porosity) plates in a spoiler configuration at three different wind tunnel velocities (15, 20 and 30 m/s) in the MIT acoustic chamber.

The important features of the perforated spoilers spectra can be summarized as follows. In the frequency region $0 \leq f \leq 800$ Hz the noise signature due to the wind tunnel jet noise is obtained. The noise signature of the perforated drag plates are below the acoustic chamber background noise. This, combined with the fact that 540 Hz is the lowest usable far field frequency at all microphone locations, the noise spectrum of the perforated plate in the low frequency range cannot be determined or measured directly.

The second frequency range ($800 \leq f \leq 2500$ Hz) is the only one that could be scaled and is important to the full scale noise. It was hypothesized that this noise signature, which does not scale with St_d, should be due to the isotropic turbulence structures and hence has no directivity. A semi-empirical noise prediction tool, described in Chapter 6, was used to predict the noise signature of the perforated plates within the mid-frequency range.

The third frequency region (2.5 kHz $\leq f$) scales with St_d. The distinct peaks identified are above 10 kHz for the full-scale configuration where the velocities are in the range of 60 to 100 m/s. Here the assumption that the full scale perforated drag device has the same perforation diameter is made. This implies that the other length scale, the size of the plate L is not important for the peak frequencies when scaled to full size.

An assessment of the interaction of the MIT acoustic chamber open jet with the perforated plates was conducted. It was observed and concluded that the primary noise source responsible for the observed peaks in the high-frequency range is the

merging of the jetlets. The shear layer interacts with the perforated plate through the top 5 rows, shielding the noise generated by the jetlets merging in the lower rows of perforations.

It was also found that there is a large acoustic shielding effect for mid to high frequencies while at low to mid frequencies, the shielding effect is negligible.

Acoustic Phased Array Experiments

Chapter 5 addresses the sizing and design choice of six perforated and one solid plates. These plates were tested in four different configurations in the CU Markham wind tunnel equipped with acoustic phased array. The results together with a thorough discussion are also included.

The sizing was based on the data available from the perforated plates tested in the MIT acoustic chamber. The two sizes $L_1 = 0.1$ m and $L_2 = 0.2$ m were chosen so that the main spectra features observed in the MIT acoustic chamber tests appear above the background noise in the Markham wind tunnel.

Based on the dimensional analysis done in Chapter 3, perforated plate parameter space was also defined. Six perforated plates were then chosen in the design space so that the design space be fully explored. The choice was made so that all the important non-dimensional parameters were varied.

The tests done in CU Markham wind tunnel were performed in four different test configurations: two spoiler and two drag rudder configurations. A horizontal plate was mounted across the wind tunnel section. The first spoiler configuration was with a spoiler mounted on the bottom surface of the horizontal plate, immediately above the center of the acoustic phase array. The second spoiler configuration, in which the spoiler was on the upper side of the flat plate, was done mainly to estimate the flat plate (wing) shielding effects. The other two configurations, simulated drag rudder configurations. They were tested because it was suggested that for the current SAX10 drag rudders be used.

The analysis of the test results showed there are two peaks, identifiable in all plates and configurations, whose frequencies scale with velocity. Different candidate

length scales were used to collapse the data but a universal characteristic length was not found.

Based on the acoustic phased array tests performed in the Markham wind tunnel at Cambridge University, a recommendation for the Silent Aircraft was made for a potential drag device. The most beneficial for noise design region is where the porosity of the plates is achieved by many small perforations of $d/L = 0.013$ spaced closely by $s/L = 0.0217$. The small distance of the perforations to the plate edge relieves the plate edge and a tone (observed for some spectra) is not produced.

The quietest drag device configuration was also identified. A perforated spoiler mounted on the upper airfoil surface is quieter than a drag rudder configuration because some of the turbulent mixing noise sources are shielded from the ground by the airfoil. This will further reduce the aircraft airframe noise on a 6° flight path.

An attempt was made to scale the spectra of the candidate for a quiet drag device perforated plate 6 for plate size and free stream velocity. In order to scale to full size, a velocity scaling law of the observed peaks is suggested with the caveat that there is peak SPL data. If such a power low indeed exists, then the exponent n will probably be around 4.0. The overall sound pressure levels were found to scale with size, such that an increase in source area causes an equivalent increase in the acoustic power.

Drag Rudder Noise Assessment for SAX10 Design

Two simple models were developed for the bluff-body noise (lower frequencies) and turbulent mixing noise (higher frequencies) created by a perforated drag rudder. These models were then used to predict the full size drag rudder noise signature for the noise and performance audit of SAX10.

Even though the noise levels from the perforated drag rudder are larger than those of the other airframe components, the addition of the perforated drag rudder leads to a 4 dBA reduction in cumulative sound pressure levels because it allows a 6° flight path [5].

7.2 Future Work

The noise assessment of the perforated drag concepts need a refined low frequency model. For this purpose, experiments need to be conducted and experimental data needs to be incorporated into the model. Highly anechoic acoustic chamber tests or hot wire measurement are envisioned to assess low frequency content.

Hot wire tests with a traverse mechanism behind the perforated plates tested in the CU Markham wind tunnel are scheduled and are left for future work.

A full investigation of the true nature of the observed tones and also a better understanding of the noise sources is needed. For this purpose it is proposed that blocking rows or columns (especially the columns nearest to the plate edges) of perforations could provide invaluable information. Due to time constraints, this was not conducted in this study and is also left for future work.

Appendix A

Tables

Table A.1: Peak frequencies for small plates ($L = 0.1$ m) in spoiler configuration 1.

Plate	Peak **A**, Hz			Peak **B**, Hz		
	20 m/s	30 m/s	40 m/s	20 m/s	30 m/s	40 m/s
Perforated Plate 1	6000	8096	12459	9345	12459	15748
Perforated Plate 2	3218	5000	6421	7774	10873	13482
Perforated Plate 3	5000	8292	12459	9920	15450	20240
Perforated Plate 4	5863	8000	12400	11765	0	0
Perforated Plate 5	6687	10415	12700	9920	15748	19668
Perforated Plate 6	7236	11243	14381	9367	12761	15748

Peak **C**, Hz			Peak **D**, Hz			Peak **T**, Hz		
20 m/s	30 m/s	40 m/s	20 m/s	30 m/s	40 m/s	20 m/s	30 m/s	40 m/s
12400	14658	0	15937	18176	0	19021	19621	19528
10873	16519	0	15487	0	0	19296	17328	21080
13322	0	0	16758	0	0	21080	21080	20240
15748	15748	15748	18840	19204	19158	21745	23084	23530
13070	0	0	16838	0	0	19528	20484	19668
12519	15748	0	15748	0	0	0	0	0

Table A.2: Peak magnitudes for small plates ($L = 0.1$ m) in spoiler configuration 1.

Plate	Peak **A**, dB			Peak **B**, dB		
	20 m/s	30 m/s	40 m/s	20 m/s	30 m/s	40 m/s
Perforated Plate 1	25.00	30.55	33.67	29.88	25.28	30.00
Perforated Plate 2	40.43	48.30	53.73	35.87	41.23	48.60
Perforated Plate 3	31.70	39.70	45.47	31.40	37.79	69.87
Perforated Plate 4	25.74	30.00	33.67	23.32	0	0
Perforated Plate 5	28.30	32.55	36.93	34.17	32.98	58.07
Perforated Plate 6	22.55	27.57	33.33	22.21	28.30	34.80

Peak **C**, dB			Peak **D**, dB			Peak **T**, dB		
20 m/s	30 m/s	40 m/s	20 m/s	30 m/s	40 m/s	20 m/s	30 m/s	40 m/s
18.72	25.29	0	12.17	25.11	0	9.57	29.87	40.33
33.19	42.77	0	30.00	0	0	30.85	77.00	55.33
32.13	0	0	30.00	0	0	27.45	64.34	69.87
16.21	27.23	33.27	14.55	26.89	34.00	7.66	36.80	37.20
27.45	0	0	24.21	0	0	17.02	44.68	58.07
22.55	33.32	0	25.53	0	0	0	0	0

Table A.3: Peak frequencies for large plates ($L = 0.2$ m) in spoiler configuration 1.

Plate	Peak **A**, Hz			Peak **B**, Hz		
	20 m/s	30 m/s	40 m/s	20 m/s	30 m/s	40 m/s
Perforated Plate 1	5976	8636	12021	8174	13007	14075
Perforated Plate 2	3706	5445	6600	6931	9873	13007
Perforated Plate 3	3226	4454	6150	7447	9896	12700
Perforated Plate 4	6375	9920	12700	9457	14484	18616
Perforated Plate 5	3210	4843	6150	6375	9686	13070
Perforated Plate 6	4216	6150	7411	8000	10847	13007

Peak **C**, Hz			Peak **D**, Hz			Peak **T**, Hz		
20 m/s	30 m/s	40 m/s	20 m/s	30 m/s	40 m/s	20 m/s	30 m/s	40 m/s
11821	17000	15748	0	0	0	0	0	0
10616	15748	15524	14312	20484	20000	9896	0	0
10769	15561	0	15085	0	0	15937	16519	12700
11850	0	0	15748	0	0	18220	18395	18616
9457	15303	18483	12400	19112	0	15748	13579	13070
13974	15561	15561	17122	0	0	20484	21641	21232

Table A.4: Peak magnitudes for large plates ($L = 0.2$ m) in spoiler configuration 1.

Plate	Peak **A**, dB			Peak **B**, dB		
	20 m/s	30 m/s	40 m/s	20 m/s	30 m/s	40 m/s
Perforated Plate 1	34.34	31.74	34.87	35.49	38.00	30.00
Perforated Plate 2	40.85	45.32	52.00	40.00	47.87	41.00
Perforated Plate 3	42.77	52.51	59.67	42.98	48.72	101.00
Perforated Plate 4	30.85	36.77	34.07	30.47	28.94	50.73
Perforated Plate 5	41.06	41.62	47.47	41.91	43.45	59.133
Perforated Plate 6	31.49	39.15	44.73	34.25	39.28	45.33

Peak **C**, dB			Peak **D**, dB			Peak **T**, dB		
20 m/s	30 m/s	40 m/s	20 m/s	30 m/s	40 m/s	20 m/s	30 m/s	40 m/s
20.47	24.26	30.00	0	0	0	0	0	0
33.83	35.32	38.33	25.96	31.70	35.93	66.38	0	0
38.60	37.87	0	33.62	0	0	46.30	52.12	101.00
18.51	0	0	16.04	0	0	10.42	40.00	50.737
42.21	42.59	31.33	25.96	41.06	0	12.89	48.85	59.133
37.87	39.28	44.07	38.94	0	0	23.06	34.89	45.47

Appendix B

Acoustic Phased Array Noise Spectra

B.1 Perforated Plate 1

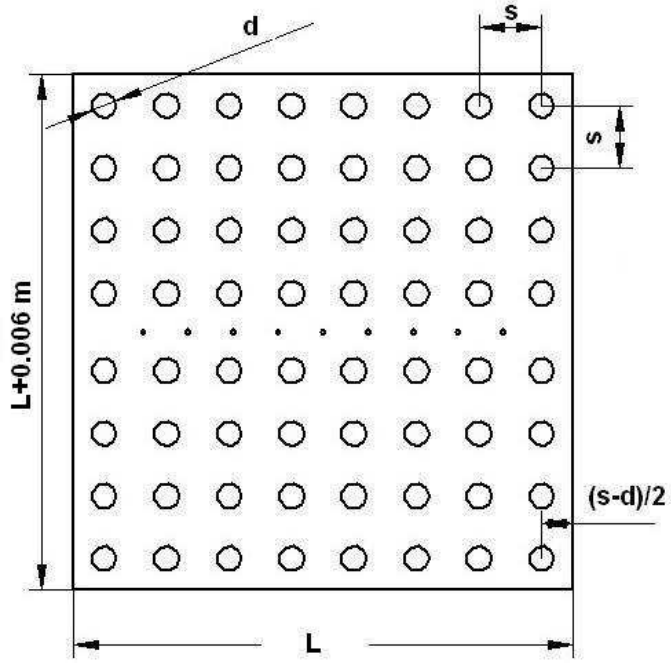

Figure B-1: Perforated plate 1 used in drag rudder configuration 1. $d/L = 0.050$, $s/L = 0.1250$ and $\beta = 0.1257$.

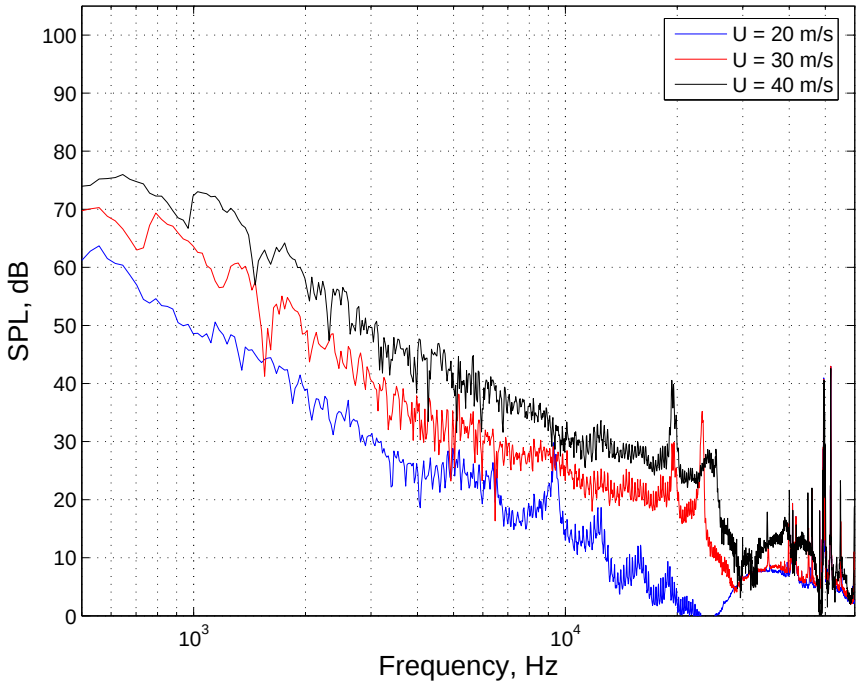

Figure B-2: Perforated plate 1 with $L = 0.1$ m in spoiler configuration 1.

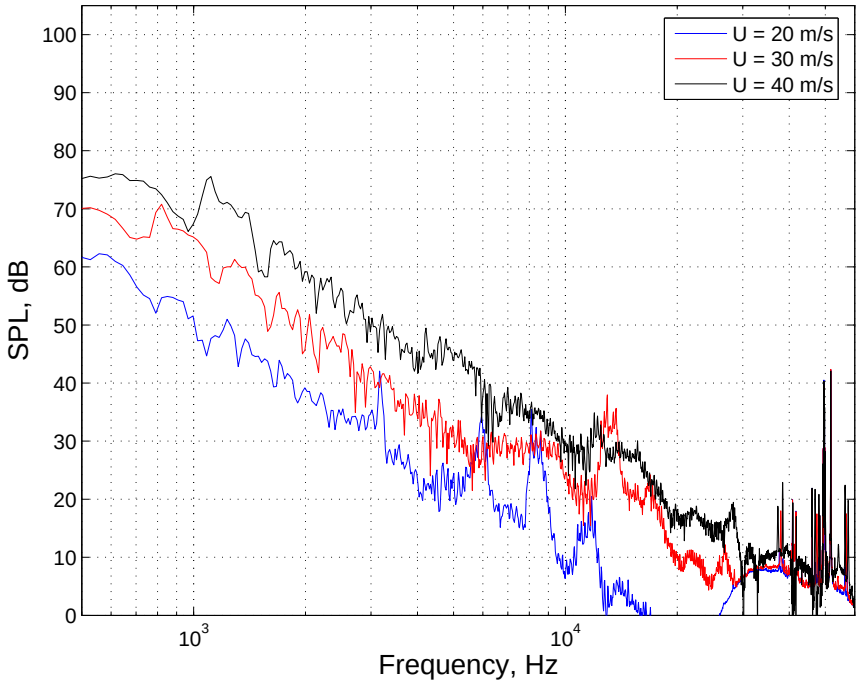

Figure B-3: Perforated plate 1 with $L = 0.2$ m in spoiler configuration 1.

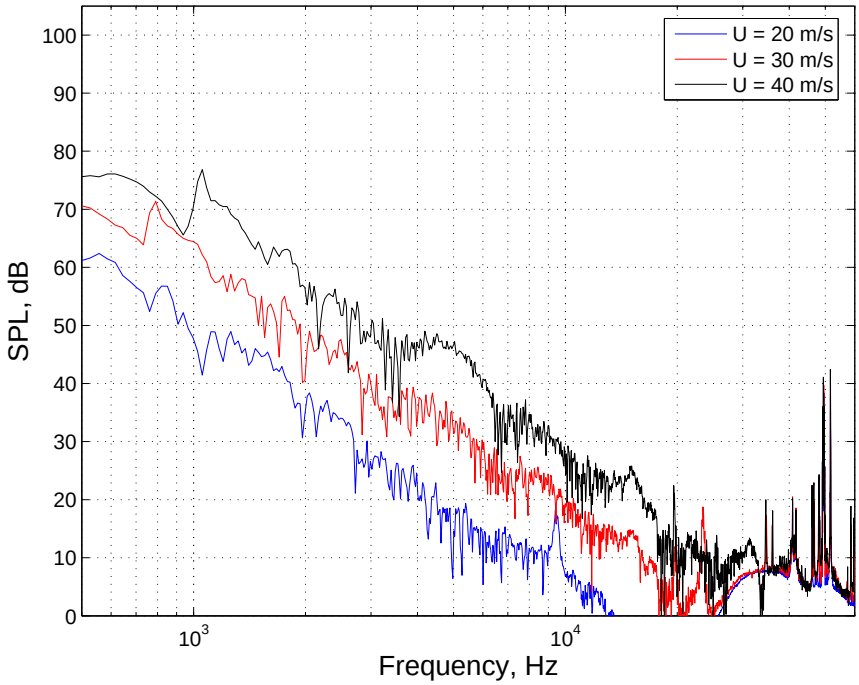

Figure B-4: Perforated plate 1 with $L = 0.1$ m in spoiler configuration 2.

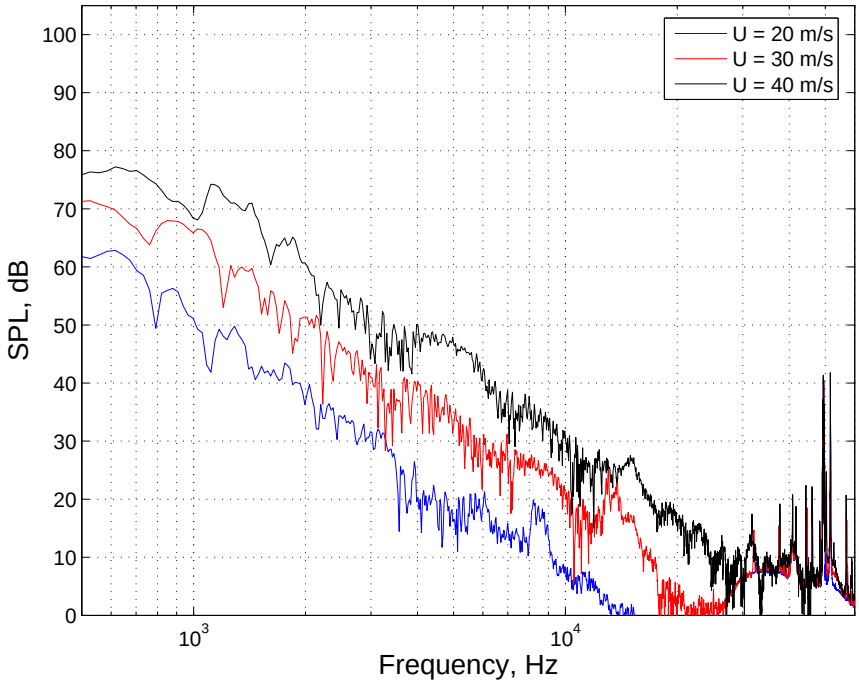

Figure B-5: Perforated plate 1 with $L = 0.2$ m in spoiler configuration 2.

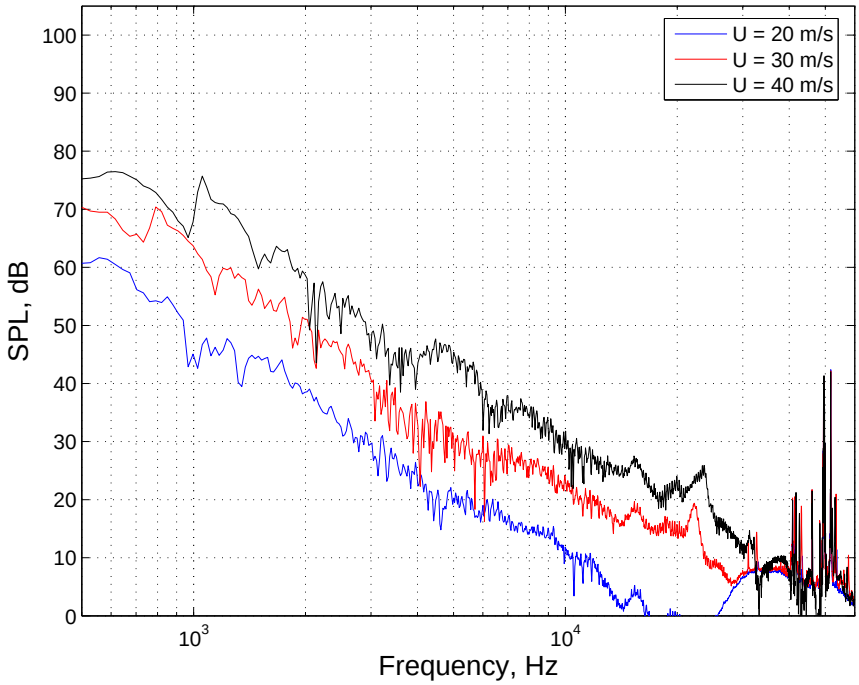

Figure B-6: Perforated plate 1 with $L = 0.1$ m in drag rudder configuration 1.

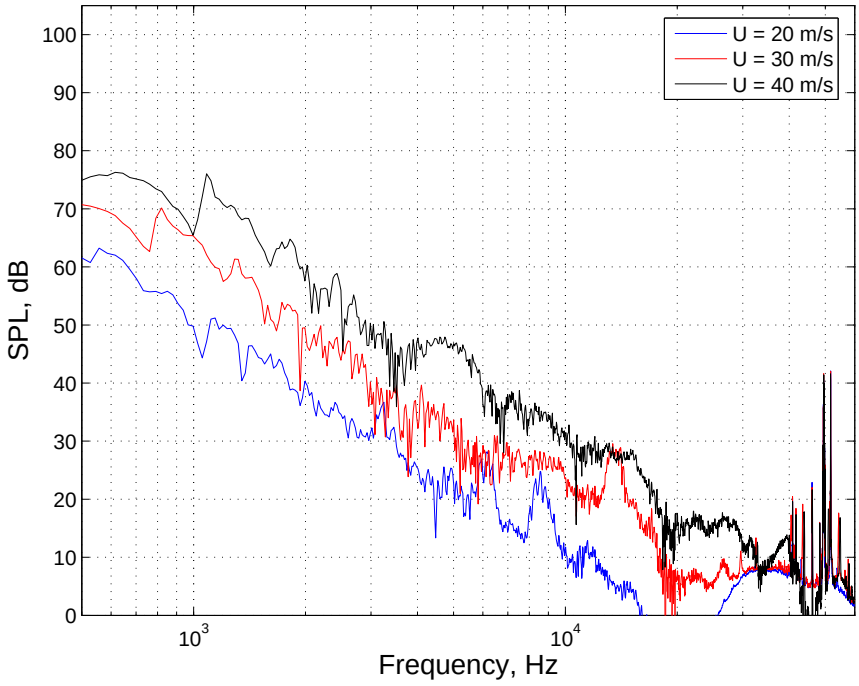

Figure B-7: Perforated plate 1 with $L = 0.2$ m in drag rudder configuration 1.

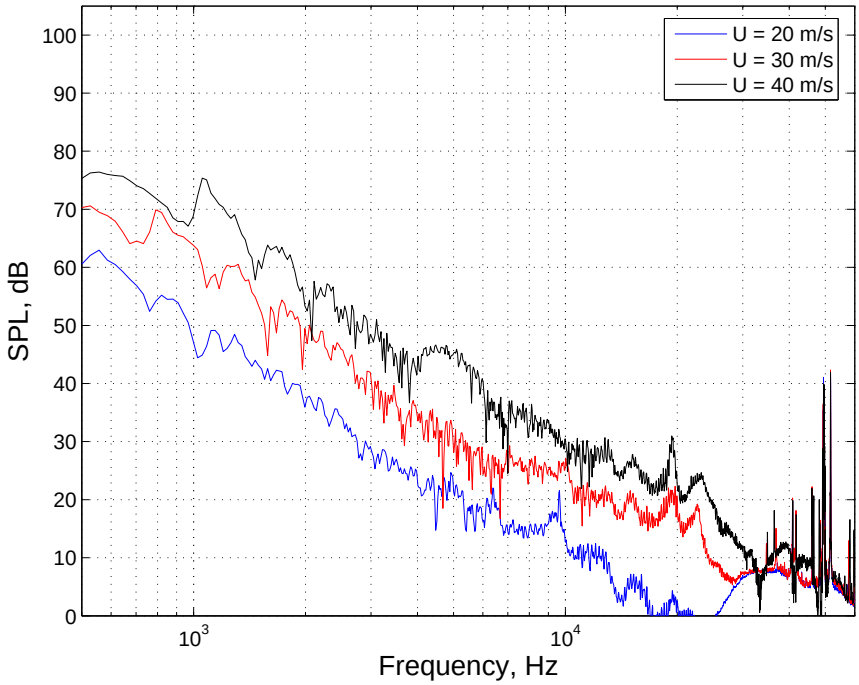

Figure B-8: Perforated plate 1 with $L = 0.1$ m in drag rudder configuration 2.

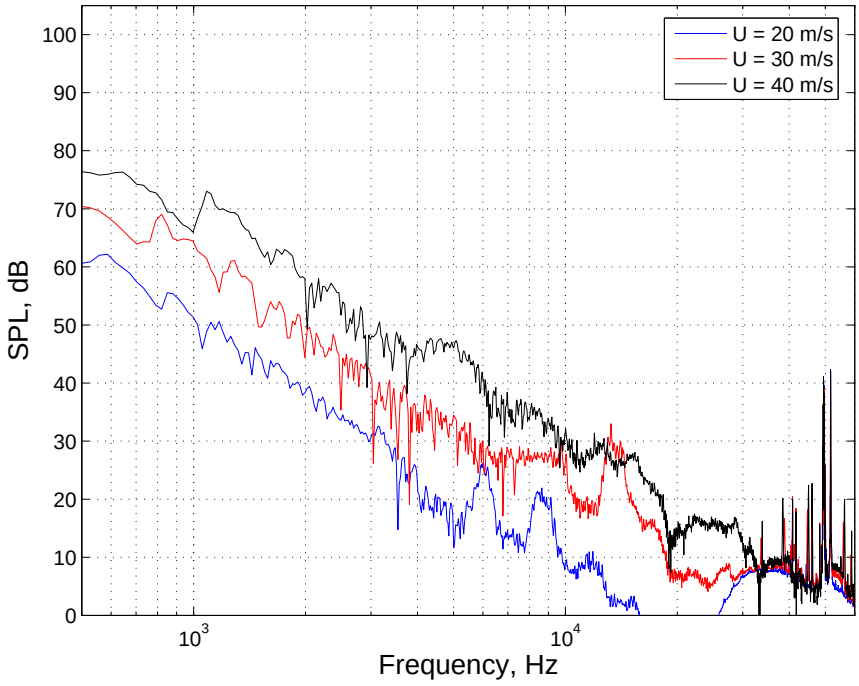

Figure B-9: Perforated plate 1 with $L = 0.2$ m in drag rudder configuration 2.

B.2 Perforated Plate 2

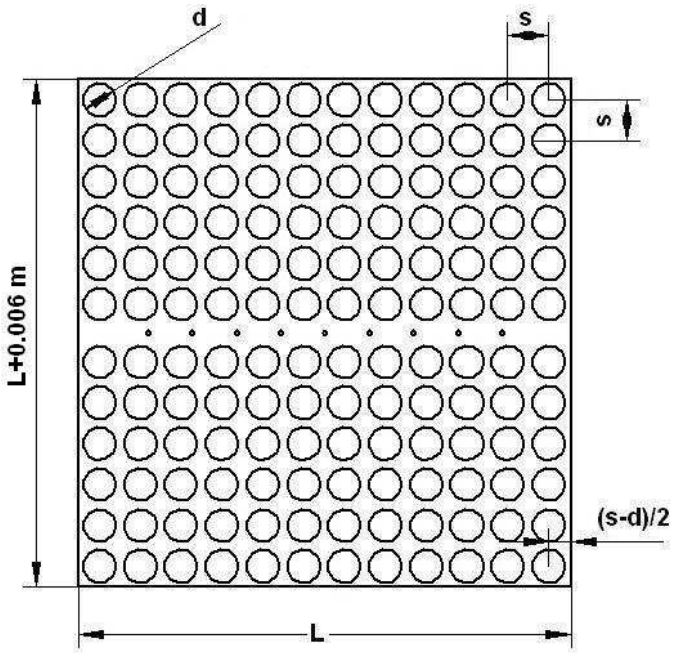

Figure B-10: Perforated plate 2 used in drag rudder configuration 1. $d/L = 0.067$, $s/L = 0.0830$ and $\beta = 0.5118$.

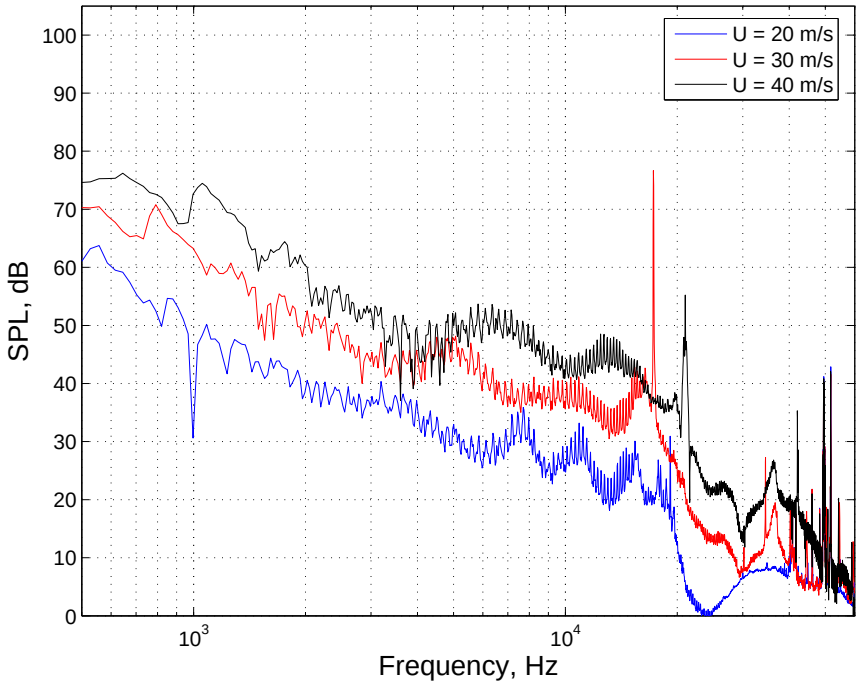

Figure B-11: Perforated plate 2 with $L = 0.1$ m in spoiler configuration 1.

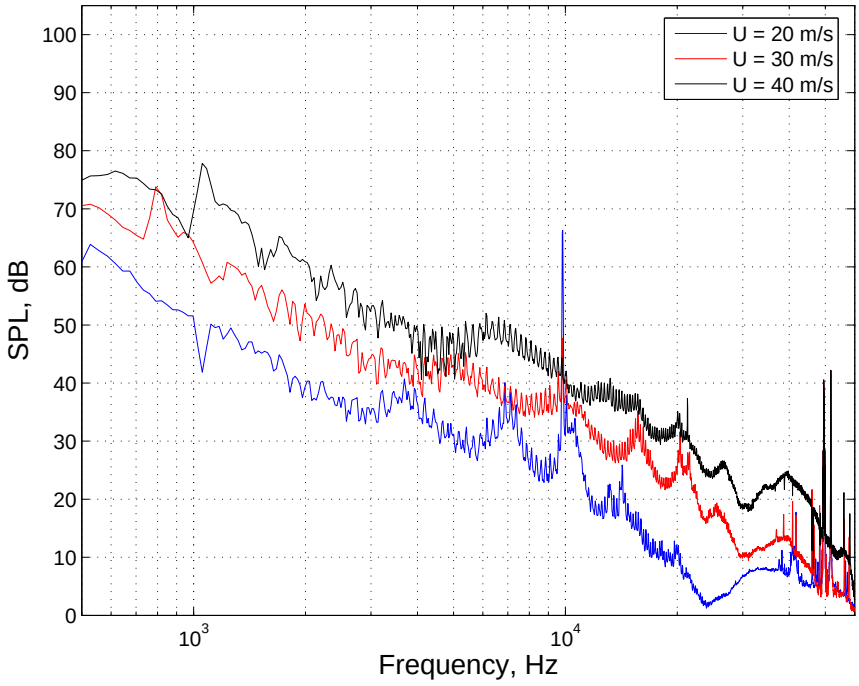

Figure B-12: Perforated plate 2 with $L = 0.2$ m in spoiler configuration 1.

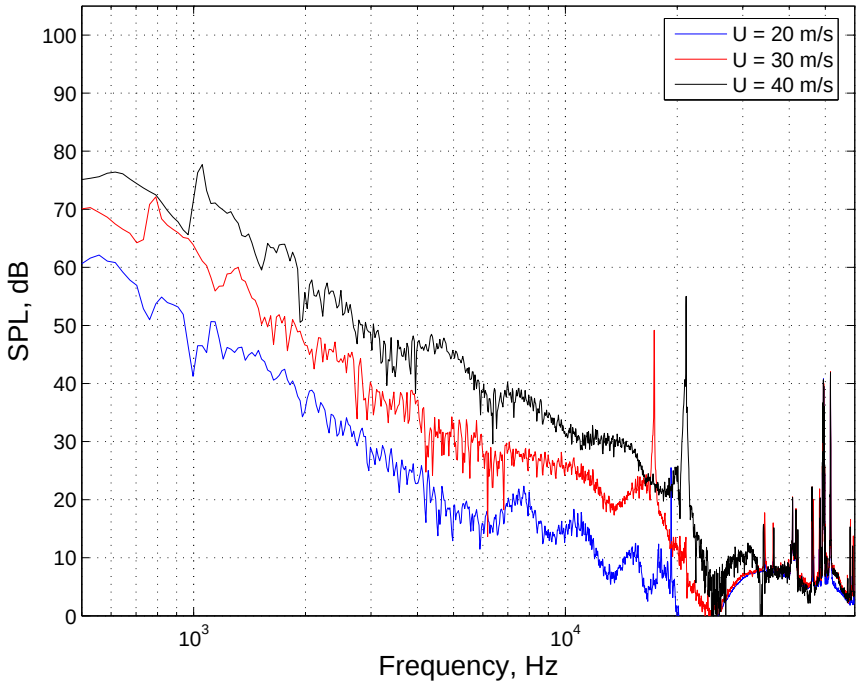

Figure B-13: Perforated plate 2 with $L = 0.1$ m in spoiler configuration 2.

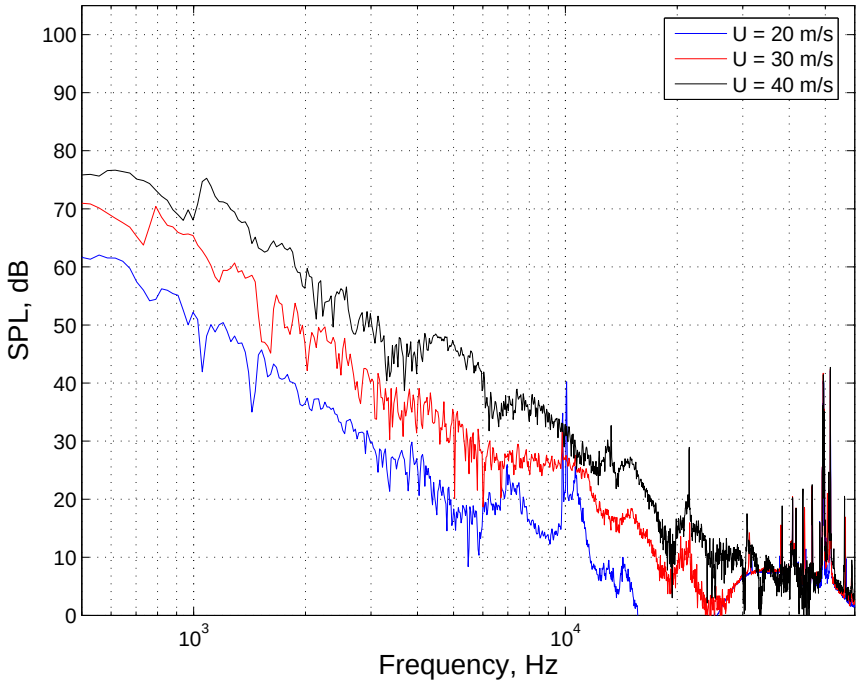

Figure B-14: Perforated plate 2 with $L = 0.2$ m in spoiler configuration 2.

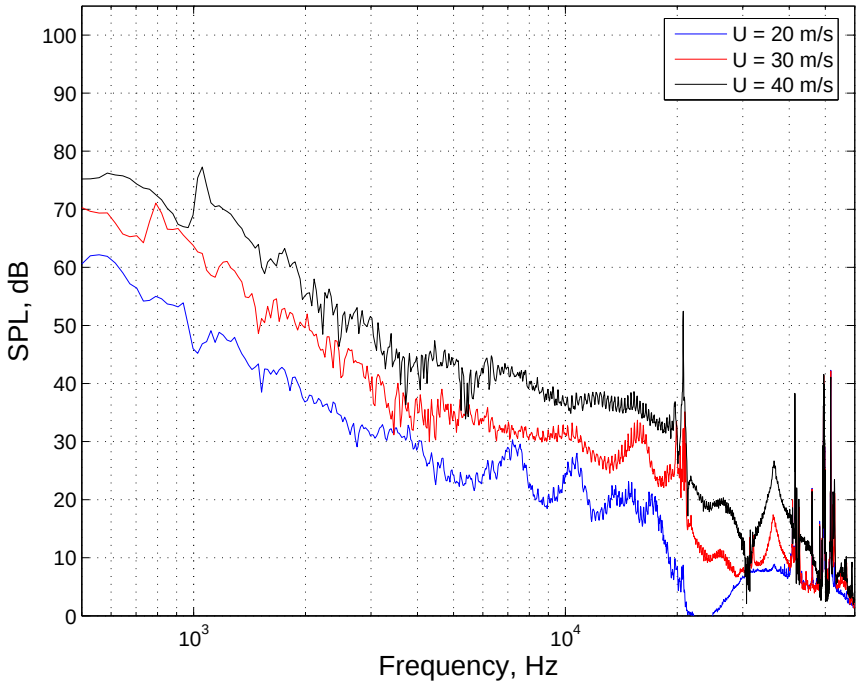

Figure B-15: Perforated plate 2 with $L = 0.1$ m in drag rudder configuration 1.

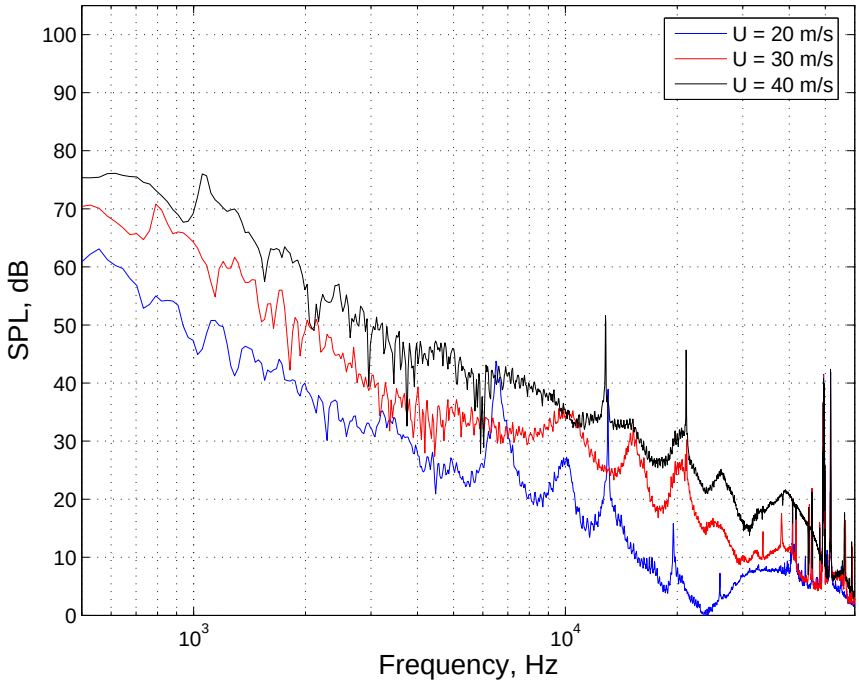

Figure B-16: Perforated plate 2 with $L = 0.2$ m in drag rudder configuration 1.

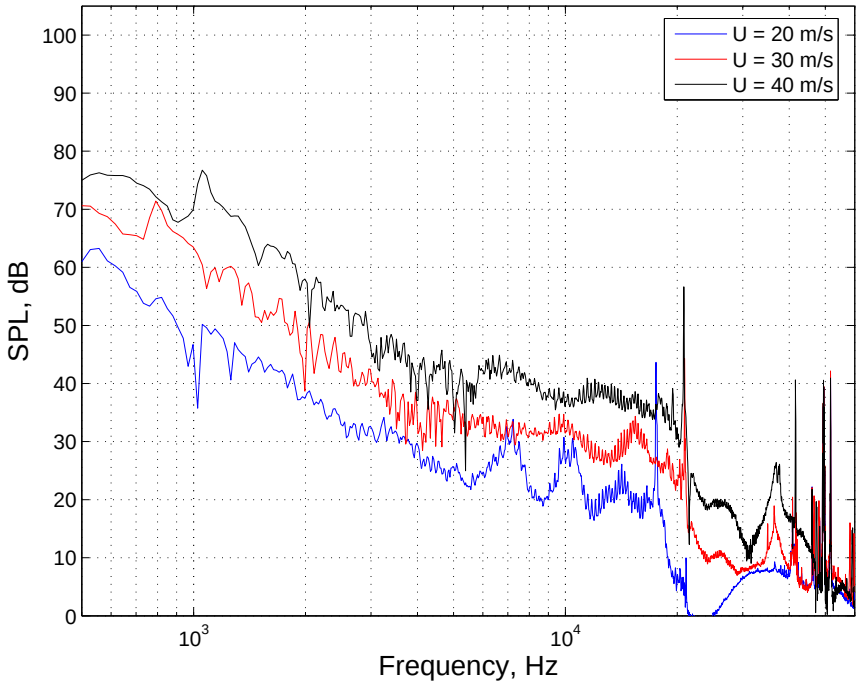

Figure B-17: Perforated plate 2 with $L = 0.1$ m in drag rudder configuration 2.

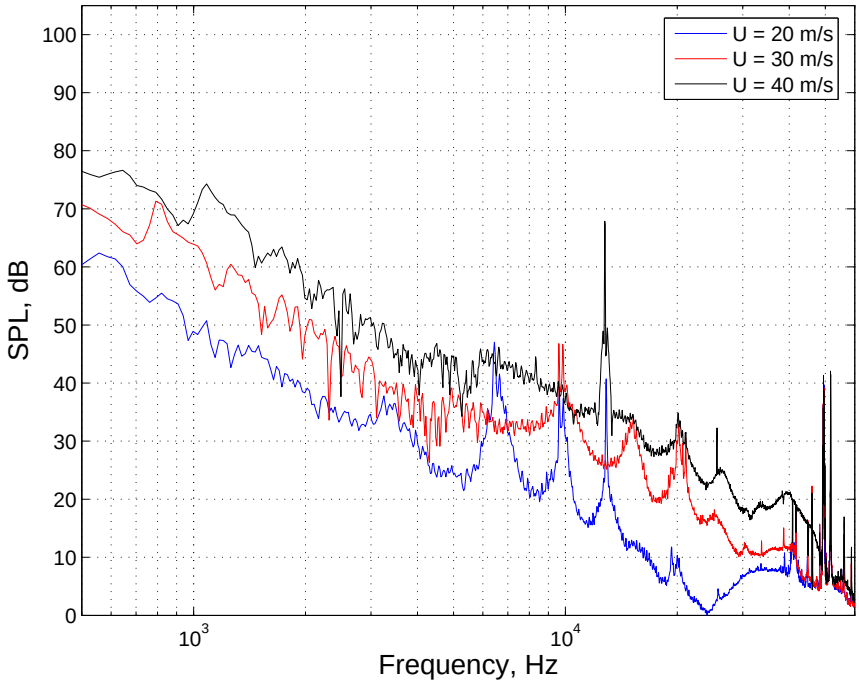

Figure B-18: Perforated plate 2 with $L = 0.2$ m in drag rudder configuration 2.

B.3 Perforated Plate 3

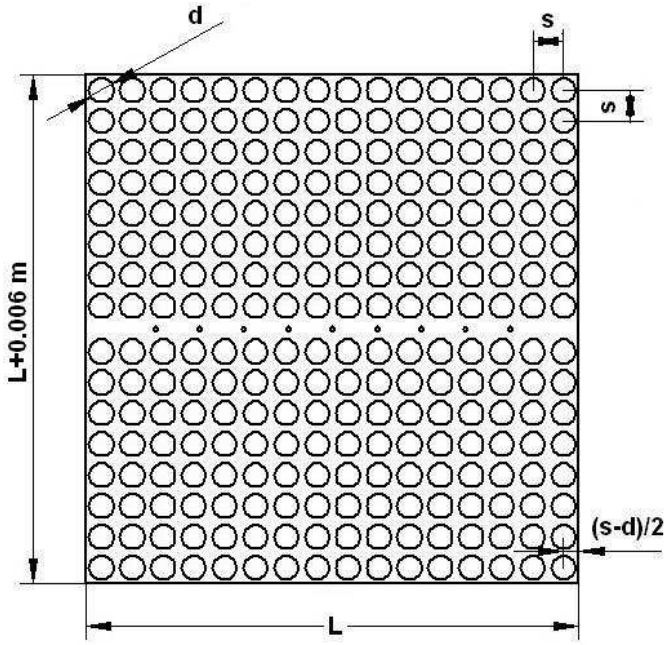

Figure B-19: Perforated plate 3 used in drag rudder configuration 1. $d/L = 0.050$, $s/L = 0.0625$ and $\beta = 0.5027$.

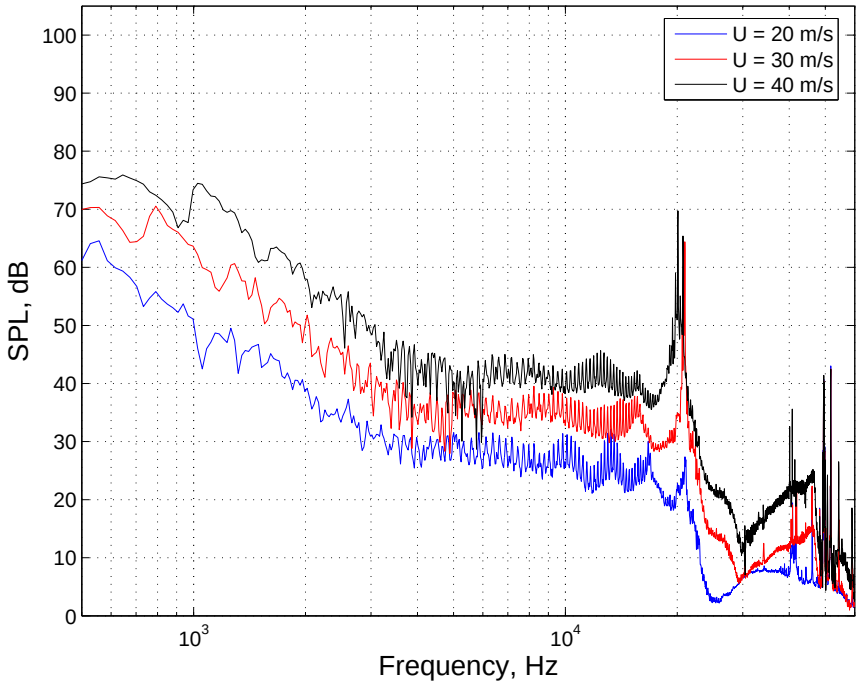

Figure B-20: Perforated plate 3 with $L = 0.1$ m in spoiler configuration 1.

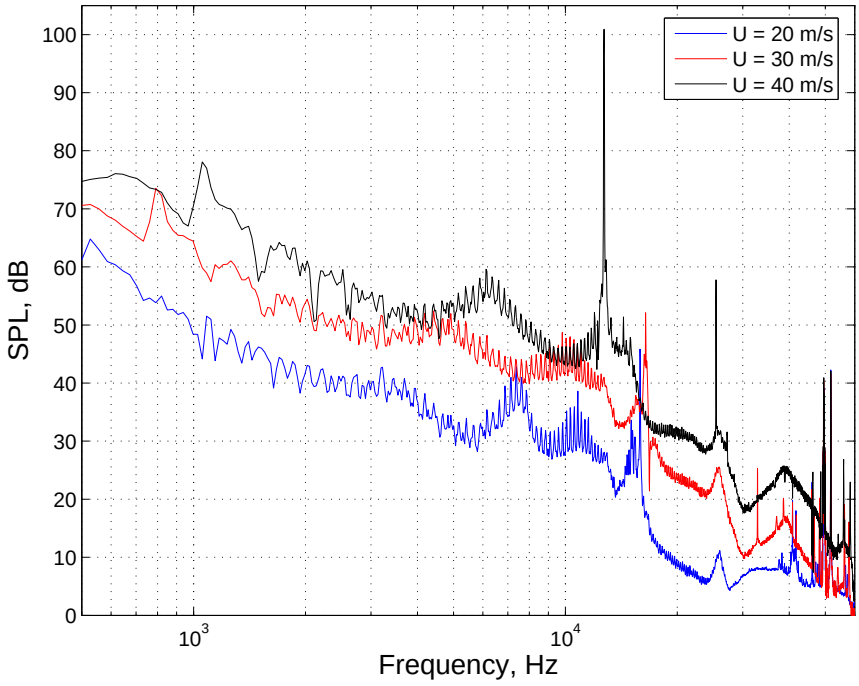

Figure B-21: Perforated plate 3 with $L = 0.2$ m in spoiler configuration 1.

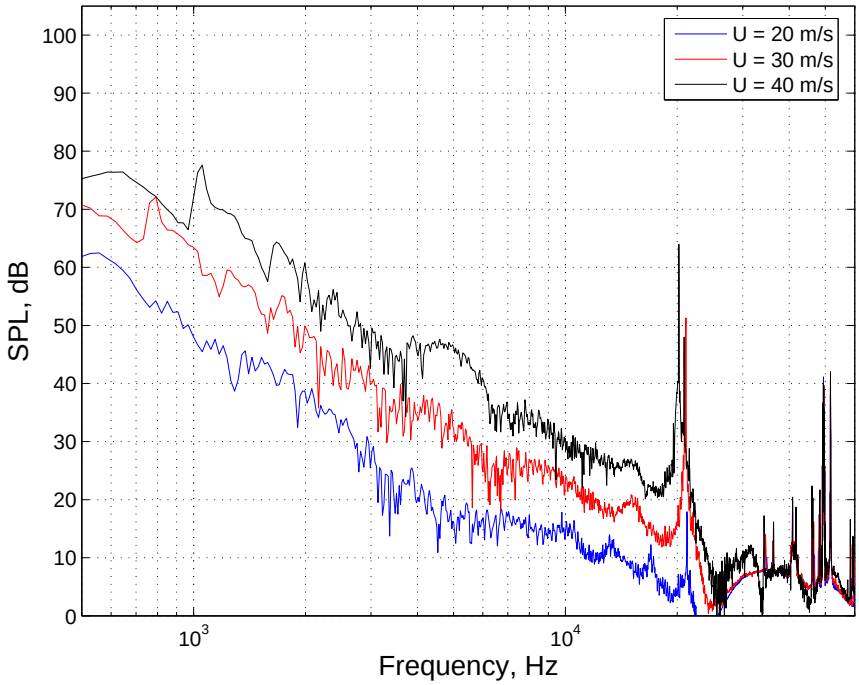

Figure B-22: Perforated plate 3 with $L = 0.1$ m in spoiler configuration 2.

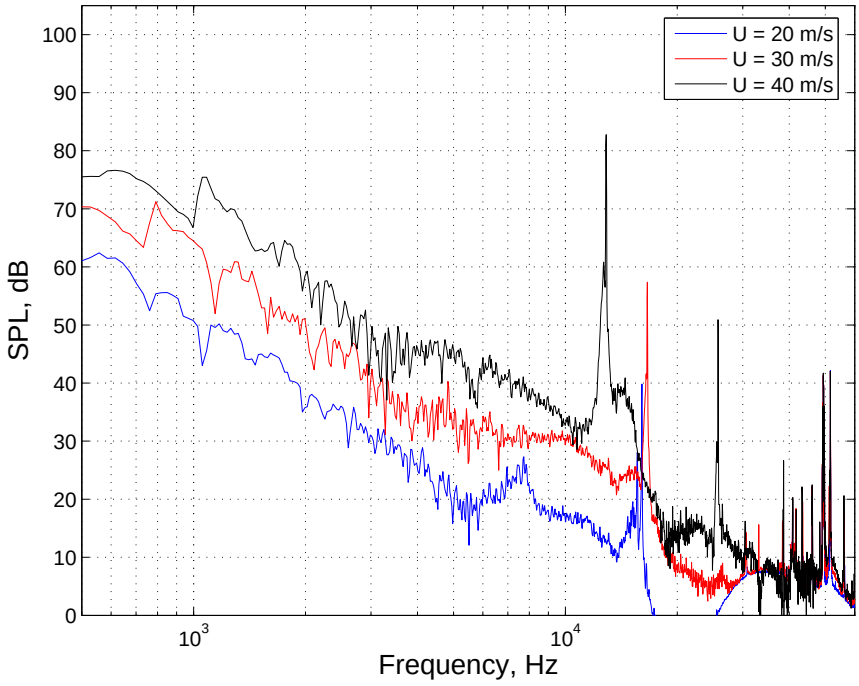

Figure B-23: Perforated plate 3 with $L = 0.2$ m in spoiler configuration 2.

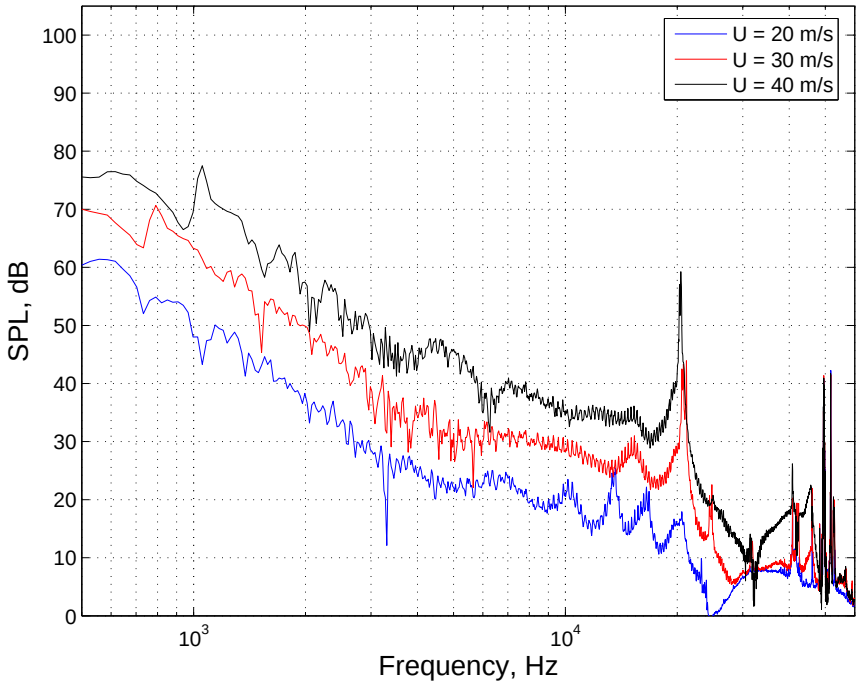

Figure B-24: Perforated plate 3 with $L = 0.1$ m in drag rudder configuration 1.

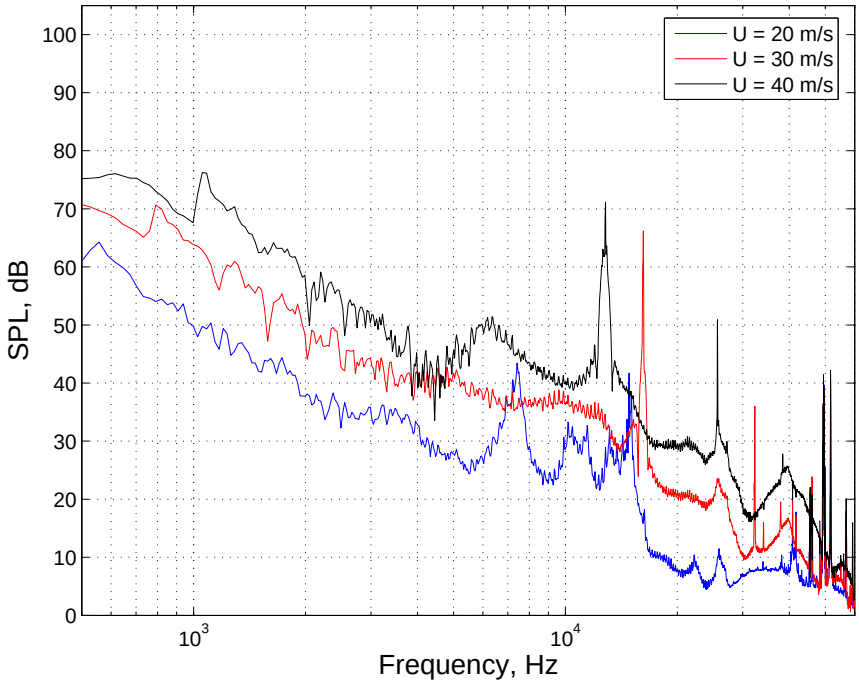

Figure B-25: Perforated plate 3 with $L = 0.2$ m in drag rudder configuration 1.

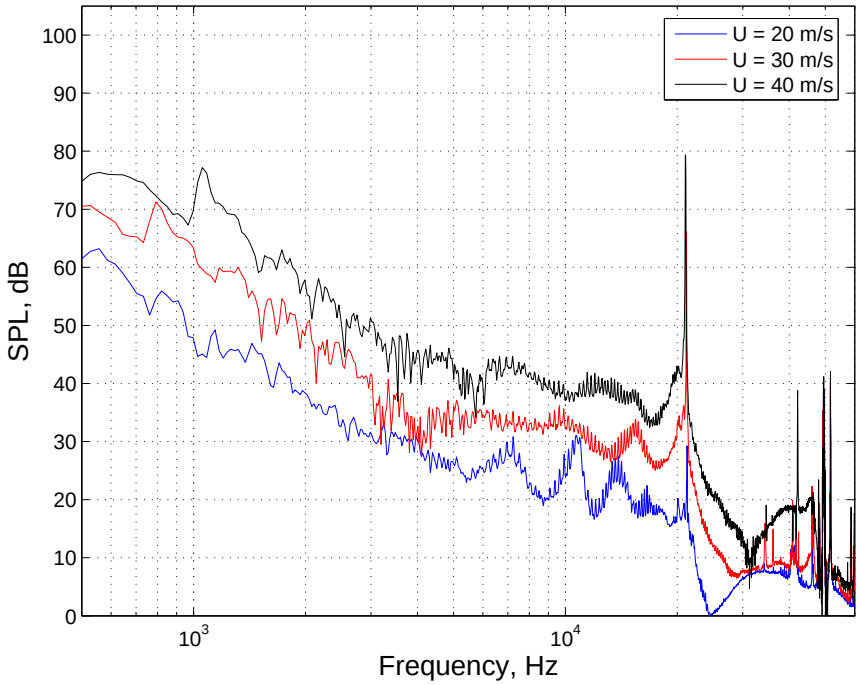

Figure B-26: Perforated plate 3 with $L = 0.1$ m in drag rudder configuration 2.

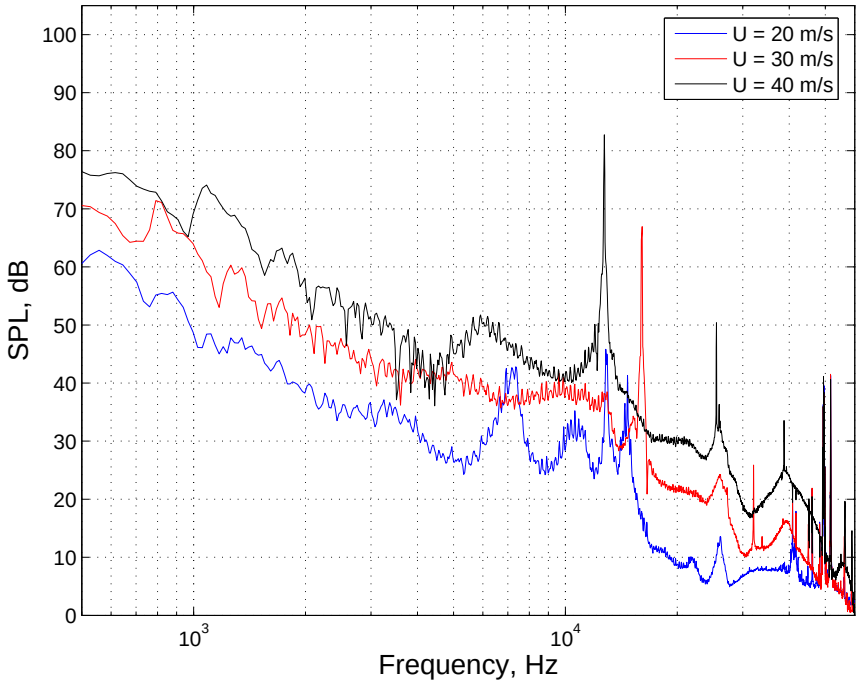

Figure B-27: Perforated plate 3 with $L = 0.2$ m in drag rudder configuration 2.

B.4 Perforated Plate 4

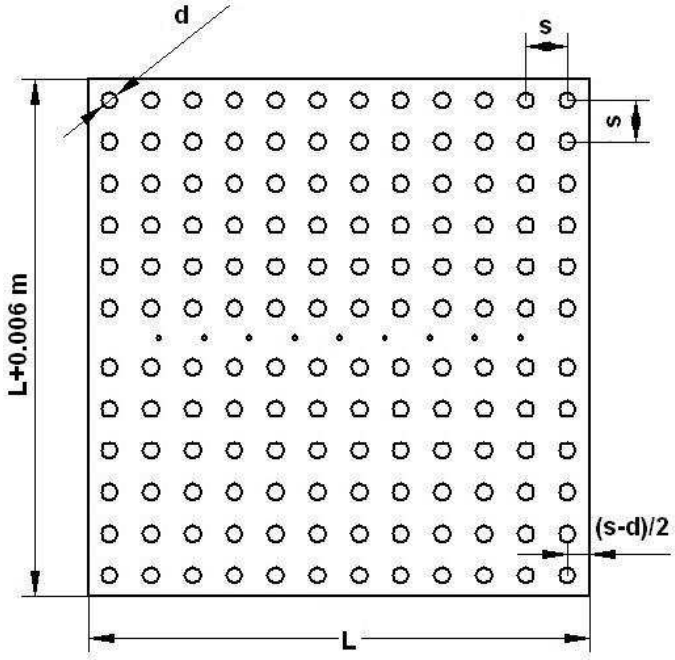

Figure B-28: Perforated plate 4 used in drag rudder configuration 1. $d/L = 0.033$, $s/L = 0.0830$ and $\beta = 0.1242$.

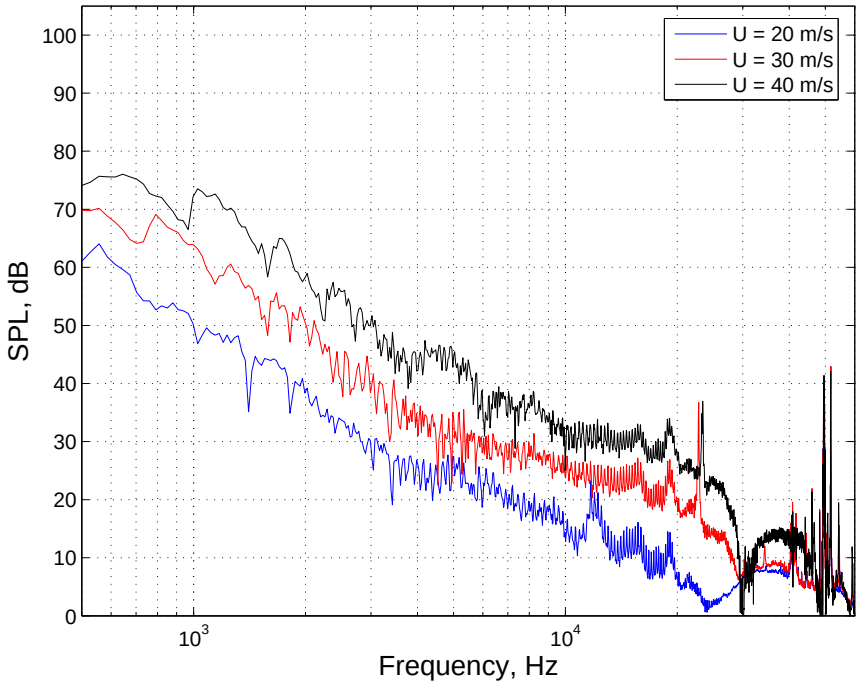

Figure B-29: Perforated plate 4 with $L = 0.1$ m in spoiler configuration 1.

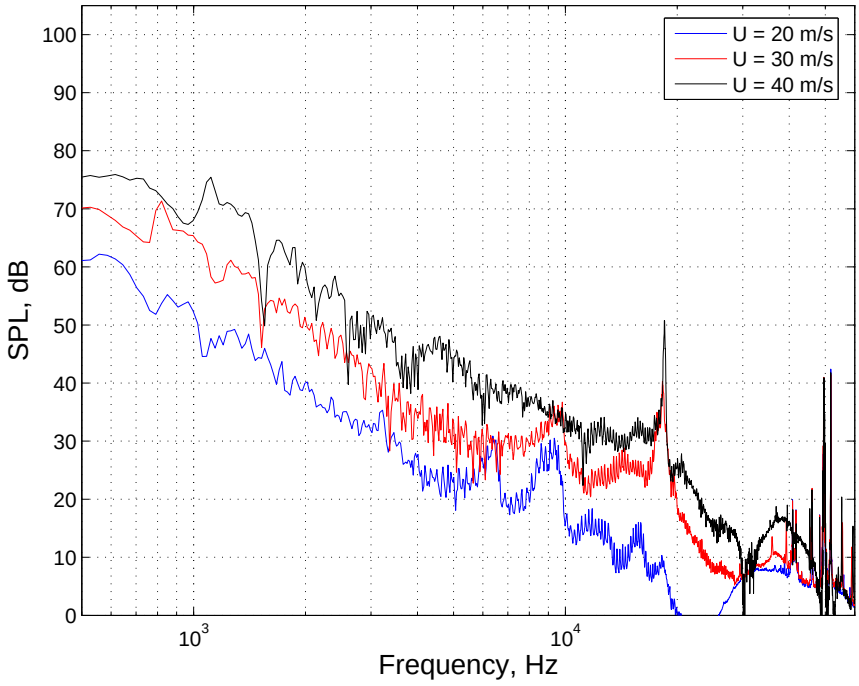

Figure B-30: Perforated plate 4 with $L = 0.2$ m in spoiler configuration 1.

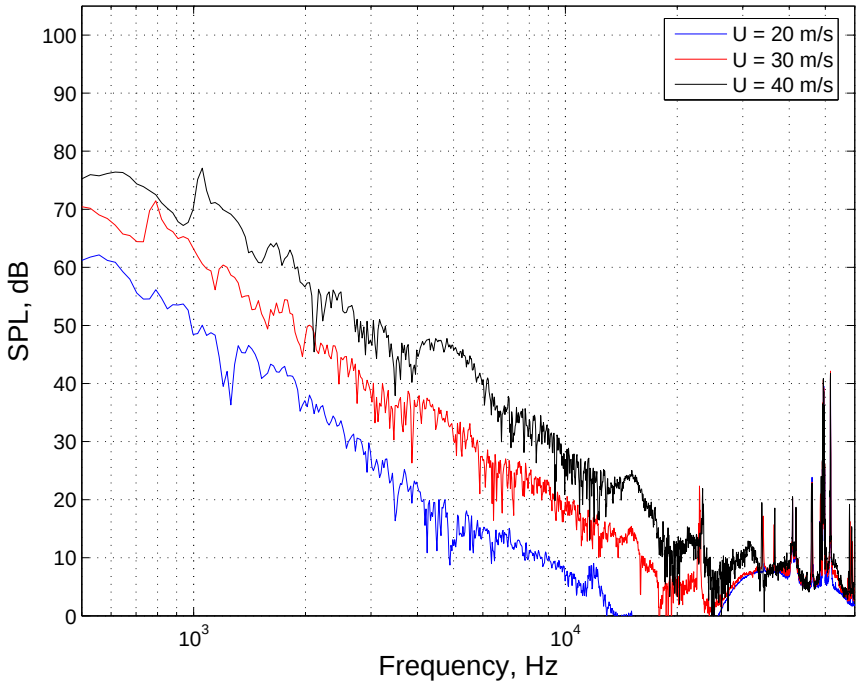

Figure B-31: Perforated plate 4 with $L = 0.1$ m in spoiler configuration 2.

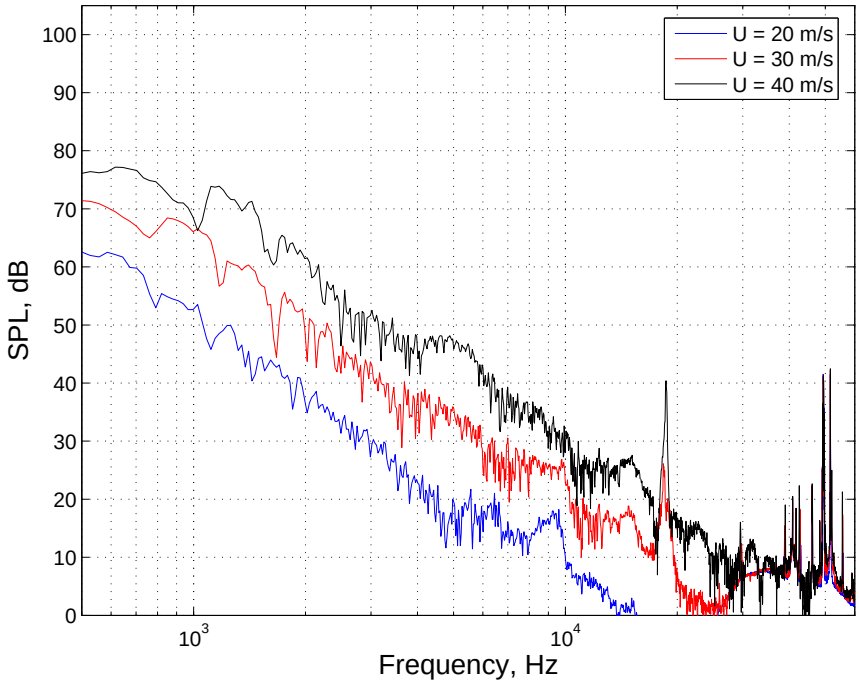

Figure B-32: Perforated plate 4 with $L = 0.2$ m in spoiler configuration 2.

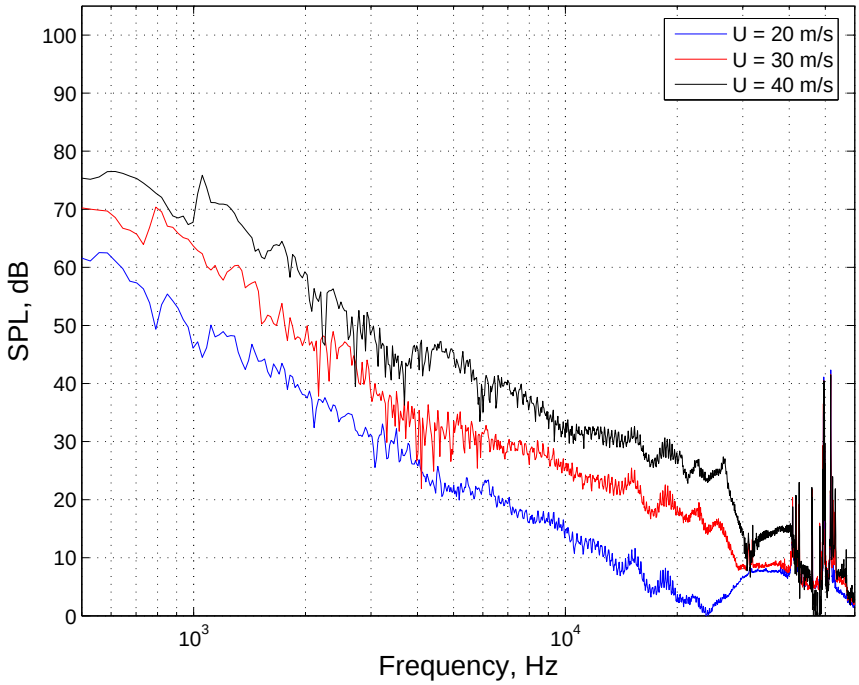

Figure B-33: Perforated plate 4 with $L = 0.1$ m in drag rudder configuration 1.

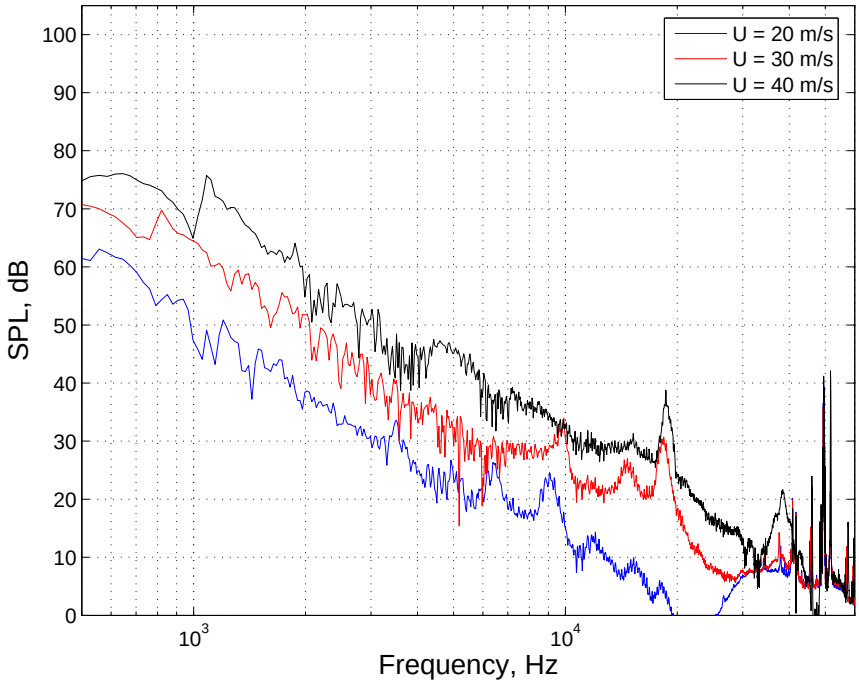

Figure B-34: Perforated plate 4 with $L = 0.2$ m in drag rudder configuration 1.

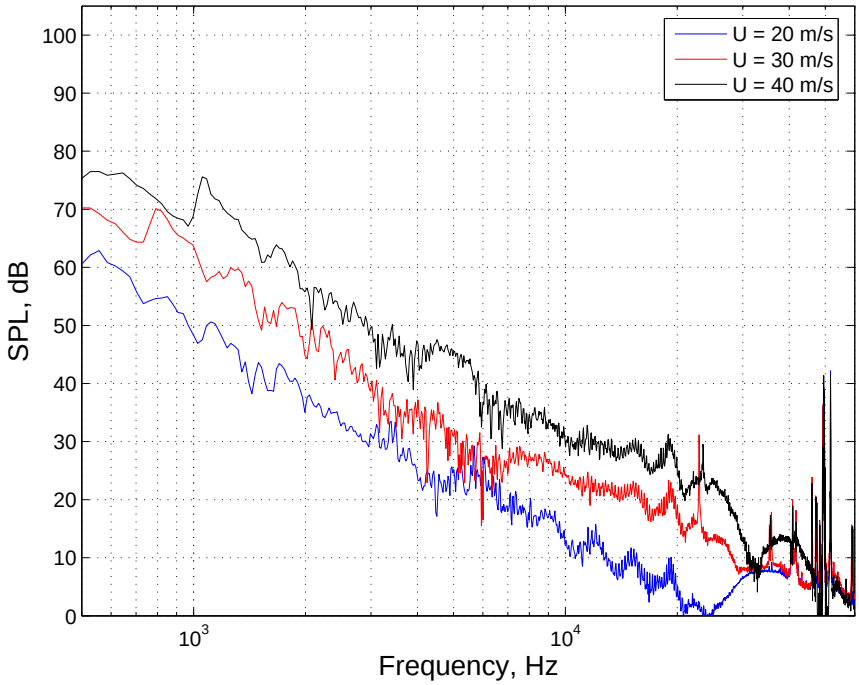

Figure B-35: Perforated plate 4 with $L = 0.1$ m in drag rudder configuration 2.

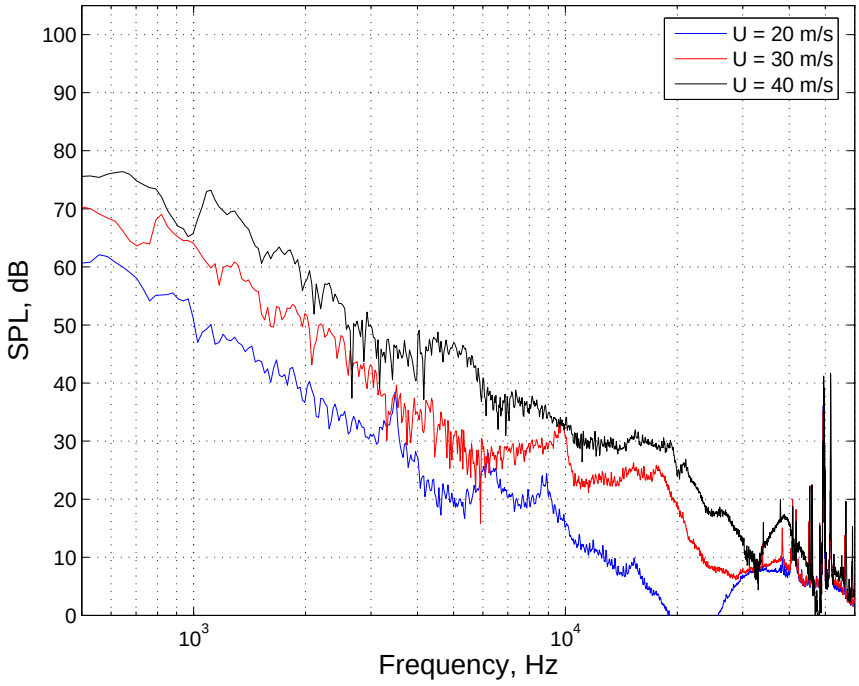

Figure B-36: Perforated plate 4 with $L = 0.2$ m in drag rudder configuration 2.

B.5 Perforated Plate 5

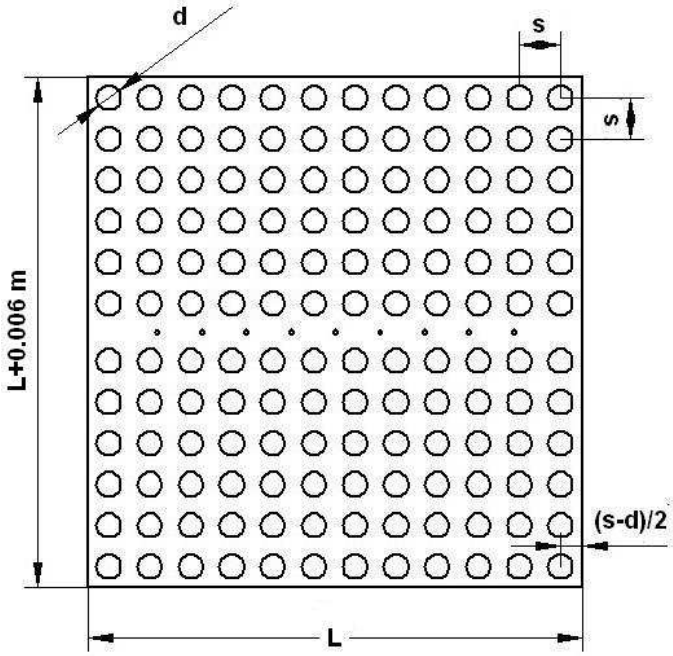

Figure B-37: Perforated plate 5 used in drag rudder configuration 1. $d/L = 0.050$, $s/L = 0.0830$ and $\beta = 0.2850$.

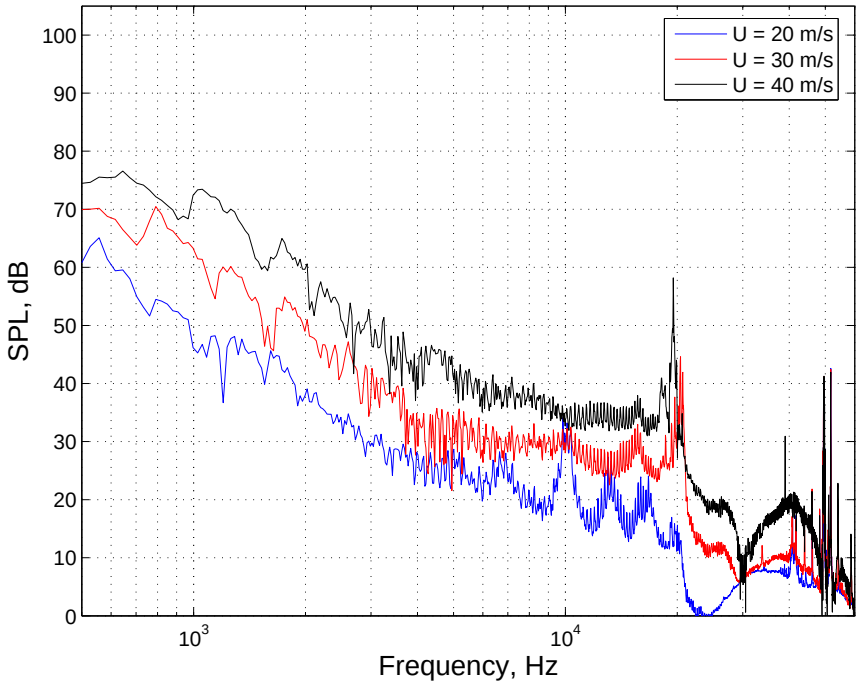

Figure B-38: Perforated plate 5 with $L = 0.1$ m in spoiler configuration 1.

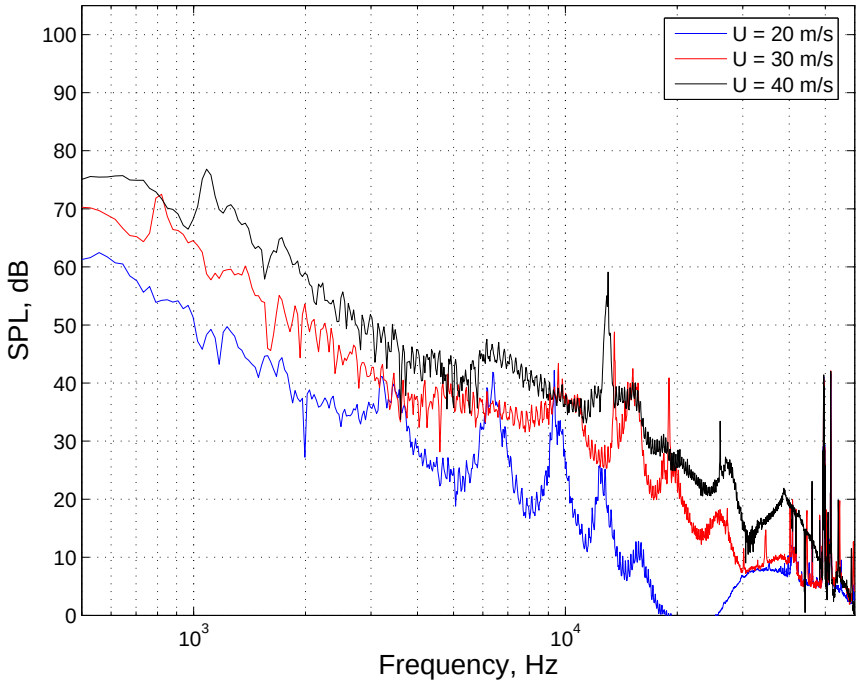

Figure B-39: Perforated plate 5 with $L = 0.2$ m in spoiler configuration 1.

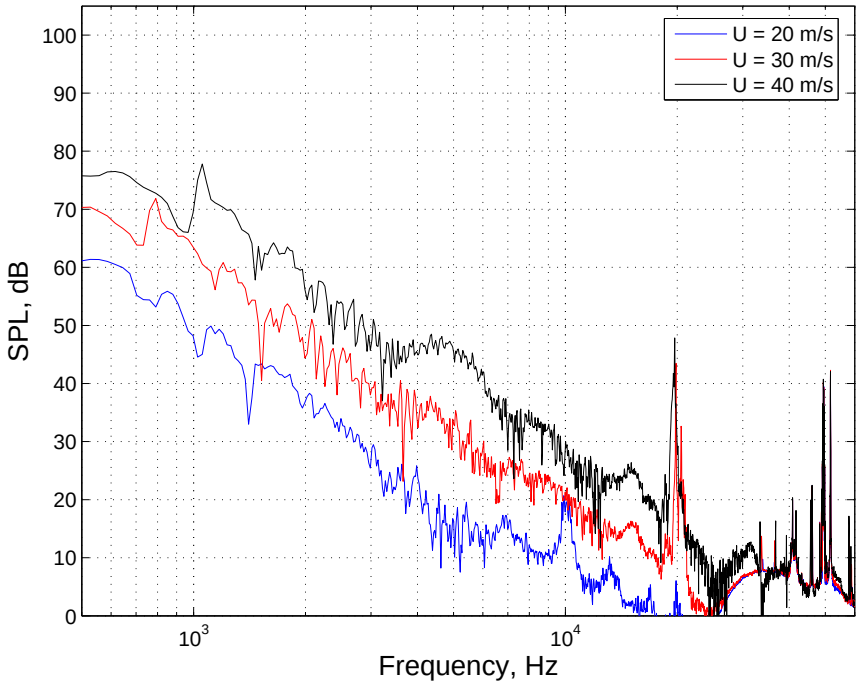

Figure B-40: Perforated plate 5 with $L = 0.1$ m in spoiler configuration 2.

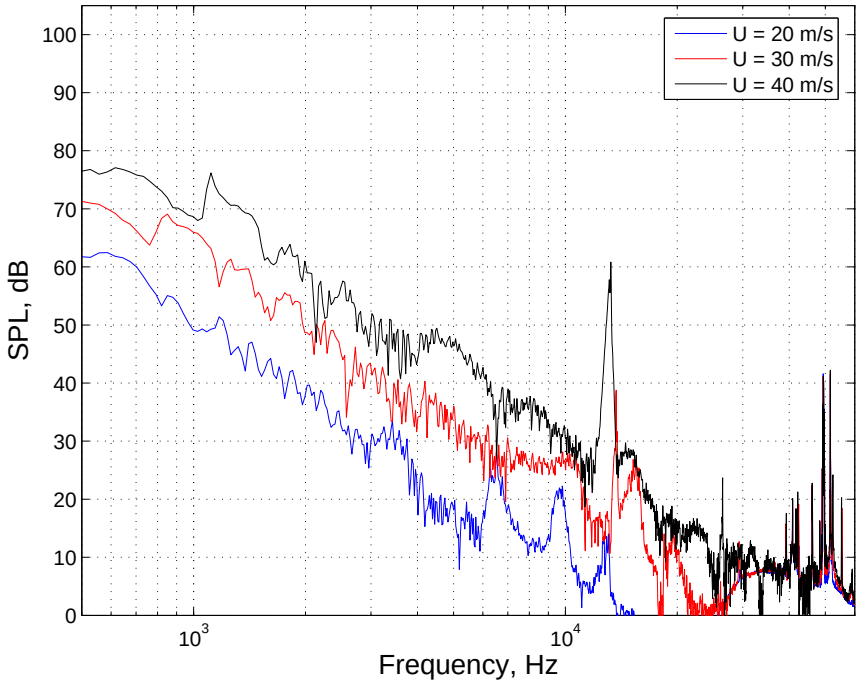

Figure B-41: Perforated plate 5 with $L = 0.2$ m in spoiler configuration 2.

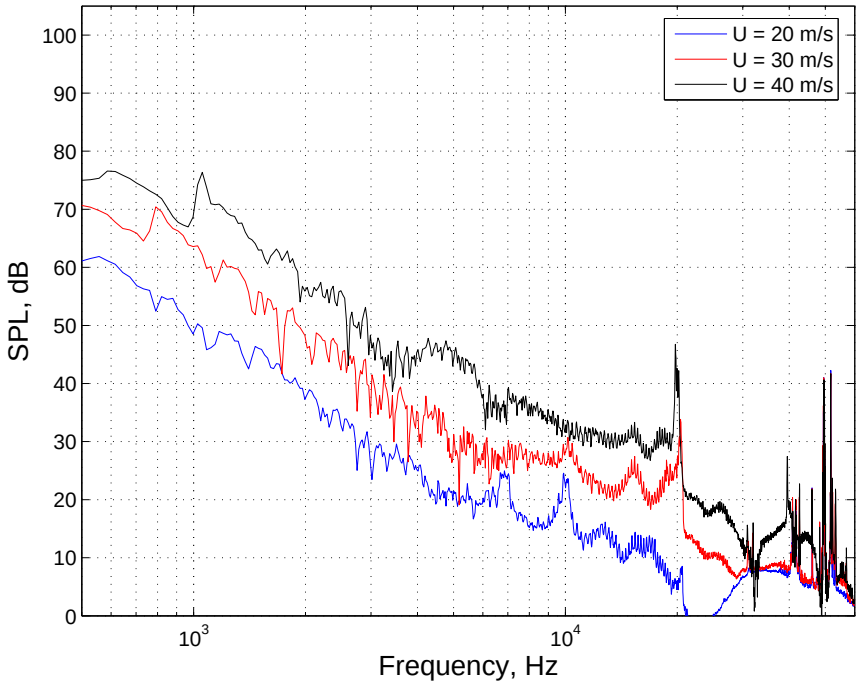

Figure B-42: Perforated plate 5 with $L = 0.1$ m in drag rudder configuration 1.

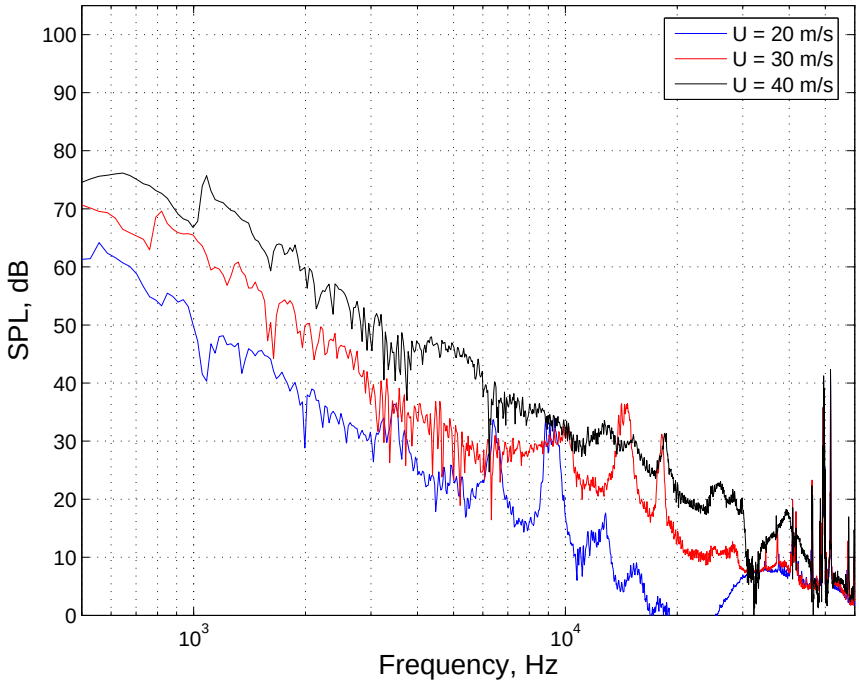

Figure B-43: Perforated plate 5 with $L = 0.2$ m in drag rudder configuration 1.

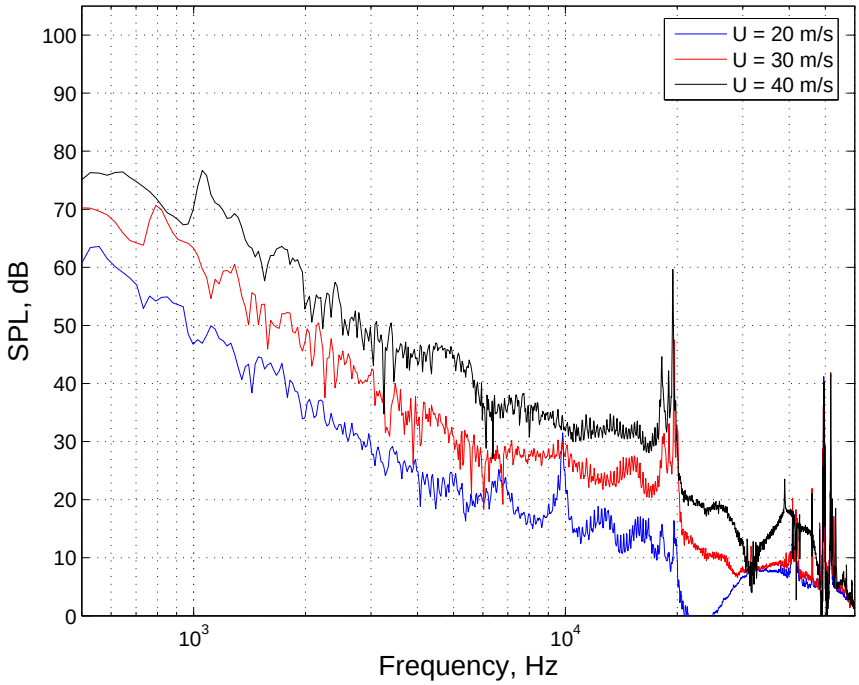

Figure B-44: Perforated plate 5 with $L = 0.1$ m in drag rudder configuration 2.

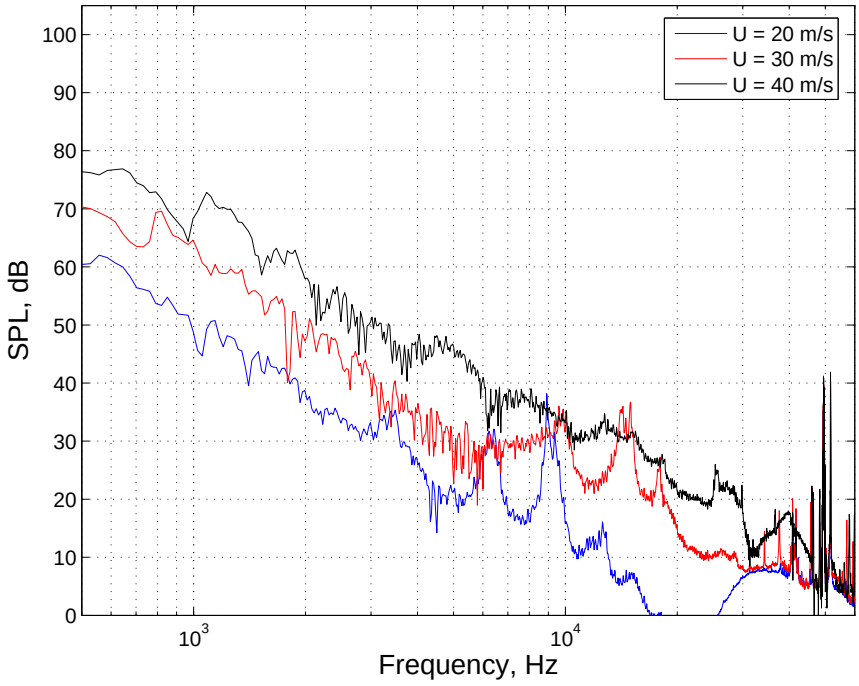

Figure B-45: Perforated plate 5 with $L = 0.2$ m in drag rudder configuration 2.

B.6 Perforated Plate 6

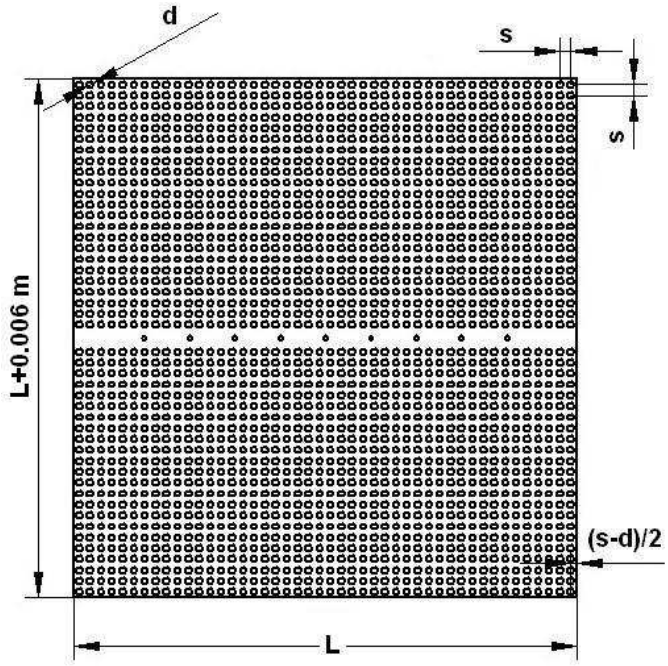

Figure B-46: Perforated plate 6 used in drag rudder configuration 1. $d/L = 0.013$, $s/L = 0.0217$ and $\beta = 0.2819$.

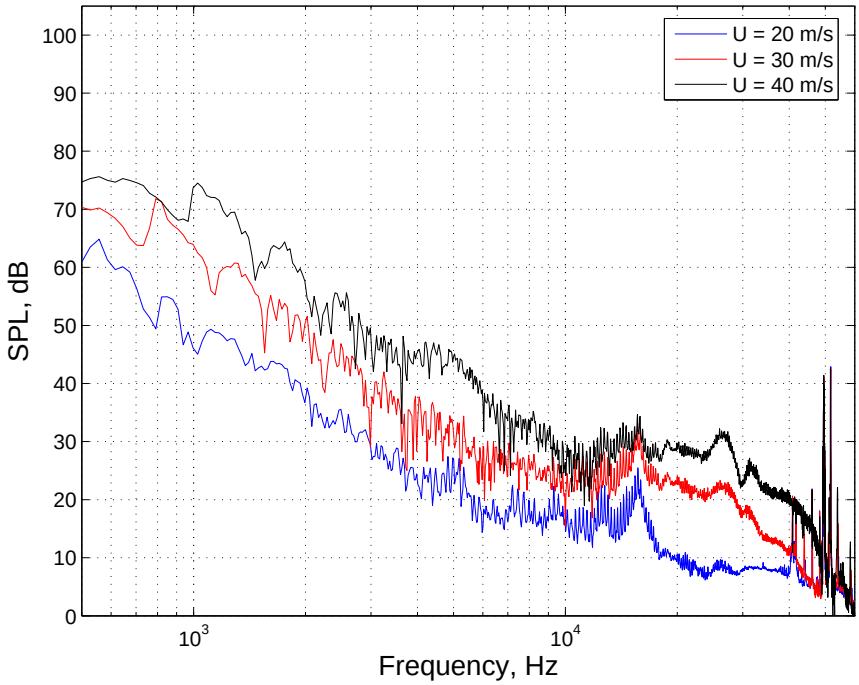

Figure B-47: Perforated plate 6 with $L = 0.1$ m in spoiler configuration 1.

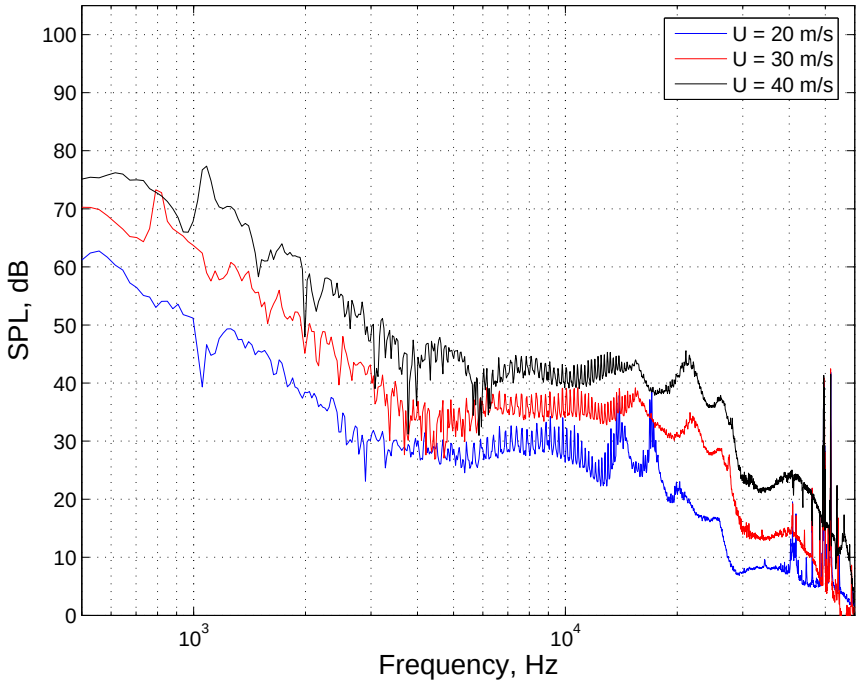

Figure B-48: Perforated plate 6 with $L = 0.2$ m in spoiler configuration 1.

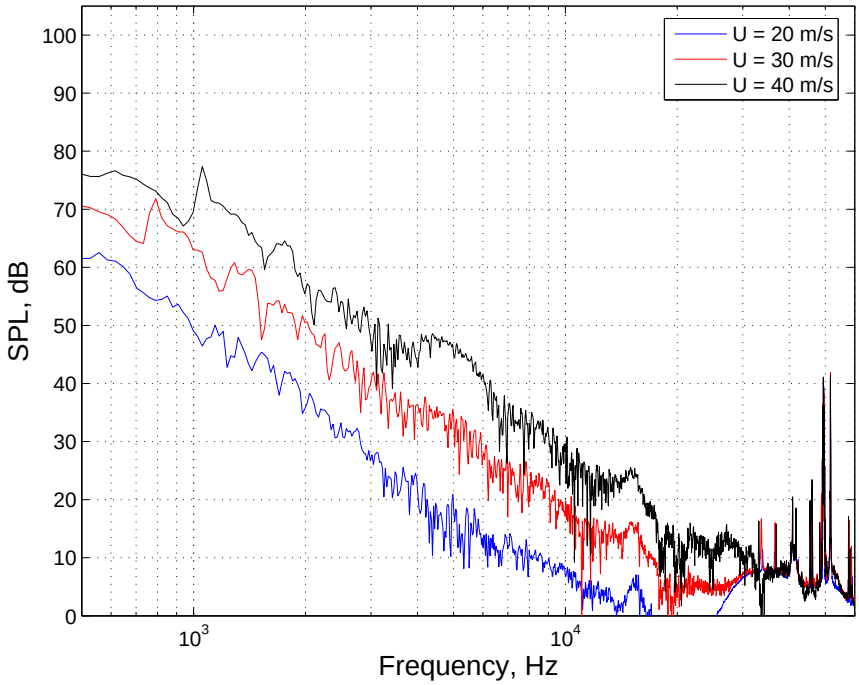

Figure B-49: Perforated plate 6 with $L = 0.1$ m in spoiler configuration 2.

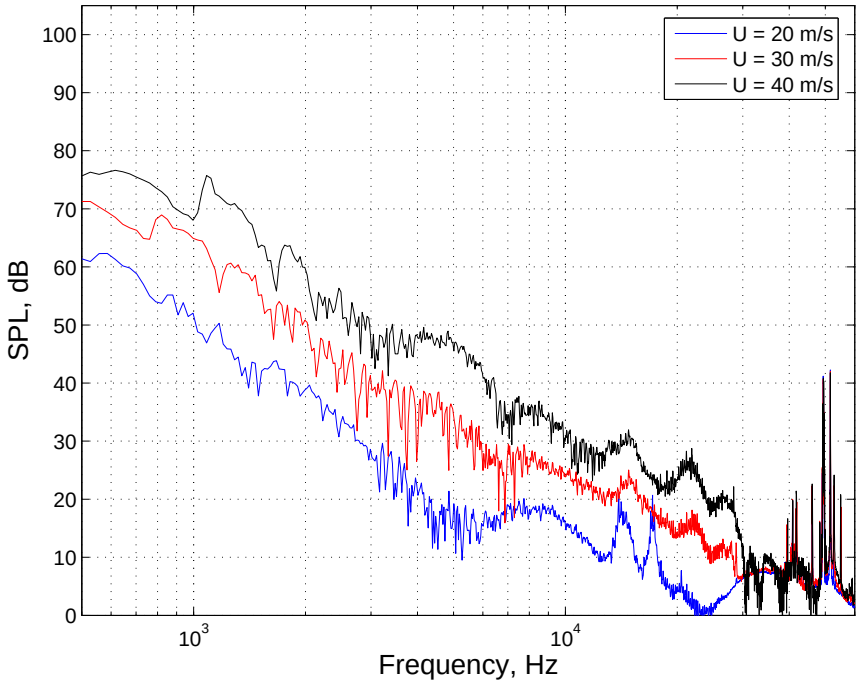

Figure B-50: Perforated plate 6 with $L = 0.2$ m in spoiler configuration 2.

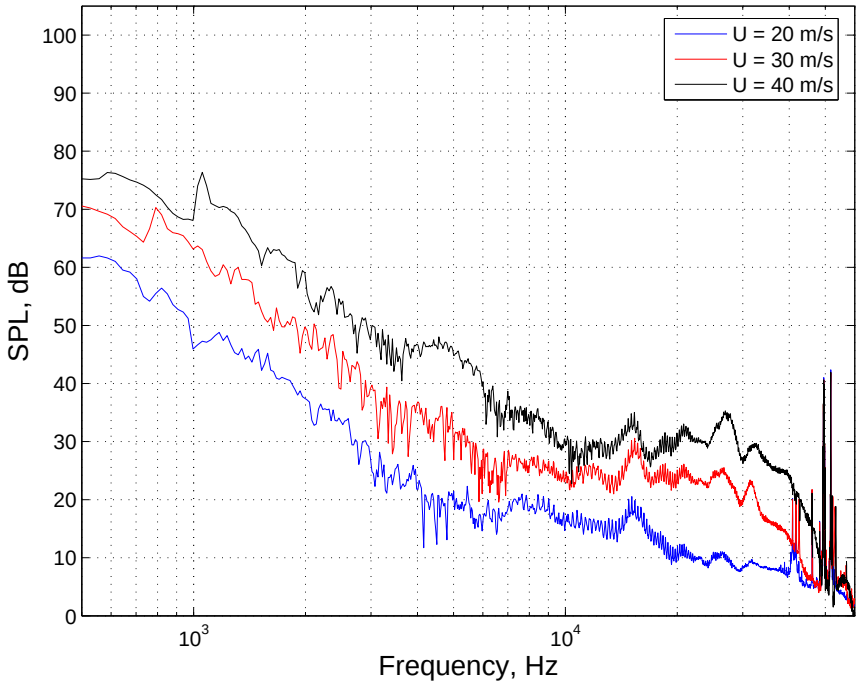

Figure B-51: Perforated plate 6 with $L = 0.1$ m in drag rudder configuration 1.

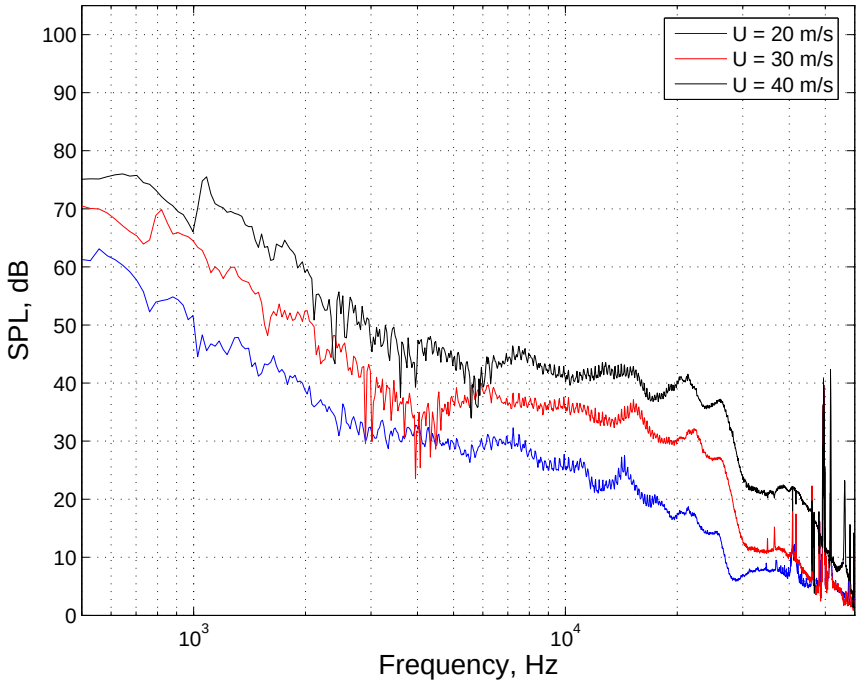

Figure B-52: Perforated plate 6 with $L = 0.2$ m in drag rudder configuration 1.

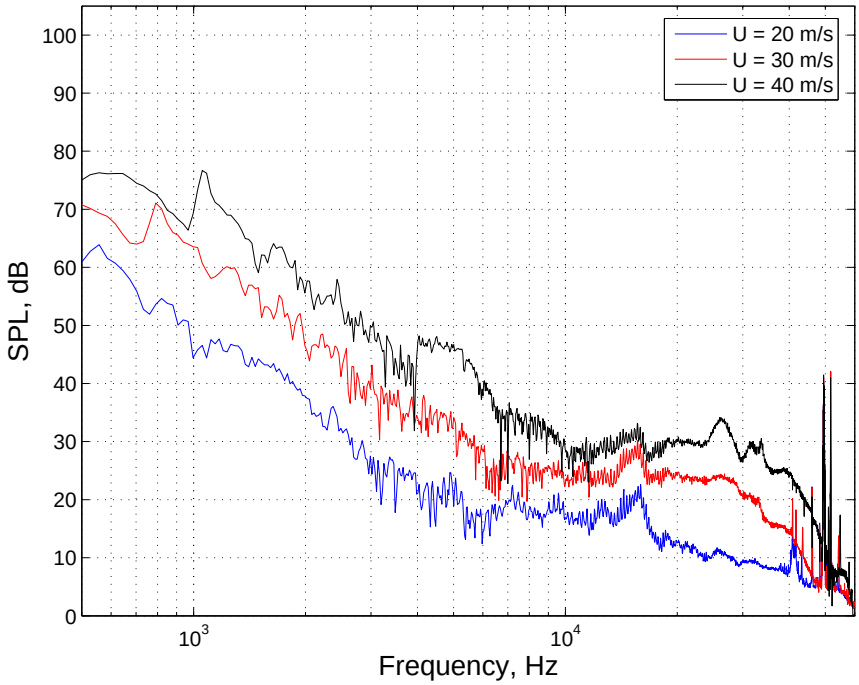

Figure B-53: Perforated plate 6 with $L = 0.1$ m in drag rudder configuration 2.

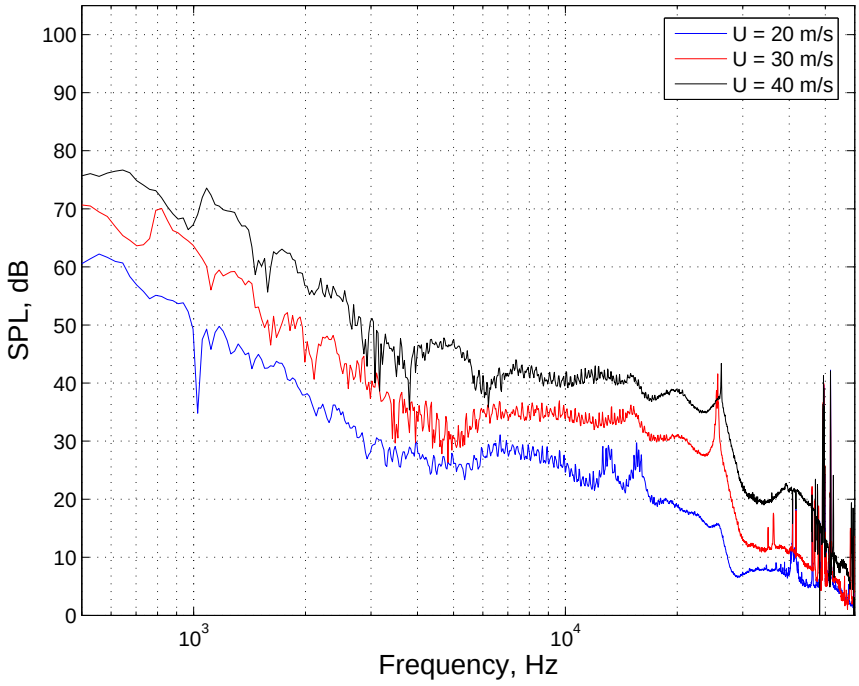

Figure B-54: Perforated plate 6 with $L = 0.2$ m in drag rudder configuration 2.

Appendix C

Figures

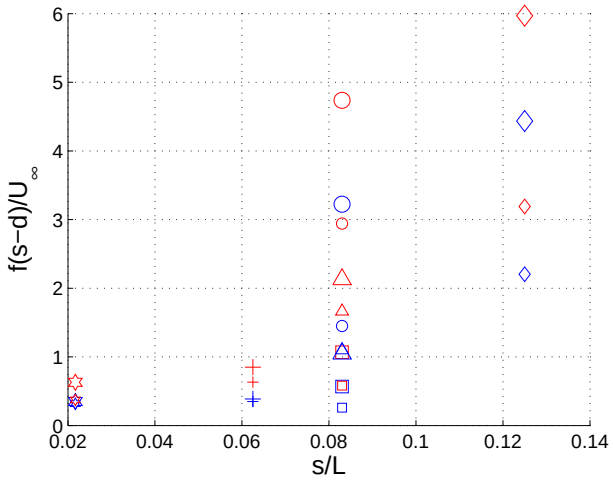

(a) $St_{(s-d)}$ vs s/L

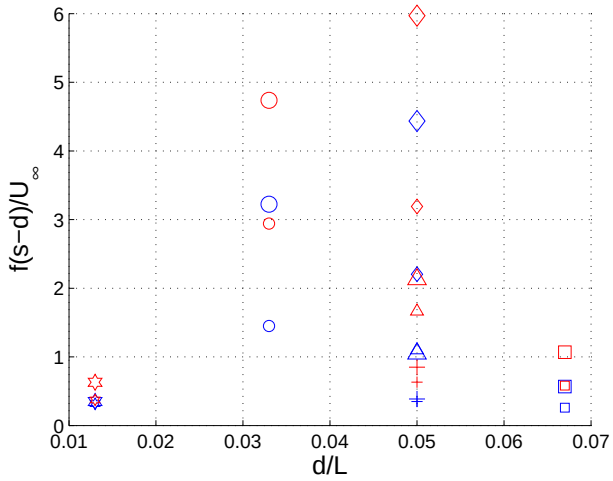

(b) $St_{(s-d)}$ vs d/L

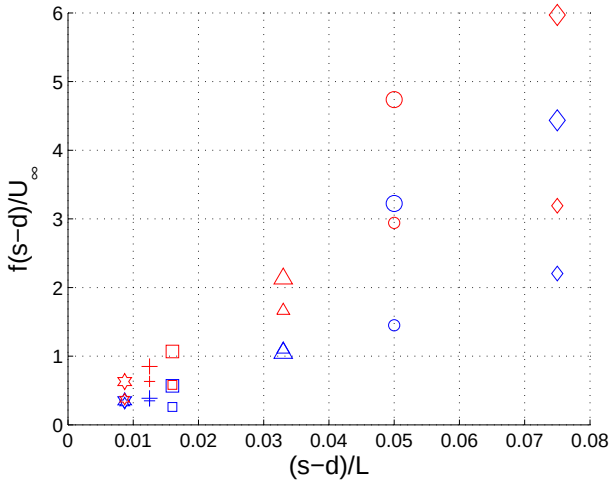

(c) $St_{(s-d)}$ vs $(s-d)/L$

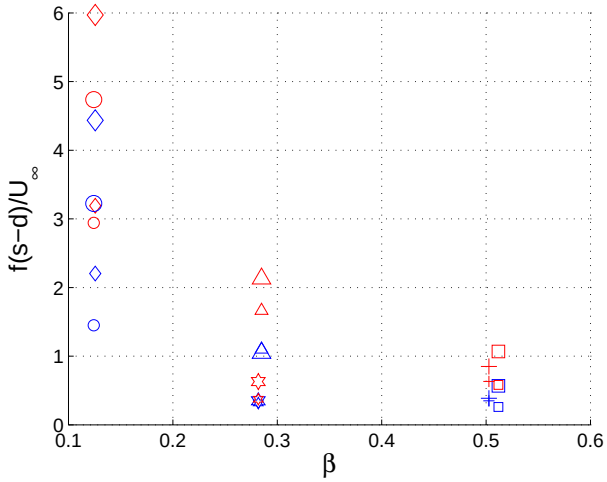

(d) $St_{(s-d)}$ vs β

Figure C-1: $St_{(s-d)}$ variation with plate non-dimensional parameters. Peak **A** data is in blue, while peak **B** data is in red. Small and large markers correspond to the small and large plates, respectively.
'◇' PP1; '□' PP2; '+' PP3; '○' PP4; '△' PP5; '⊛' PP6.

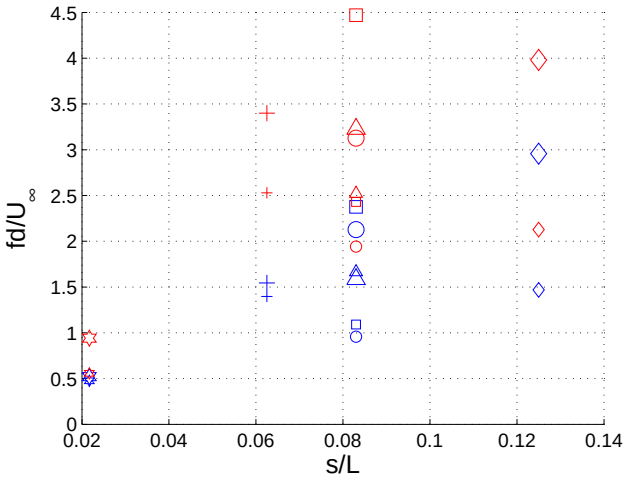

(a) St_d vs s/L

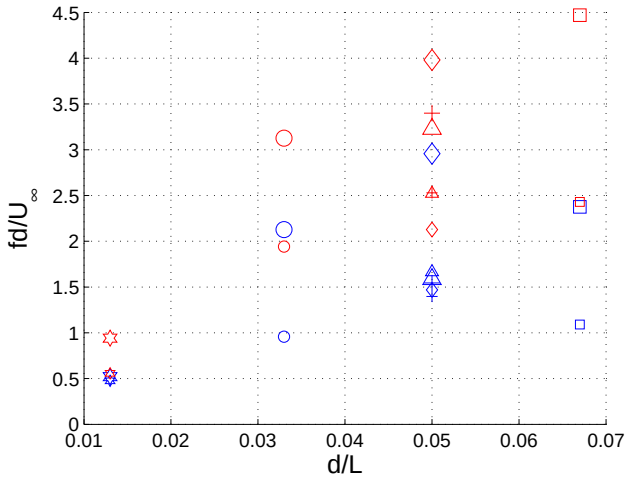

(b) St_d vs d/L

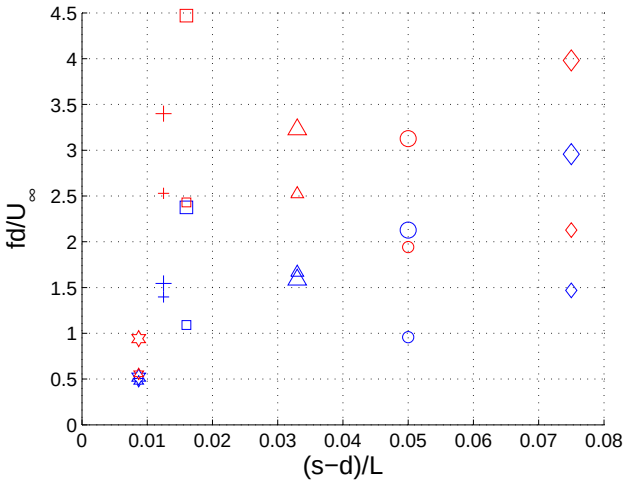

(c) St_d vs $(s-d)/L$

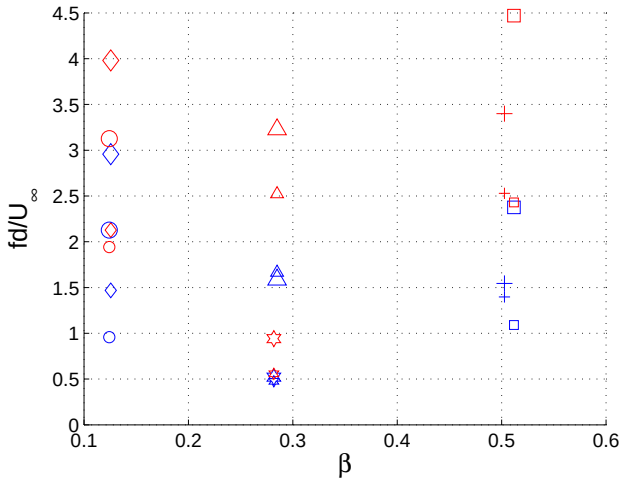

(d) St_d vs β

Figure C-2: St_d variation with plate non-dimensional parameters. Peak **A** data is in blue, while peak **B** data is in red. Small and large markers correspond to the small and large plates, respectively.
'◇' PP1; '□' PP2; '+' PP3; '○' PP4; '△' PP5; '⊛' PP6.

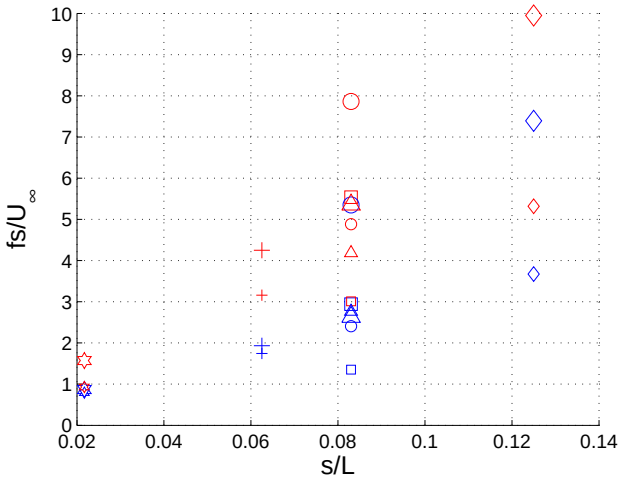

(a) St_s vs s/L

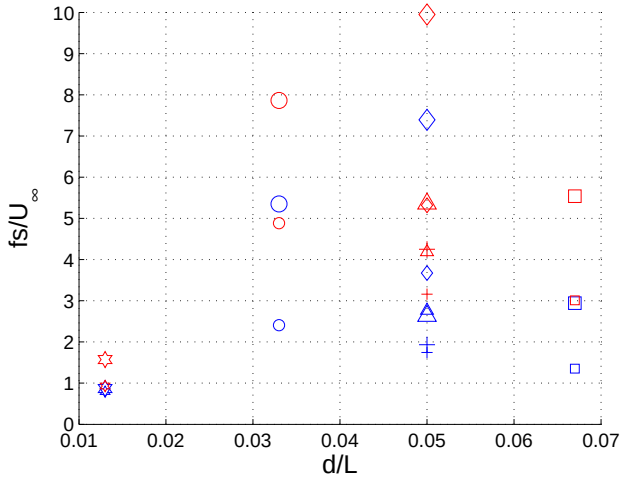

(b) St_s vs d/L

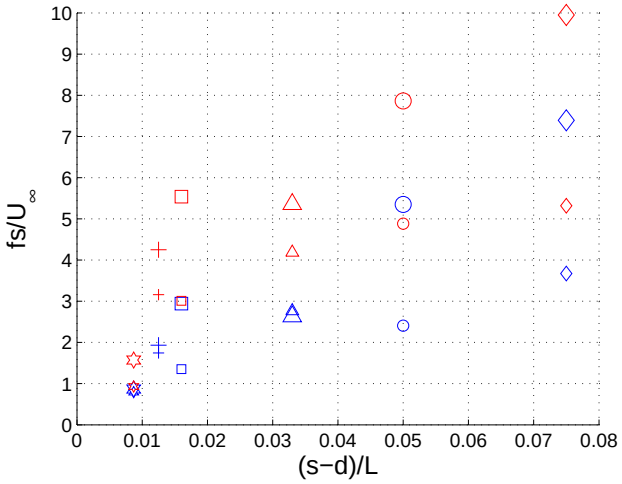

(c) St_s vs $(s-d)/L$

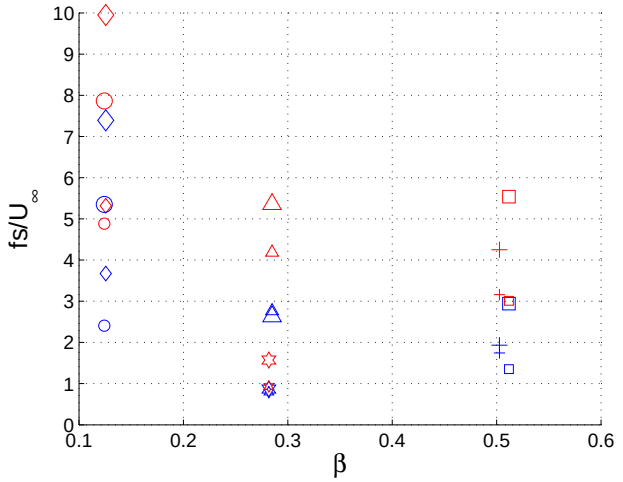

(d) St_s vs β

Figure C-3: St_s variation with plate non-dimensional parameters. Peak **A** data is in blue, while peak **B** data is in red. Small and large markers correspond to the small and large plates, respectively.
'◇' PP1; '□' PP2; '+' PP3; '○' PP4; '△' PP5; '⊛' PP6.

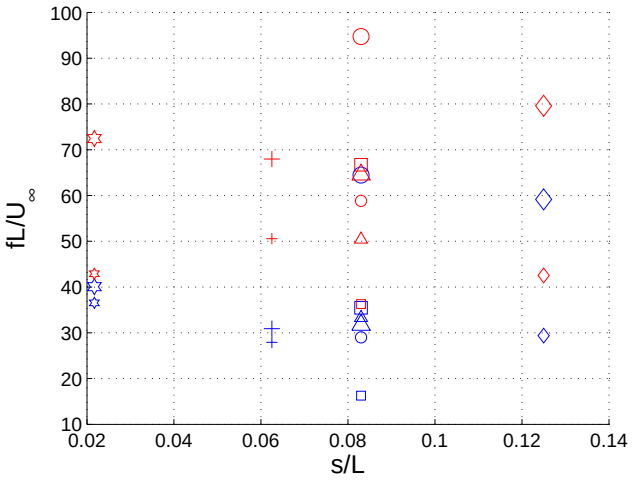

(a) St_L vs s/L

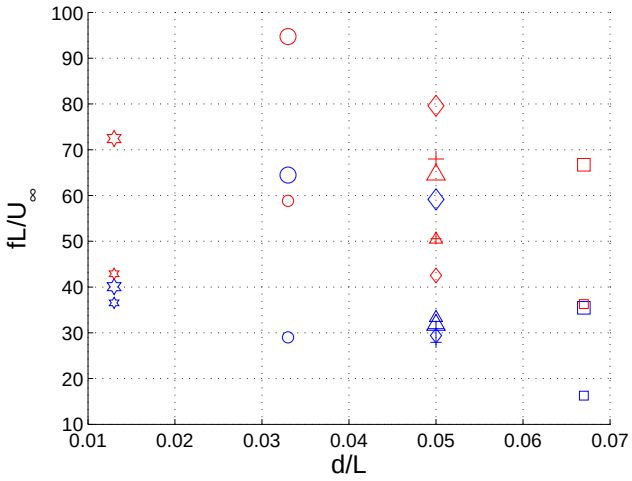

(b) St_L vs d/L

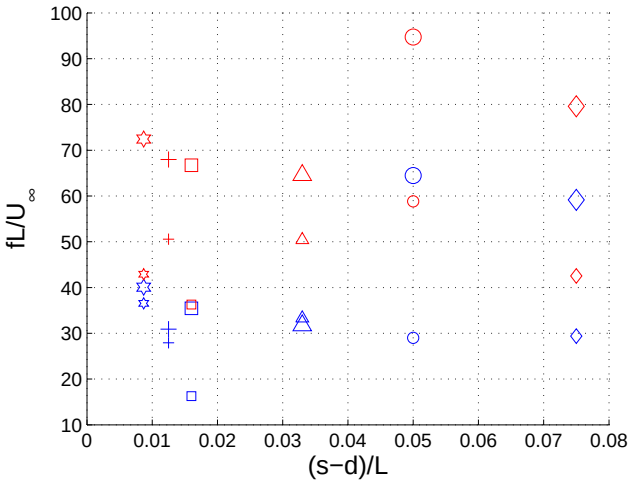

(c) St_L vs $(s-d)/L$

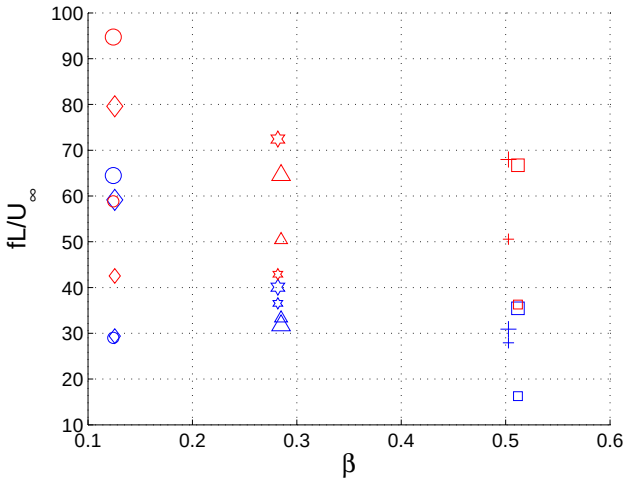

(d) St_L vs β

Figure C-4: St_L variation with plate non-dimensional parameters. Peak **A** data is in blue, while peak **B** data is in red. Small and large markers correspond to the small and large plates, respectively.
'◇' PP1; '□' PP2; '+' PP3; '○' PP4; '△' PP5; '⊛' PP6.

Bibliography

[1] "Noise Impacts of Airport Developments Considered in the National Consultation Documents," Tech. rep., United Kingdom Department for Transportation, 2003.

[2] Tam, R., *Personal Communication*, July 2005.

[3] Owens, R. E., "Energy Efficient Engine Performance System - Aircraft Integration Evaluation," *NASA CR-159488*, 1979.

[4] Huff, D. L., "Technology Development for Aircraft Noise Alleviation: Engine Noise Reduction Research," .

[5] Hileman, J., Hall, C., Agarwal, A., Crichton, D., Diedrich, A., Drela, M., Greitzer, E., Law, T., Madani, V., Quayle, A., Sakaliyski, K., Spakovszky, Z., Tan, D., and Willcox, K., "Integration Taskforce Report - 18 Month Noise and Performance Audit for Silent Aircraft Experimental (SAX) Conceptual Design," .

[6] Tam, C., Golebiowski, M., and Seiner, J. M., "On the Two Components of Turbulent Mixing Noise from Supersonic Jets," AIAA Paper 96-1716, 1996.

[7] Tam, C. and Zaman, K., "Subsonic Jet Noise from Nonaxisymmetric and Tabbed Nozzles," *ASIA Journal*, Vol. 38, No. 4, 2000, pp. 592–599.

[8] Smith, M. J. T., *Aircraft Noise*, Cambridge University Press, 1989.

[9] Mueller, T. J., *Aeroacoustic Measurements*, Springer, New York, 1st ed., 1991.

[10] Dowell, E. H., "Radiation From Panels as a Source of Airframe Noise," *ASIA Journal*, Vol. 13, No. 11, 1975, pp. 1529–1530.

[11] Crighton, D. G., *Aircraft Noise*, chap. Airframe Noise, Addison-Wesley, 1979.

[12] Sonin, A. A., The Physical Basis of Dimensional analysis.

[13] Taylor, G. I., "Air Resistance of a Flat Plate of Very Porous Material," *Reports and Memoranda of the Aeronautical Research Council*.

[14] Castro, I. P., "Wake Characteristics of Two-dimensional Perforated Plates Normal to an Air-stream," *J. Fluid Mech.*, Vol. 46, Part 3, 1971, pp. 599–609.

[15] Eckert, B. and Pfluger, F., "The Resistance Coefficient of Commercial Round Wire Grids," *Reports and Memoranda of the Aeronautical Research Council*.

[16] Davies, R. M., "The Aerodynamics of Porous Sheets," *Reports and Memoranda of the Aeronautical Research Council*.

[17] Blockley, R. H., Master's thesis, University of London, 1968.

[18] Nolan, S. P. R. and Mottley, R., Aircraft Wing Noise Reduction.

[19] "Product Data: Condenser Microphone Cartridges – Types 4133 to 4181," Brüel & Kjær, Nærum, Denmark.

[20] "Product Data: Falcon Range 1/2" Microphone Preamplifier – Types 2669," Brüel & Kjær, Nærum, Denmark.

[21] "S Series Multifunction DAQ," National Instruments, U.S.A.

[22] "Technical Review: Windows to FFT Analysis (Part I)," Brüel & Kjær, Nærum, Denmark, 1987.

[23] "Technical Documentation: Pistonphone Type 4228," Brüel & Kjær, Nærum, Denmark.

[24] Kirk, D. R., *Aeroacoustic Measurement and Analysis of Transient Supersonic Hot Nozzle Flows*, Master's thesis, Massachusetts Institute of Technology, Department of Aeronautics and Astronautics, 1999.

[25] Pierce, A. D., *Acoustics: An Introduction to Its Physical Principles and Applications*, Acoustical Society of America, New York, 2nd ed., 1991.

[26] Allen, C. S., Vandra, K., and Soderman, P. T., "Microphone Corrections for Accurate In-Flow Acoustic Measurements at High Frequency," .

[27] Gutmark, E. and Ho, C.-M., "Preferred Modes and Spreading Rates of Jets," *Phys. Fluids*, Vol. 26, No. 10, 1983, pp. 2932–2938.

[28] Shin, H.-C., *Personal Communication*, August 2005.

[29] Schewe, G., "On the Force Fluctuations Acting on a Circular Cylinder in Crossflow from Subcritical up to Transcritical Reynolds Numbers," *J. Fluid Mech.*, Vol. 133, 1983, pp. 265–285.

[30] Lilley, G., *Personal Communication*, December 2004.

[31] Hileman, J., Faszer, A., Andreou, C., Diedrich, A., Reynolds, T., and Agarwal, A., "Airframe Task Force Report-Trailing Edge Noise Assessment from a Clean Aircraft Configuration," .

[32] ESDU, "ESDU 90023 - Airframe Noise Prediction," .

[33] Tan, D., *Design Trade Studies and Assessment for Advanced Quiet Aircraft Concepts*, Master's thesis, Massachusetts Institute of Technology, Department of Aeronautics and Astronautics, 2005.